

DEVELOPMENT AND CHARACTERIZATION OF SULFIDE BASED ACTIVE  
MATERIALS FOR ELECTROCHEMICAL APPLICATIONS

A THESIS SUBMITTED TO  
THE GRADUATE SCHOOL OF NATURAL AND APPLIED SCIENCES  
OF  
MIDDLE EAST TECHNICAL UNIVERSITY

BY

CANSU SAVAŞ UYGUR

IN PARTIAL FULFILLMENT OF THE REQUIREMENTS  
FOR  
THE DEGREE OF DOCTOR OF PHILOSOPHY  
IN  
METALLURGICAL AND MATERIALS ENGINEERING

JUNE 2022



Approval of the thesis:

**DEVELOPMENT AND CHARACTERIZATION OF SULFIDE BASED  
ACTIVE MATERIALS FOR ELECTROCHEMICAL APPLICATIONS**

submitted by **CANSU SAVAŞ UYGUR** in partial fulfillment of the requirements  
for the degree of **Doctor of Philosophy in Metallurgical and Materials  
Engineering, Middle East Technical University** by,

Prof. Dr. Halil Kalıpçılar  
Dean, Graduate School of **Natural and Applied Sciences**

Prof. Dr. Cemil Hakan Gür  
Head of the Department, **Metallurgical and Materials Eng**

Prof. Dr. Mehmet Kadri Aydınol  
Supervisor, **Metallurgical and Materials Eng**

**Examining Committee Members:**

Prof. Dr. H. Emrah Ünalın  
Metallurgical and Materials Eng, METU

Prof. Dr. M. Kadri Aydınol  
Metallurgical and Materials Eng, METU

Prof. Dr. Ziya Esen  
Inter-Curricular Courses, Çankaya Uni.

Assoc. Prof. Dr. Burak Ülgüt  
Chemistry, Bilkent Uni.

Assist. Prof. Dr. Çiğdem Toparlı  
Metallurgical and Materials Eng, METU

Date: 20.06.2022

**I hereby declare that all information in this document has been obtained and presented in accordance with academic rules and ethical conduct. I also declare that, as required by these rules and conduct, I have fully cited and referenced all material and results that are not original to this work.**

Name Last name : Cansu Savař Uygur

Signature :

## **ABSTRACT**

### **DEVELOPMENT AND CHARACTERIZATION OF SULFIDE BASED ACTIVE MATERIALS FOR ELECTROCHEMICAL APPLICATIONS**

Savaş Uygur, Cansu  
Doctor of Philosophy, Metallurgical and Materials Engineering  
Supervisor: Prof. Dr. Mehmet Kadri Aydınol

June 2022, 135 pages

Next-generation electrochemical applications have faced a challenge to be improved in terms of performance with the increasing demand for new technologies. Although oxide-based active materials are widely used material groups in the electrochemical applications, including batteries, electrolyzers, capacitors and electrochemical catalysis, research in nitride/ phosphide/ boride/ sulfide-based active materials are increasing trend topic to overcome the shortcomings of the metal oxide groups. Sulfide-based active materials show remarkable capacitive and electrocatalytic behavior, which has the potential to be replaced with their commercial counterparts. However, the reaction mechanism behind the capacitive and electrocatalytic performance of certain parts of this group either has not been understood completely or even studied/published. In this study, sulfide-based active materials and/or their composites were synthesized and compounds that were not reported in the literature before were used to improve the electrochemical behavior, including reaction mechanisms and performance. Structural and morphological characterization of synthesized active materials was carried out by using X-ray diffraction (XRD), scanning electron microscopy (SEM), transmission electron microscopy (TEM) and

particle size analysis (PSA). Energy dispersive spectroscopy (EDS) and Rietveld analysis were used for the chemical analysis. Electrochemical characterization was performed by cyclic voltammetry (CV), electrochemical impedance spectroscopy (EIS) and constant current/voltage tests focusing on the capacitive and electrocatalytic performance of the active materials.

Keywords: Microwave-Assisted Synthesis; Metal Sulfides; Oxygen Evolution Reaction; Electrocatalysts

## ÖZ

### **ELEKTROKİMYASAL UYGULAMALAR İÇİN SÜLFİT ESASLI AKTİF MALZEMELERİN GELİŞTİRİLMESİ VE KARAKTERİZASYONU**

Savaş Uygur, Cansu  
Doktora, Metalurji ve Malzeme Mühendisliği  
Tez Yöneticisi: Prof. Dr. Mehmet Kadri Aydınol

Haziran 2022, 135 sayfa

Yeni nesil elektrokimyasal uygulamalar, yeni teknolojilere artan taleple birlikte performans açısından iyileştirilmesi gereken bir durumla karşı karşıya kaldı. Oksit bazlı aktif maddeler, piller, elektrolizörler, kapasitörler ve elektrokimyasal kataliz gibi elektrokimyasal uygulamalarda yaygın olarak kullanılan malzeme grupları olmasına rağmen, metal oksit gruplarının eksikliklerinin üstesinden gelmek için nitrür/fosfit/borid/sülfür bazlı aktif malzemeler üzerine araştırmalar giderek artan trend konular arasında yer almaktadır. Sülfür bazlı aktif malzemeler, ticari muadilleriyle değiştirilme potansiyeline sahip, dikkate değer bir kapasitif ve elektrokatalitik davranış göstermektedir. Bununla birlikte, bu grubun belirli bölümlerinin kapasitif ve elektrokatalitik performansının arkasındaki reaksiyon mekanizması ya tam olarak anlaşılmamıştır ya da çalışılmamıştır/yayınlanmamıştır. Bu çalışmada, sülfür esaslı aktif maddeler ve/veya bunların kompozitleri sentezlenerek daha önce literatürde yayınlanmamış bileşikler kullanılarak reaksiyon mekanizmaları ve performansları dahil elektrokimyasal davranışın iyileştirilmesi amaçlandı. Sentezlenen aktif malzemelerin yapısal ve morfolojik karakterizasyonu, X-ışını kırınımı (XRD), taramalı elektron mikroskobu (SEM), transmisyon elektron

mikroskobu (TEM) ve parçacık boyutu analizi (PSA) kullanılarak gerçekleştirildi. Kimyasal analiz için enerji dağılımlı spektroskopi (EDS) kullanıldı. Elektrokimyasal karakterizasyon ayrıca aktif malzemelerin kapasitif ve elektrokatalitik performansına odaklanan döngüsel voltametri (CV), elektrokimyasal empedans spektroskopisi (EIS) ve sabit akım/gerilim testleri ile gerçekleştirildi.

Anahtar Kelimeler: Mikrodalga-Destekli Sentez, Metal Sülfürler, Oksijen Açığa Çıkarma Reaksiyonu, Elektrokatalizörler

To My Family

## ACKNOWLEDGMENTS

I wish to express my deepest gratitude to my supervisor Prof. Dr. Mehmet Kadri Aydınol, for his guidance, advice, criticism, encouragement and insight throughout the research.

I would also like to thank Prof. Dr. H. Emrah ÜNALAN and Asst. Prof. Dr. Burak Ülğüt for their suggestions and comments during the whole research. I also thank examining committee members Ziya Esen and Çiğdem Toparlı for their criticism and comments.

I want to thank Kadir Özgün KÖSE, Bersu BAŞTUĞ AZER, Erdem Erkin ERDOĞAN, Fundagül ÇUVALOĞLU, Sibel TOPALOĞLU, Arzu Gizem ŞENTÜRK and Deniz VARSAVAŞ for their cordial friendship, guidance and support. I feel so lucky to have such friends. Thanks to also lab-mates Doruk BAHTİYAR and Mustafa Alp YILDIRIM for their friendship and help.

I want to thank my parents and my sister Tuğçe SAVAŞ ÖZTÜRK for their support, encouragement and patience. I also thank my little niece Defne ÖZTÜRK for her existence and for making my life more colorful. I want to express my sincere thanks to my sister Nilay TAM for her endless love, support, encouragement and patience from birth. Her existence in my life is irreplaceable.

My special thanks go to my family Özcan UYGUR and my baby girl growing inside me. Özcan was always by my side at each step of my research. His patience, support, cheerful attitude and never-ending love always motivated me and made me feel happy. I am so lucky to have his love and a growing family with him.

## TABLE OF CONTENTS

ABSTRACT.....	v
ÖZ .....	vii
ACKNOWLEDGMENTS .....	x
TABLE OF CONTENTS.....	xi
LIST OF TABLES .....	xiv
LIST OF FIGURES .....	xvi
LIST OF ABBREVIATIONS .....	xix
CHAPTERS	
1 INTRODUCTION .....	1
1.1 Metal Sulfides in Electrochemical Systems .....	1
1.2 Aim of This Work .....	6
2 LITERATURE REVIEW .....	11
2.1 Structure of Metal Sulfides .....	11
2.2 Microwave-Assisted Synthesis .....	13
2.3 Other Synthesis Methods and Performance of Metal Sulfides as Electrocatalysts .....	17
2.4 Other Synthesis Methods and Performance of Metal Sulfides in Li-ion Battery and Li-S Battery Systems .....	21
2.5 Theory of Electrocatalysis.....	22
2.5.1 OER Mechanisms .....	22
2.5.2 Single or Multi-Electron Transfer.....	23
2.5.3 Calculations.....	24
3 EXPERIMENTAL PROCEDURE .....	29

3.1	Powder Synthesis Procedure.....	29
3.1.1	Materials.....	29
3.1.2	Microwave-Assisted Solvothermal Synthesis Route.....	30
3.1.3	Chemical Precipitation Route.....	31
3.2	Characterization Methods.....	32
3.2.1	Structural Characterization.....	32
3.2.2	Electrode (Electrocatalyst) Preparation and Cell Configuration.....	33
3.2.3	Electrode (Li-Battery) Preparation, Cell Configuration and Testing Procedure.....	34
4	RESULTS AND DISCUSSION.....	35
4.1	Reaction Mechanism of Microwave-Assisted Synthesis of Metal Sulfides	35
4.2	Structural, Morphological and Chemical Characterization of the Transition Metal Sulfides.....	36
4.3	Electrochemical Characterization of Transition Metal Sulfides as OER Electrocatalysts.....	45
4.3.1	Effect of Chromium in Nickel Sulfide.....	45
4.3.2	Effect of A-site Element in $ACr_2S_4$ (A = Ni, Co, Ti) Structure.....	61
4.3.3	Effect of Crystal Structure on the OER Activity.....	72
4.3.4	Effect of Crystallinity.....	83
4.4	Electrochemical Characterization of Transition Metal Sulfides in Li-Battery Systems.....	89
4.5	Summary.....	97
4.6	Future Recommendations.....	101
5	CONCLUSIONS.....	103

REFERENCES .....	105
CURRICULUM VITAE .....	135

## LIST OF TABLES

### TABLES

Table 1.1 Transition metal sulfide studies in electrochemistry .....	5
Table 1.2 Metal-sulfide studies in literature related to electrochemical applications. .....	9
Table 2.1 Calculated Tafel slopes for different rate-determining steps. ....	24
Table 3.1 Experimental details and sample labeling. ....	31
Table 4.1 Phase analysis and crystal structure information. ....	37
Table 4.2 EDS results of the samples in terms of at. %. ....	41
Table 4.3 Rietveld analysis of NiS-mw, Cr/NiS and NiCr <sub>2</sub> S <sub>4</sub> -194 samples. ....	47
Table 4.4 Surface properties of the electrocatalysts. ....	49
Table 4.5 Intrinsic OER activities and Tafel slopes of the NiS-mw, Cr/NiS and NiCr <sub>2</sub> S <sub>4</sub> -194 samples. ....	60
Table 4.6 Resistance values of the NiS-mw, Cr/NiS and NiCr <sub>2</sub> S <sub>4</sub> -194 samples. ..	61
Table 4.7 Rietveld analysis of NiCr <sub>2</sub> S <sub>4</sub> -12, CoCr <sub>2</sub> S <sub>4</sub> and TiCr <sub>2</sub> S <sub>4</sub> samples and ionic radius with six-fold octahedral coordination of Ti, Cr, Co and Ni atoms [106], respectively. ....	63
Table 4.8 Electrochemical surface area (ECSA) and roughness factor (RF) values of the NiCr <sub>2</sub> S <sub>4</sub> -12, CoCr <sub>2</sub> S <sub>4</sub> and TiCr <sub>2</sub> S <sub>4</sub> samples. ....	69
Table 4.9 Intrinsic OER activities and Tafel slopes of the NiCr <sub>2</sub> S <sub>4</sub> -12, CoCr <sub>2</sub> S <sub>4</sub> and TiCr <sub>2</sub> S <sub>4</sub> samples. ....	71
Table 4.10 Resistance values of the NiCr <sub>2</sub> S <sub>4</sub> -12, CoCr <sub>2</sub> S <sub>4</sub> and TiCr <sub>2</sub> S <sub>4</sub> samples. .....	72
Table 4.11 Crystal structure information of the NiCr <sub>2</sub> S <sub>4</sub> -194 sample. ....	74
Table 4.12 Crystal structure information of the NiCr <sub>2</sub> S <sub>4</sub> -12 sample. ....	74
Table 4.13 EDS analysis results of the NiCr <sub>2</sub> S <sub>4</sub> -194 and NiCr <sub>2</sub> S <sub>4</sub> -12 samples. ...	75
Table 4.14 Electrochemical surface area (ECSA) and roughness factor (RF) values of the NiCr <sub>2</sub> S <sub>4</sub> -194 and NiCr <sub>2</sub> S <sub>4</sub> -12 samples. ....	75

Table 4.15 Intrinsic OER activities and Tafel slopes of the NiCr <sub>2</sub> S <sub>4</sub> -194 and NiCr <sub>2</sub> S <sub>4</sub> -12 samples. ....	76
Table 4.16 Resistance values of the NiCr <sub>2</sub> S <sub>4</sub> -194 and NiCr <sub>2</sub> S <sub>4</sub> -12 samples. ....	78
Table 4.17 Crystal structure information of the CoS sample.....	79
Table 4.18 Crystal structure information of the Co <sub>9</sub> S <sub>8</sub> sample.....	80
Table 4.19 EDS analysis results of the CoS and Co <sub>9</sub> S <sub>8</sub> samples.....	81
Table 4.20 Electrochemical surface area (ECSA) and roughness factor (RF) values of the CoS and Co <sub>9</sub> S <sub>8</sub> samples.....	81
Table 4.21 Intrinsic OER activities and Tafel slopes of the CoS and Co <sub>9</sub> S <sub>8</sub> samples.....	82
Table 4.22 Resistance values of the CoS and Co <sub>9</sub> S <sub>8</sub> samples. ....	82
Table 4.23 EDS analysis results of the NiCr <sub>2</sub> S <sub>4</sub> -194 and Ni-Cr-S samples. ....	85
Table 4.24 Electrochemical surface area (ECSA) and roughness factor (RF) values of the NiCr <sub>2</sub> S <sub>4</sub> -194 and Ni-Cr-S samples. ....	85
Table 4.25 Intrinsic OER activities and Tafel slopes of the NiCr <sub>2</sub> S <sub>4</sub> -194 and Ni-Cr-S samples. ....	87
Table 4.26 Resistance values of the NiCr <sub>2</sub> S <sub>4</sub> -194 and Ni-Cr-S samples.....	89
Table 4.27 Li-ion battery performances of the NiCr <sub>2</sub> S <sub>4</sub> -12, CoCr <sub>2</sub> S <sub>4</sub> , TiCr <sub>2</sub> S <sub>4</sub> electrodes. ....	95
Table 4.28 Summary of the OER electrocatalyst performances.....	98
Table 4.29 Summary of the Li-battery electrode performances. ....	100

## LIST OF FIGURES

### FIGURES

Figure 1.1. Discharge potential vs. capacity plots of conversion-type Li-ion battery (a) cathodes and (b) all types of electrodes. Reproduced from [2].	3
Figure 1.2. Crystal structures of transition metal sulfides used in this study. Yellow spheres represent the sulfur atom and blue/pink/green spheres represent the transition metal sites [49]. Transition metal atoms occupy the same atomic sites in bimetallic compounds.	8
Figure 2.1. Crystal structure (a), local bonding around B (b), and A atoms (c) of spinel compounds [144].	13
Figure 2.2. (a) A number of publications regarding microwave synthesis categorized according to research fields on the web of science database until 2021, June, (b) Percent distribution of microwave synthesis publications in scientific research.	15
Figure 2.3. Heating-cooling profile of a sample heated to 300 °C for 10 minutes. Regions named as a, b and c represent the heating region, temperature holding region and cooling region, respectively [147].	16
Figure 2.4. Cyclic voltammogram within the non-Faradaic potential region at different scan rates [179].	25
Figure 2.5. (a) Linear sweep voltammogram and (b) Tafel plot [180].	28
Figure 3.1. Experimental setup for microwave-assisted synthesis route.	30
Figure 4.1. XRD pattern of single-phase metal sulfides with space group no (a) 194, (b) 12 and (c-h) phase mixtures.	38
Figure 4.2. Binary phase diagram of cobalt and sulfur [182].	39
Figure 4.3. SEM micrographs of the samples synthesized via precipitation.	43
Figure 4.4. SEM micrographs of the samples synthesized via microwave.	44
Figure 4.5. (a) XRD spectrum and phase analysis of NiS-mw sample and (b) XRD pattern of NiS-mw, Cr/NiS and NiCr <sub>2</sub> S <sub>4</sub> -194 samples in comparison.	46

Figure 4.6. EDS-mapping images of (a) NiS-mw, (b) Cr/NiS, (c) NiCr <sub>2</sub> S <sub>4</sub> -194 samples and (d) EDS analysis results. ....	48
Figure 4.7. Crystal structures of (a) NiS (space group P63/mmc, no: 194), (b) CrS (space group P63/mmc, no: 194) and (c) NiCr <sub>2</sub> S <sub>4</sub> (space group P63/mmc, no: 194) compounds. ....	49
Figure 4.8. SEM micrographs of the (a) NiS-mw, (b) Cr/NiS and (c) NiCr <sub>2</sub> S <sub>4</sub> -194 samples. ....	50
Figure 4.9. Cyclic voltammetry curves of (a) NiS-mw, (b) Cr/NiS and (c) NiCr <sub>2</sub> S <sub>4</sub> -194 electrocatalysts in the non-Faradaic region. ....	52
Figure 4.10. (a) Ni-2p, (b) Cr-2p and (c) S-2p XPS spectra of the NiS-mw, Cr/NiS and NiCr <sub>2</sub> S <sub>4</sub> -194 electrocatalysts. ....	54
Figure 4.11. Cyclic voltammograms at the (a) 1 <sup>st</sup> , (b) 2 <sup>nd</sup> , (c) 50 <sup>th</sup> and (d)100 <sup>th</sup> cycles of the NiS-mw, Cr/NiS and NiCr <sub>2</sub> S <sub>4</sub> -194 samples. ....	55
Figure 4.12. Cyclic voltammetry curves of the (a) NiS-mw, (b) Cr/NiS and (c) NiCr <sub>2</sub> S <sub>4</sub> -194 electrocatalysts at 1 <sup>st</sup> , 2 <sup>nd</sup> , 50 <sup>th</sup> and 100 <sup>th</sup> cycles. ....	56
Figure 4.13. Comparison of the uncorrected (solid) and iR-corrected (dashed) LSV curves of NiS-mw, Cr/NiS and NiCr <sub>2</sub> S <sub>4</sub> -194 samples and bare glassy carbon electrode (GC). ....	57
Figure 4.14. (a) LSV curves, (b) CP curves, (c) Tafel slopes and EIS plots at (d) 1.52 V and (e) 1.62 V of the electrocatalysts. ....	58
Figure 4.15. XRD pattern of NiCr <sub>2</sub> S <sub>4</sub> -12, CoCr <sub>2</sub> S <sub>4</sub> and TiCr <sub>2</sub> S <sub>4</sub> samples. ....	62
Figure 4.16. Crystal structures of (a) NiCr <sub>2</sub> S <sub>4</sub> (space group C12/m1, no: 12), (b) CoCr <sub>2</sub> S <sub>4</sub> (space group C12/m1, no: 12) and (c) TiCr <sub>2</sub> S <sub>4</sub> (space group C12/m1, no: 12) compounds. ....	64
Figure 4.17. EDS-mapping images of (a) NiCr <sub>2</sub> S <sub>4</sub> -12, (b) CoCr <sub>2</sub> S <sub>4</sub> , (c) TiCr <sub>2</sub> S <sub>4</sub> samples and (d) EDS analysis results. ....	65
Figure 4.18. Cyclic voltammograms at the (a) 1 <sup>st</sup> , (b) 2 <sup>nd</sup> , (c) 50 <sup>th</sup> and (d)100 <sup>th</sup> cycles of the NiCr <sub>2</sub> S <sub>4</sub> -12, CoCr <sub>2</sub> S <sub>4</sub> and TiCr <sub>2</sub> S <sub>4</sub> samples. ....	66
Figure 4.19. Cyclic voltammetry curves of the (a) NiCr <sub>2</sub> S <sub>4</sub> -12, (b) CoCr <sub>2</sub> S <sub>4</sub> and (c) TiCr <sub>2</sub> S <sub>4</sub> electrocatalysts at 1 <sup>st</sup> , 2 <sup>nd</sup> , 50 <sup>th</sup> and 100 <sup>th</sup> cycles. ....	67

Figure 4.20. Cyclic voltammetry curves of (a) NiCr2S4-12, (b) CoCr2S4 and (c) TiCr2S4 electrocatalysts in the non-Faradaic region. ....	68
Figure 4.21. (a) LSV curves, (b) CP curves, (c) Tafel slopes and EIS plots at (d) 1.55 V and (e) 1.60 V of the NiCr2S4-12, CoCr2S4 and TiCr2S4 samples. ....	70
Figure 4.22. Crystal structure images of (a) NiCr2S4-194 (space group P63/mmc, no: 194) and (b) NiCr2S4-12 (space group C2/m, no: 12) compounds. ....	73
Figure 4.23. (a) LSV curves, (b) Tafel slopes and EIS plots at (c) small and (d) large working potentials of the NiCr2S4-194 and NiCr2S4-12 samples. ....	77
Figure 4.24. Crystal structure images of (a) CoS (space group P63/mmc, no: 194) and (b) Co9S8 (space group Fm-3m, no: 225) compounds. ....	79
Figure 4.25. (a) LSV curves, (b) Tafel slopes and EIS plots at (c) small and (d) large working potentials of the CoS and Co9S8 samples. ....	83
Figure 4.26. XRD pattern of the NiCr2S4-194 and Ni-Cr-S samples. ....	84
Figure 4.27. (a) LSV curves, (b) Tafel slopes and EIS plots at (c) small and (d) large working potentials of the NiCr2S4-194 and Ni-Cr-S samples. ....	86
Figure 4.28. CP curve of the amorphous Ni-Cr-S sample. ....	88
Figure 4.29. Cell potential vs. specific discharge capacity curves of NiCr2S4-194 and Ni-Cr-S samples coated onto Cu-foil in 1.5 M LiPF6 in EC: EMC: DMC electrolyte system. ....	91
Figure 4.30. Cell potential vs. specific discharge capacity curves of NiCr2S4-194 samples with electrode compositions of (active material: carbon: binder) 8:1:1 and 6:2:2. ....	92
Figure 4.31. Cell potential vs. specific discharge capacity curves of NiCr2S4-194 and NiCr2S4-12 samples. ....	93
Figure 4.32. (a) Specific capacity curves at the first cycle at 50 mA g <sup>-1</sup> and (b) Capacity retention cycles of the NiCr2S4-12, CoCr2S4, TiCr2S4 at 100 mA g <sup>-1</sup> . ..	94
Figure 4.33. Nyquist plots of (a) as-assembled and (b) after 50 cycles at 100 mA g <sup>-1</sup> of the NiCr2S4-12, CoCr2S4, TiCr2S4 electrodes. ....	96

## LIST OF ABBREVIATIONS

### ABBREVIATIONS

BET	Brunauer–Emmett–Teller
CP	Chronopotentiometry
CV	Cyclic Voltammetry
ECSA	Electrochemically Active Surface Area
EDS	Energy Dispersive Spectroscopy
EIS	Electrochemical Impedance Spectroscopy
GC	Glassy Carbon
GEO	Geometrical
HER	Hydrogen Evolution Reaction
LSV	Linear Sweep Voltammetry
OCV	Open Circuit Potential
OER	Oxygen Evolution Reaction
ORR	Oxygen Reduction Reaction
RHE	Reversible Hydrogen Electrode
RF	Roughness Factor
SA	Surface Area
SEM	Scanning Electron Microscopy
TOF	Turnover Frequency
XPS	X-ray Photoelectron Spectroscopy
XRD	X-ray Diffraction



# CHAPTER 1

## INTRODUCTION

### 1.1 Metal Sulfides in Electrochemical Systems

In the field of electrochemical research, the popularity of stoichiometric metal oxides has begun to decline. In contrast, studies on non-stoichiometric metal oxides and variants of stoichiometric and non-stoichiometric metal halides, metal phosphides, metal sulfides, metal borides, and metal nitrides have started to accelerate. Among them, sulfide-based materials have been studied and found in various application fields for decades. The electrochemical activity of metal sulfides made it one of the material groups studied in the field of electrochemical energy storage and electrocatalysis. In this regard, metal sulfides were first used as a positive electrode, instead of elemental sulfur, for lithium-sulfur batteries operating at high temperatures [1]. Subsequently, they were used as Li-ion battery anodes and cathodes. The theoretical capacity of chalcogenides (metal sulfides are named as chalcogenides when they are in the form of MS and as dichalcogenides when they are in the form of MS<sub>2</sub> where M and S refer to metal and sulfur, respectively) extends over a wide range as a Li-ion battery cathode shown in Figure 1(a) [2]. The highest theoretical potential can be achieved by metal fluorides; however, the highest capacity (approximately 1700 mAh g<sup>-1</sup>) belongs to chalcogenides as cathodes. The reason is the chemistry of the metal sulfides as well as the Li-storage mechanism. The specific capacities of Li-ion battery electrodes regarding the Li-storage mechanism were compared in Figure 1(b). Conversion electrodes yield a higher specific capacity as compared to intercalation electrodes. The reason is that conversion cathodes can store 2 or 3 Li-ions per chemical formula, while intercalation cathodes store only one Li-ion.

The lithium storage mechanism of metal sulfides mainly consists of two steps: i) (de)intercalation and ii) conversion reaction depending on the potential window [3]. These two distinct storage mechanisms come with their benefits and drawbacks. The intercalation mechanism provides excellent structural stability during cycling, which increases battery life. However, the intercalation mechanism limits the charge storage, which causes a lower specific capacity than that of the conversion mechanism [4]. The conversion mechanism results in higher specific capacity, whereas it confronts structural instability due to volume expansion.

As a conversion electrode, metal sulfides undergo reactions, including breaking chemical bonds and forming new ones. Possible conversion mechanisms during lithium insertion and extraction are *i*) true conversion and *ii*) chemical transformation [2].



True conversion and chemical transformation were given in equations 1.1 and 1.2, respectively, where  $M'$  = cation,  $X'$  = anion, and  $M$  = reduced form of the cation. In the case of metal sulfides, when  $X'$  is  $S^{2-}$  and  $M$  is one of the transition metals, i.e.  $Cu^{2+}$ ,  $Ni^{2+}$ ,  $Co^{2+}$ ,  $Fe^{2+}$ ,  $Fe^{3+}$ ,  $Mn^{3+}$ , etc., true conversion is the reaction mechanism. Chemical transformation simply forms  $Li_2S$  when  $2Li^+$  ions react with  $S^{2-}$  ions.

Challenges for conversion electrodes focus on their typical drawbacks. These drawbacks are: volume change, low conductivity, large voltage hysteresis, and unwanted active material/electrolyte interactions are the main problems of conversion cathodes. Making hybrid nano-composite active material, carbon encapsulation, use of a lithiated form of active materials, conductive additives, electrically conductive intermediate phase formations during conversion reactions,

decreasing particle size of the active material, reducing ionic resistance at the electrode surface, minimizing energy losses due to plastic deformation during phase transformation and preventing active material loss with electrolyte additives by avoiding the side reactions are some of the possible solutions for the shortcomings of the conversion electrodes. In short, the design of active materials (morphology, size, and chemistry), electrolyte additives, and surface protection should be the primary focus to increase the performance [4–7]. Metal sulfides formed as intermediate phases during cycling and their dissolution in the electrolyte, as well as volume change (structural instability), both cause a decrease in the cycle life of Li-based batteries. However, these intermediate phases allow multi-electron redox reactions, which provide a higher capacity for batteries and capacitors.

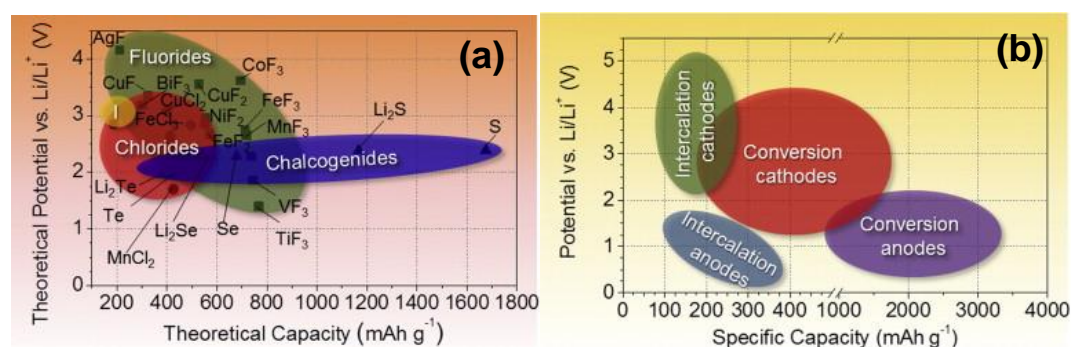


Figure 1.1. Discharge potential vs. capacity plots of conversion-type Li-ion battery (a) cathodes and (b) all types of electrodes. Reproduced from [2].

The efficient use of energy and the protection of the environment are the primary priorities of today's world. The rapid increase in the demands in the field of energy from day to day, and the fact that the needs will double in 15 years, have directed academic and industrial studies around the world to this field. However, today, energy demands are provided by fossil fuels that are not sustainable and have limited reserves. Therefore, the conversion of energy from renewable sources is very critical in order to reduce dependence on fossil fuels. When considering the most practical,

chemically clean and effective energy systems in terms of electrochemical reactions, fuel cells, metal-air batteries and water splitting reactions come first. In this manner, oxygen evolution reaction (OER), oxygen reduction reaction (ORR) and hydrogen evolution reaction (HER) are the fundamental mechanisms for all these systems. Limiting factors of large-scale commercialization of the electrochemical water splitting are; *i*) high cost of the benchmark electrocatalysts, *ii*) poor stability of the electrocatalysts and *iii*) kinetic restrictions (requirement of larger overpotentials than the 1.23 V) to drive the reaction. Pt, Ru and Ir-based noble metals have great popularity as benchmark water splitting electrocatalysts, but their poor stability due to agglomeration and dissolution limits their performance and efficiency [8]. Sulfide-based materials are very promising electrocatalysts that can be the candidates for benchmark Pt, Ru and Ir-based noble metals with their high earth abundance, low cost, good electrical conductivity and good electrocatalytic activity. In this regard, Ni or Co-based sulfides are the most promising ones with their performance, but they suffer from poor stability. Thermodynamic instability may be the main reason resulting in structural deterioration and stripping off the substrate surface.

Increasing the catalyst surface area by reducing the particle size is one factor that enhances the catalytic activity. Another way to improve the intrinsic performance of the catalyst is introducing defects and strains (excess or deficient constituent elements, additives, second phases, etc.), leading to modification of the electronic structure and creating a synergistic effect between the additive and the matrix to enhance OER performance. Iron [9,10], cobalt [11], aluminum [12], zinc [13], nitrogen [14,15], fluorine [16], borate [17], Fe and Mn co-doping [18], Cu and Co co-doping [19] are the ones reported mostly as effective dopants in water splitting.

Today, distinctive features of metal sulfides enable them to be studied in the fields of electrochemical research other than Li-based systems. Some of the transition metal sulfide studies in electrochemistry are listed in Table 1.1.

Table 1.1 Transition metal sulfide studies in electrochemistry.

<b>Material</b>	<b>System</b>	<b>Ref.</b>
<b>(Di)Chalcogenides (MS, MS<sub>2</sub>, MS<sub>3</sub>, etc. compounds)</b>		
SnS <sub>2</sub>	Li-ion anode	[20]
Ni <sub>3</sub> S <sub>2</sub>	Li-ion cathode	[21]
CuS, FeS <sub>2</sub> , Co <sub>9</sub> S <sub>8</sub>	Li-ion cathode	[22]
CoS and CoS <sub>2</sub>	Li-ion cathode	[23]
Ni <sub>3</sub> S <sub>2</sub>	Li-polymer cathode	[24]
MoS <sub>2</sub>	Supercapacitor	[25]
Co <sub>9</sub> S <sub>8</sub>	Electrocatalyst	[26]
Ni <sub>3</sub> S <sub>2</sub>	Electrocatalyst	[27]
MoS <sub>2</sub> and Mo <sub>2</sub> S <sub>3</sub>	Electrocatalyst	[28]
ZnS	Photocatalyst	[29]
<b>Mixed Metal Sulfides (A-B-S mixtures)</b>		
FeCoS	Supercapacitor	[30]
NiCoS	Supercapacitor	[31]
ZnCdS	Photo/electrocatalyst	[32]
NiWS	Catalyst	[33]
<b>Thiospinels (AB<sub>2</sub>S<sub>4</sub> compounds)</b>		
MgCr <sub>2</sub> S <sub>4</sub>	Mg-ion cathode	[34]
Mg <sub>x</sub> Zr <sub>2</sub> S <sub>4</sub>	Mg-ion cathode	[35]
Mo <sub>x</sub> Ti <sub>2</sub> S <sub>4</sub>	Mg-ion cathode	[36]
MgCr <sub>2</sub> S <sub>4</sub>	Li-ion cathode	[37]
Ni <sub>x</sub> Cu <sub>1-x</sub> Co <sub>2</sub> S <sub>4</sub>	Supercapacitor	[38]
Ni <sub>x</sub> Co <sub>1-x</sub> MoS <sub>y</sub>	Supercapacitor	[39]
Ni <sub>x</sub> Co <sub>3-x</sub> S <sub>4</sub>	Supercapacitor and Electrocatalyst	[40]
Ni <sub>2</sub> FeS <sub>4</sub>	Electrocatalyst	[41]
CoIn <sub>2</sub> S <sub>4</sub>	Electrocatalyst	[42]
NiCo <sub>2</sub> S <sub>4</sub>	Dye-sensitized solar cells	[43]

Among metal sulfides, thiospinels draw special attention due to their interconnected diffusion pathways. In addition to being Li-ion and Li-S battery electrodes, thiospinels behave as good electrocatalysts for water splitting, dye-sensitized solar cell electrodes [44], and supercapacitor electrodes [45]. Other than Ni or Co-based sulfides, Mo, Cu, Fe, Mg, Ti, Cr, Zr, Zn, Sn, Cd, and W-based sulfides have also been studied as material groups in the field of electrochemical research.

## 1.2 Aim of This Work

Transition metal oxides are widely used compounds in electrochemical systems. Among them,  $AB_2O_4$  type of metal-oxides exhibit better (two times more) electrical conductivity than MO type metal oxides [46]. Metal sulfides, particularly  $AB_2S_4$  compounds, on the other hand, show 100 times greater electrical conductivity as compared to  $AB_2O_4$ -type metal oxide counterparts [47].

Metal-sulphur bonding allows an easier conversion reaction due to being a weaker bond as compared to the metal-oxide bond because sulfur is less electronegative than oxygen. Thus, metal sulfides exhibit higher efficiency than metal oxide counterparts in terms of conversion reactions in energy research due to the low electronegativity of sulfur as compared to oxygen [48].

In addition to bonding and electrical conductivity, structural features, especially interconnected diffusion pathways and electrochemical activity of  $AB_2S_4$  type metal sulfides, make these material groups remarkable compounds for electrochemistry. Transition metal sulfides exhibit a variety of crystal structures. This variety is advantageous for Li-ion battery systems because it makes both conversion and intercalation reactions possible. Chemical variety is also advantageous for electrocatalysts because electronic structure modification with atoms having different valance states enhances the electrocatalytic activity significantly. **In this regard, this study focuses on the effect of structural and chemical features of metal sulfides on the OER activity as well as the performance as Li-battery (Li-**

**ion or Li-S) electrodes.** Figure 1.2 shows the schematic representation of metal sulfide crystal structures used in this study [49]. The monoclinic structure with a space group no. 12 is given in Figure 1.2 (a).  $\text{Cr}_3\text{S}_4$ ,  $\text{NiCr}_2\text{S}_4$ ,  $\text{CoCr}_2\text{S}_4$  and  $\text{TiCr}_2\text{S}_4$  phases belong to this family. Hexagonal structures with space group no. 194 ( $\text{CoS}$ ,  $\text{NiS}$ ,  $\text{CrS}$ ,  $\text{MoS}_2$ ,  $\text{NiCr}_2\text{S}_4$ ), 155 ( $\text{Ni}_3\text{S}_2$ ) and 148 ( $\text{NiMo}_3\text{S}_4$  or  $\text{Mo}_3\text{S}_4$ ) were given in Figures 2.1 (b), (e) and (g), respectively. The layered structures may enable an intercalation reaction for Li-ions. Figures 2.1 (c), (d) and (f) represents the cubic structures with space group no. 225 ( $\text{Co}_9\text{S}_8$ ), 227 ( $\text{Ni}_3\text{S}_4$  or  $\text{CoCr}_2\text{S}_4$ ) and 205 ( $\text{CoS}_2$ ,  $\text{NiS}_2$ ), respectively. These structures may enable easy intercalation of Li-ions due to their open diffusion pathways. Moreover, the possible sites for Li intercalation are surrounded by sulfur atoms which form an excellent lithium affinity due to attractive coulombic forces between oppositely charged Li and S atoms.

The electrochemical activity of metal sulfides has made these compounds subjects of many studies in the literature. Some of these studies on metal sulfides in electrochemical research are summarized in Table 1.2. Preparing this table, priority was given to Ni, Co, Mo, Cr, and Ti containing compounds (because oxide forms of these elements are the most common electrocatalysts and Li-ion electrodes). These compounds were categorized according to research fields in electrochemistry. As can be seen in Table 1.2 that  $\text{AB}_2\text{S}_4$  type of metal sulfide compounds is very popular in electrochemistry. Studies focus on both the single-metal and bimetallic forms of the Ni and/or Co containing sulfides due to the substantial performance of the oxide forms. Single metal sulfides were represented as Metal-S in the table, indicating all forms of metal sulfides, i.e.,  $\text{NiS}$ ,  $\text{NiS}_2$ ,  $\text{Ni}_3\text{S}_2$ ,  $\text{Ni}_3\text{S}_4$ ,  $\text{CoS}$ ,  $\text{CoS}_2$ ,  $\text{Co}_3\text{S}_4$ ,  $\text{Co}_9\text{S}_8$ ,  $\text{CrS}$ ,  $\text{Cr}_3\text{S}_4$ ,  $\text{MoS}_2$ ,  $\text{Mo}_3\text{S}_4$ .

**In this regard, this study will mainly cover the synthesis of transition metal sulfides and testing electrocatalytic activity in terms of oxygen evolution as well as the performance of these compounds in Li-battery systems.**

Target compositions (except  $\text{NiCo}_2\text{S}_4$  and  $\text{CoNi}_2\text{S}_4$ ) of this study were listed in Table 1.2. Bi-metallic forms and phase mixtures of these compounds are the primary

targets of this study since there are very few studies in electrochemistry of the target compositions. The single-metal forms were used in this study to be a basis for the complex forms. Some of the phase mixtures of the single-metal sulfides which were investigated in this study also have novelty.

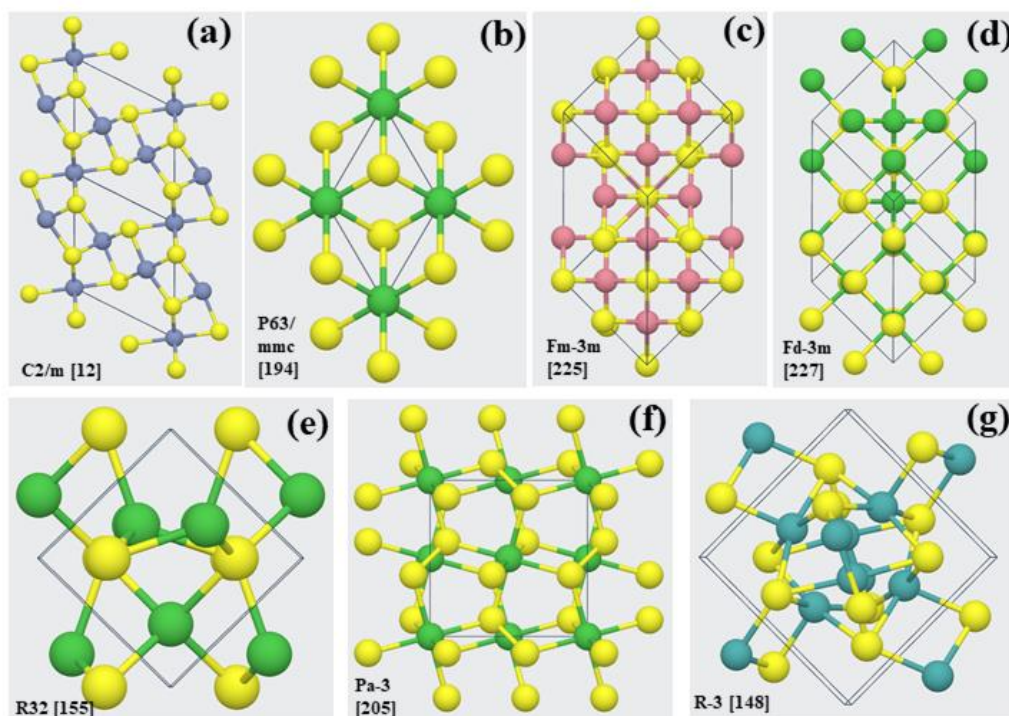


Figure 1.2. Crystal structures of transition metal sulfides used in this study. Yellow spheres represent the sulfur atom and blue/pink/green spheres represent the transition metal sites [49]. Transition metal atoms occupy the same atomic sites in bimetallic compounds.

Electrochemical reactions take place at the surface. Therefore, surface feature plays a vital role in electrochemical performance. Increasing the surface area is the most popular approach to increase the number of active sites, which can be provided by reducing the particle size. Hydrothermal/solvothermal synthesis of metal sulfides is

very common in literature because it is easy to modulate size and morphology by simply controlling the experimental parameters. Long reaction times and slow heating are the shortcomings of this method which can be overcome by using microwave-assisted synthesis. The main superiority of the microwave-assisted synthesis upon hydrothermal method is fast-heating and reaction times as well as being a time and energy-saving procedure by enabling more than one experiment simultaneously. Direct heating (without heating the vessel walls) of the reaction solvent by microwaves is the main reason for these advantages. Reduced reaction times enable the formation of nano-sized particles by microwave-assisted synthesis [50]. **Herein, metal sulfides will be synthesized via a microwave-assisted route and tested as Li-battery electrodes and OER electrocatalysts. Other than the novelty of chosen compounds, microwave-assisted synthesis of these compounds will be the first in the literature.**

Table 1.2 Metal-sulfide studies in literature related to electrochemical applications.

Metal Sulfides	Studies in Literature				
	Supercapacitor	Li-ion/Li-S Battery	Electro-catalysis*	Photo-catalysis	Na-ion/K-ion Battery
Ni-S	[51–53]	[54–56]	[57–60]	[61–63]	[64–66]
Co-S	[67–70]	[71–74]	[58,75–77]	[78–80]	[81–83]
Cr-S	none	[84]	[85]	[86]	[87]
Mo-S	[53,88–90]	[91–94]	[95–98]	[95,99,100]	[101–103]
NiCo <sub>2</sub> S <sub>4</sub>	[40,104–106]	[107–110]	[111–114]	[115,116]	[108,117,118]
CoNi <sub>2</sub> S <sub>4</sub>	[119–122]	[123–126]	[127–131]	[132]	[133–135]
NiCr <sub>2</sub> S <sub>4</sub>	none	none	none	none	[136]
CoCr <sub>2</sub> S <sub>4</sub>	none	none	none	none	none
TiCr <sub>2</sub> S <sub>4</sub>	none	none	none	none	none
NiMo <sub>3</sub> S <sub>4</sub>	[137]	none	[138,139]	none	[140]

\*Electrocatalysts represent the materials studied in hydrogen evolution (HER), oxygen evolution (OER), and oxygen reduction (OER) reactions.

After synthesizing the active materials, the characterization of physical, chemical, and electrochemical features will be carried out. To explain in more detail, morphology, particle size, crystal structure, and phase analysis, chemical composition, electrochemical stability, ionic and electrical conductivity, electrocatalytic activity in water splitting focusing on the OER part and performance as an electrode for Li-ion/Li-S batteries will be investigated. As an electrode, specific capacity, cycle life, rate capability, structural, and cyclic stability measurements will also be performed.

## CHAPTER 2

### LITERATURE REVIEW

In this section, crystal structure, atomic ordering and possible chemistries of the transition metal sulfides were summarized. Synthesis of transition metal sulfides and their performances as electrodes for Li-ion or Li-S battery systems and as electrocatalysts for water splitting reactions focusing on the oxygen evolution part. The theory of microwave-assisted synthesis was also explained since it was one of the synthesis routes used in this study. Then, the theory behind the electrocatalytic reaction focusing on the reaction mechanisms, rate-determining steps and electron transfer reactions and the calculations for measurement criteria, corrections and performance were explained in detail.

#### 2.1 Structure of Metal Sulfides

Metal sulfides with a general formula of  $M_xS_y$  for single-metal forms and  $AB_2S_4$  for bi-metallic forms (used in this study) find a wide range of applications in literature due to their low cost and earth abundance as well as their structural variety [141]. Layered metal sulfides are formed by the presence of transition metal in between the two sulfur atoms (sulfur-metal-sulfur ordering), similar to oxide forms. This layered structure has a tendency to form hollow nanotubes, nanooctahedra and nano onions [142]. Single metal sulfides may have four possible arrangements in the crystal structure. The first one is the sodium chloride (NaCl) type of structure, which is the most significant and symmetrical one where ions occupy the octahedral sites. More than one sulfur-containing compound falls into the pyrite prototype group with a high symmetry where two sulfur atoms occupy each octahedral site. In the case of sphalerite (ZnS), metal atoms are surrounded by six sulfur atoms arranged tetrahedrally. Finally, the metal ion is surrounded by eight sulfur and each sulfur is

surrounded by four metal ions, i.e.,  $\text{CaF}_2$  in fluorite type of structure. In the case of alkali metal sulfides ( $\text{Li}_2\text{S}$ ,  $\text{Na}_2\text{S}$  etc.) anti-fluorite structure is seen, meaning that the metal ion is surrounded by four sulfur and each sulfur is surrounded by eight metal ions [143].

Spinel structure has a general formula of  $\text{AB}_2\text{X}_4$ , where A and B are cations and X is an anion which can be  $\text{O}^{2-}$ ,  $\text{S}^{2-}$ ,  $\text{Se}^{2-}$ ,  $\text{Te}^{2-}$ ,  $\text{N}^{3-}$ ,  $\text{F}^-$ ,  $\text{Cl}^-$ ,  $(\text{CN})^-$ . The crystal structure of spinels generally consists of tetrahedral and octahedral sites. Figure 2.1 shows a typical crystal structure and distinct polyhedral sites of spinels. The brown regions represent the tetrahedral ( $\text{AX}_4$ ) and the blue regions represent the octahedral ( $\text{BX}_6$ ) sites. Tetrahedrons are in distinct regions from each other, but they share corners (where X atoms occupy) with neighboring octahedrons. Octahedrons share six of their twelve X-X edges [144]. Anions are shown as red spheres. Local bonding views of A and B cations were given in Figure 2.1(b) and (c), respectively. Spinel unit cell consists of 8 formula units of  $\text{AB}_2\text{X}_4$  compound. In this unit cell, A and B cations occupy 1/8 and 1/2 of the tetrahedral and octahedral sites, respectively. This ordering is named normal spinel crystal structure ordering. There is also an inverse spinel crystal structure in which A atoms occupy B atom sites and half of the B atoms occupy the A atom sites forming the  $\text{B}(\text{AB})\text{X}_4$  type of compound.

Thiospinels are the sub-groups of the spinel family, where thio- refers to a sulfur element that turns the  $\text{AB}_2\text{X}_4$  compound into an  $\text{AB}_2\text{S}_4$  compound. All the crystal structure features of the spinels are also valid for thiospinels. Thiospinels are also divided into two sub-groups: carrollite and linnaeite. Oxidation states of cations specify these groups. In the carrollite sub-group, the oxidation state of A is +1, while that of B is +3.5. A general chemical formula of the carrollite sub-group can be written as  $\text{A}^+\text{B}_2^{3.5+}\text{S}_4$ , where A can be Cu, Ag, and B can be  $\text{Co}^{3+}/\text{Co}^{4+}$ ,  $\text{Ni}^{3+}/\text{Ni}^{4+}$ ,  $\text{Cr}^{3+}/\text{Cr}^{4+}$ ,  $\text{Ir}^{3+}/\text{Ir}^{4+}$ ,  $\text{Ir}^{3+}/\text{Pt}^{4+}$ ,  $\text{Cr}_{1.5}^{3+}/\text{Sb}_{0.5}^{4+}$ ,  $\text{Fe}_{0.5}^{2+}/\text{Sn}_{1.5}^{4+}$ . The linnaeite sub-group, on the other hand, can be formalized as  $\text{A}^{2+}\text{B}_2^{3+}\text{S}_4$ , where the oxidation states of A and B are +2 and +3, respectively. In this case, A can be Mg, Cd, Fe, Mn, Zn, Pb, Sn, Co, Ni,  $\text{Cu}_{0.5}^+\text{Fe}_{0.5}^{3+}$  and B can be Al, Ga, Ti, V, Ni, Co, Fe, In, Cr, Rh [145].

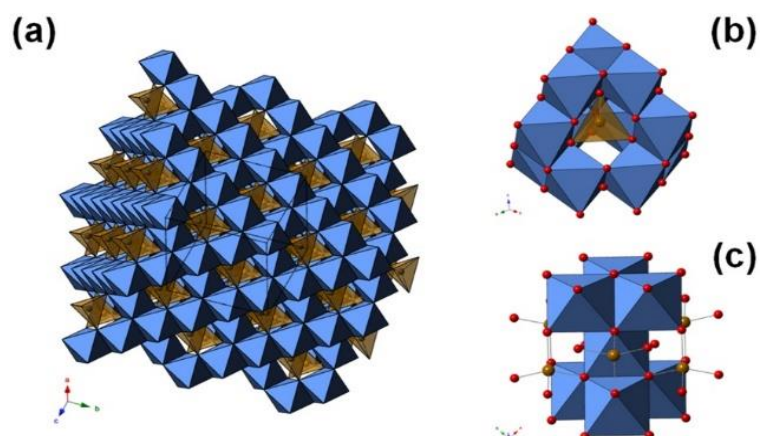


Figure 2.1. Crystal structure (a), local bonding around B (b), and A atoms (c) of spinel compounds [144].

$AB_2S_4$  type of metal sulfide compound has different crystal structures. All  $AB_2S_4$  group does not belong to the spinel family. Cc, P21/m, C2/m, Pnma, I-4, R3m, and P-3m1 are the examples of other space groups that do not belong to the spinel family.

## 2.2 Microwave-Assisted Synthesis

Microwave heating was first introduced in the 1940s by Percy Spencer for food heating. Chemical synthesis by microwaves for scientific use started in the 1980s, which accelerated the publications regarding this method. Now, thousands of articles can be found on the Web of Science. Figure 2.2 (a) demonstrates the number of publications regarding microwave synthesis categorized according to research fields on the web science database until June 2021. The majority of the articles published are related to either chemistry or materials science. The percent distribution of microwave synthesis publications in scientific research is given in Figure 2.2 (b). Chemistry-related publications are 55.73 % of total microwave synthesis publications and among them, 2.15 % of the publications are related to electrochemistry. Organic Chemistry, Physical Chemistry, Analytical Chemistry, Inorganic Nuclear Chemistry, Medicinal Chemistry, Biochemistry, Polymer Science

and Chemical Engineering have percent contributions to Chemistry topic in the pie chart. Materials Science and Engineering, including ceramic materials, crystallography and coating film studies, ranks second in the pie chart with 18.1 %. A wide range of research fields related to microwave synthesis also extends to Physics (11.59 %), Nanoscience and Nanotechnology (4.25 %), Metallurgy and Metallurgical Engineering (1.97 %), as well as other research fields (8.36 %), including Energy Fuels, Green Sustainable Science and Technology, Telecommunications, Environmental Engineering and Electrical Electronic Engineering.

The popularity of this synthesis method comes from its certain advantages over the conventional hydrothermal method and other solution synthesis methods of chemicals. It allows users to synthesize a wide range of material classes, including organic and inorganic materials, bio-based materials, polymers, polymer-metal composites and organometallic materials. This method provides enhanced yields and high purity of the products. Another superiority upon the conventional hydrothermal method is reduced reaction times. Damm et al. [50] suggest using the microwave method in their study to reduce the reaction time to 9 minutes at 9 bar pressure.

The logic behind the rapid reaction times of microwaves is dielectric heating. In this regard, two types of heating mechanisms are proposed: i) Dipolar polarization and ii) Ionic conduction. Microwave irradiation is effective only for dipolar (containing positive and negative charges in its molecular structure) substances. Oscillating microwave fields result in the alignment of dipoles. Dipoles' rotation during alignment causes frictions. The friction in accord with the alignment of dipoles generates heat which is the basis of microwave heating. In the ionic conduction mechanism, heat generation resides oscillation and collision of ions. Oscillations by microwave irradiation result in collisions of the atoms, ions or molecules with each other and generate heat. More rapid heating is predicted for substances with ionic content than pure substances. Dielectric properties are determined by the loss tangent ( $\tan \delta$ ) value which is the ratio of dielectric loss to dielectric constant, where dielectric loss is the efficiency of heat-generating microwave irradiation. In this

manner, 1-Butanol, Nitrobenzene, Methanol, Formic acid, 2-Propanol, DMSO, Ethanol and Ethylene Glycol are the solvent with high ( $\tan \delta > 0.5$ ) loss tangent values. Chlorobenzene, Water ( $\tan \delta = 0.123$ ), Dichloroethane, DMF, Acetic acid, NMP, Dichlorobenzene, 2-Butanol have medium ( $0.1 > \tan \delta > 0.5$ ) loss tangent values while Hexane, Toluene, Dichloromethane, THF, Acetone, Ethyl acetate, Acetonitrile and Chloroform have low ( $\tan \delta < 0.1$ ) loss tangent values. Microwave absorption characteristics determine the heating of substances since metals reflect and materials like glass, PTFE and quartz transmit the microwaves [146].

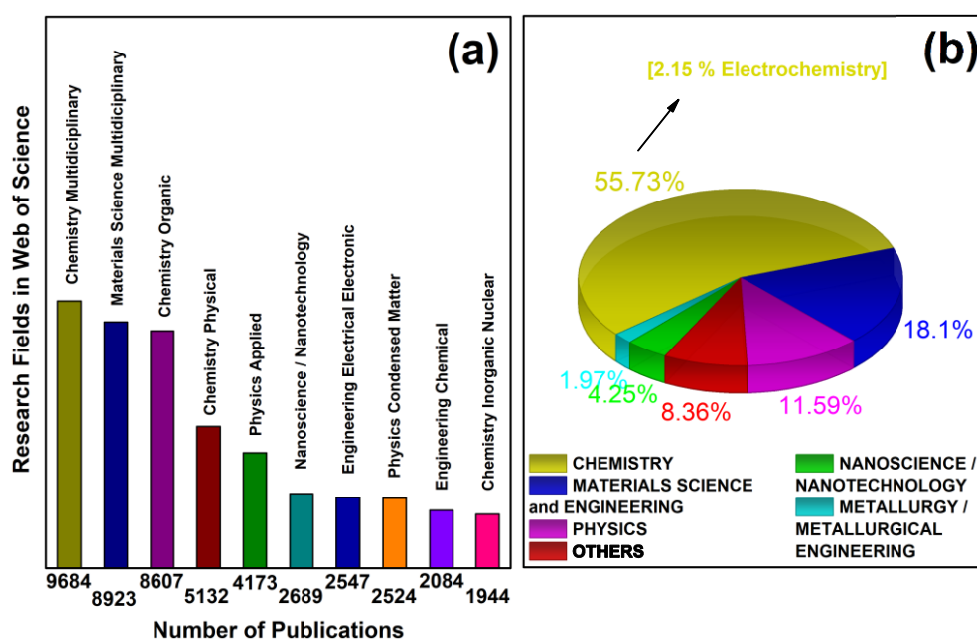


Figure 2.2. (a) A number of publications regarding microwave synthesis categorized according to research fields on the web of science database until 2021, June, (b) Percent distribution of microwave synthesis publications in scientific research.

Enabling the power-controlled as well as the temperature-controlled processes, microwave synthesis provides enhanced reproducibility, parameter control and reaction control. Figure 2.3 shows the heating-cooling profile of a sample heated to

300 °C for 10 minutes. Regions named as a, b and c represent the heating region, temperature holding region and cooling region, respectively [144]. As can be seen in Figure 2.3 that reaching 300 °C takes only a couple of minutes (approximately 2 minutes) and cooling down to the set temperature, which is around 50 °C, takes only shorter than 5 minutes. Reduced reaction times enable the formation of nano-sized particles by microwave-assisted synthesis [50].

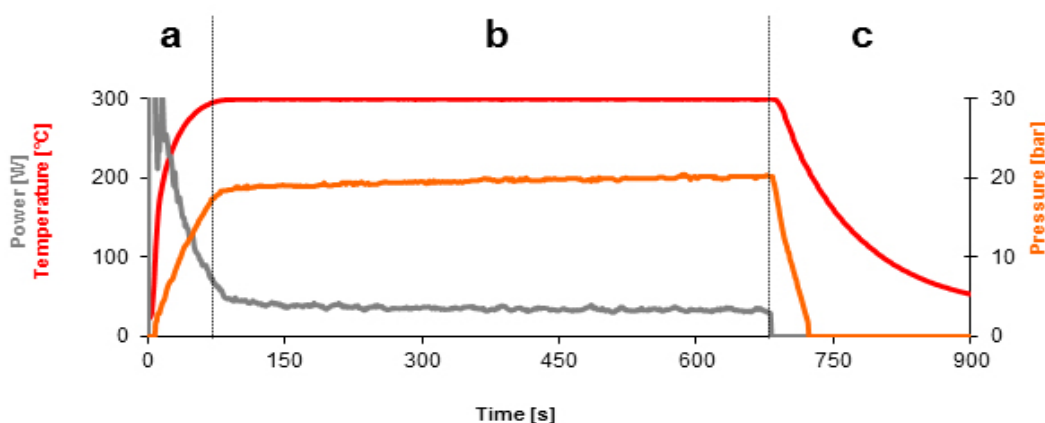


Figure 2.3. Heating-cooling profile of a sample heated to 300 °C for 10 minutes. Regions named as a, b and c represent the heating region, temperature holding region and cooling region, respectively [147].

Allowing simultaneous processes at one time and stirring opportunity of the solutions satisfy homogenous distribution of temperature and effectualness of the results in addition to saving time. Another reason for faster experiment durations of microwave synthesis as compared to hydrothermal processes is the direct heating of substances bypassing the vessel walls. In this way, the reaction mixtures are directly heated by microwaves without heat losses caused by vessel walls which increases the heating efficiency. Moreover, both hydrothermal and microwave-assisted synthesis enable superheating of the substances due to closed (sealed) vessel systems which also reduces reaction times.

### 2.3 Other Synthesis Methods and Performance of Metal Sulfides as Electrocatalysts

The FeNi<sub>2</sub>S<sub>4</sub> compound was synthesized via electrodeposition methods by Ganesan et al. [41] and performed as bi-functional catalysts for water splitting, focusing on both OER and HER characteristics. They achieved improvements in Tafel slope (55 mV/dec), OER (231 mV at 100 mA cm<sup>-2</sup>), and HER (180 mV at 10 mA cm<sup>-2</sup>) overpotentials in 1 M KOH, 200-hours-stability as well as an increase in turnover frequency as compared to RuO<sub>2</sub> and Pt/C catalysts. Wang et al. [148] used a template-free solvothermal method to synthesize the FeNi<sub>2</sub>S<sub>4</sub> compound as an electrocatalyst for OER and reached 237 mV overpotential at 10 mA cm<sup>-2</sup> in 1 M KOH and stability of 10 h. An et al. [149] also focused on bi-functional characteristics of the same compound, but in the form of composite with NiFe<sub>2</sub>O<sub>4</sub> compound to catalyze OER and ORR of air electrode of zinc-air batteries. They claimed that improvement in OER and ORR overpotentials was achieved by heterostructure NiFe<sub>2</sub>O<sub>4</sub>/FeNi<sub>2</sub>S<sub>4</sub> as compared to individual performances of NiFe<sub>2</sub>O<sub>4</sub> and FeNi<sub>2</sub>S<sub>4</sub>. They used the hydrothermal route as a synthesis method and phosphate buffer solution (with pH=7) as an electrolyte to perform both ORR and OER. Jiang et al. [150] synthesized FeNi<sub>2</sub>S<sub>4</sub> nanoparticles via the precipitation method. They investigated the performance of this compound as an OER electrocatalyst and achieved 250 mV overpotential at 10 mA cm<sup>-2</sup> in 1 M KOH.

Ma et al. [151] synthesized FeCo<sub>2</sub>S<sub>4</sub> compound traditionally with hydrothermal method onto Ni-foam. Their electrocatalyst delivered overpotentials of 155 mV at 10 mA cm<sup>-2</sup> and 234 mV at 50 mA cm<sup>-2</sup> in a 1 M KOH electrolyte for HER and OER, respectively. Hu et al. [152] obtained overpotential requirements of 270 mV and 290 mV for OER at 50 mA cm<sup>-2</sup> and 100 mA cm<sup>-2</sup>, respectively, 20-hours-stability for OER, and 132 mV at 10 mA cm<sup>-2</sup> for the HER using the same compound on Ni-foam in 1 M KOH. Similar results were also obtained by Gong et al. [153]. Electrocatalytic activity for OER of this compound was distinctly supported on carbon cloth which enables flexibility by Hu et al. [154]. They achieved an OER overpotential of 317

mV at  $100 \text{ mA cm}^{-2}$  and a small Tafel slope of  $36 \text{ mV dec}^{-1}$  in  $1 \text{ M KOH}$ . Du et al. [155] supported the heterostructure of  $\text{FeCo}_2\text{S}_4/\text{Ni}(\text{OH})_2$  compound onto Ni-foam by hydrothermal method and performed the bi-functional electrocatalytic activity. They stated that this electrocatalyst keeps its  $10 \text{ mA cm}^{-2}$  current density for 140 h in  $1 \text{ M KOH}$ .

Gervas et al. [40] investigated the influence of change in the stoichiometry of transition metals on the electrocatalytic activity of  $\text{Ni}_x\text{Co}_{3-x}\text{S}_4$  compounds and used the precipitation route as a synthesis method. In terms of OER activity,  $89 \text{ mV dec}^{-1}$  and  $90 \text{ mV dec}^{-1}$  Tafel slopes were attained for Ni-rich and Co-rich compositions, whereas Ni-rich and Co-rich compounds exhibited  $161 \text{ mV dec}^{-1}$  and  $176 \text{ mV dec}^{-1}$  as HER activities, respectively. They concluded that Ni-rich stoichiometry exhibit better electrocatalytic activity. He et al. [112] demonstrated the improvements of ORR and OER activity by heterostructure of  $\text{NiCo}_2\text{S}_4/\text{carbon-nitrogen nanosheets}$ . Similarly, Li et al. [113] studied another heterostructure form of  $\text{NiCo}_2\text{S}_4$  compound making  $\text{NiCo}_2\text{S}_4/\text{FeOOH}$  composite and investigated the influence on OER activity. They achieved  $200 \text{ mV}$  overpotential at  $10 \text{ mA cm}^{-2}$  and  $71 \text{ mV dec}^{-1}$  Tafel slope as well as a long-term-durability. Another composite structure was studied by Li et al. [156] to examine the synergistic effect of N-doped  $\text{NiCo}_2\text{S}_4$  together with S-doped  $\text{CeO}_2$  on electrocatalytic activity for biosensors. They achieved comparable ORR activity with the commercial Pt/C catalyst but remarkable improvements as compared to bare  $\text{CeO}_2$ . Xu et al. [114] provided enhancements in the electrocatalytic activity of  $\text{NiCo}_2\text{S}_4$  compound for zinc-air batteries by doping Ag, V, Ti, Mn, Cr, Fe elements with a molar ratio of Ni: Co: Doping element = 9: 9: 2. Among them, Fe, Mn, and Ti-doped samples showed exhibited better kinetics (Tafel slopes of  $57 \text{ mV dec}^{-1}$ ,  $65 \text{ mV dec}^{-1}$ ,  $64 \text{ mV dec}^{-1}$ , respectively) as compared to pristine sample ( $66 \text{ mV dec}^{-1}$ ) for OER while ORR performance of all samples was similar except the Ti-doped sample with a poorer activity. Battery tests were carried out in alkaline solution and they preserved their stabilities upon 100 cycles.

We et al. [157] studied the solvothermal synthesis of  $\text{NiCu}_2\text{S}_4$  and  $\text{CuCo}_2\text{S}_4$  compounds and investigated the electrocatalytic features for OER and ORR. They

observed hollow structures with high surface area, features identical to mesoporous structures, improved electrical conductivity with the synergistic effect of NiCu<sub>2</sub>S<sub>4</sub> and CuCo<sub>2</sub>S<sub>4</sub> compounds, and remarkable reaction kinetics as compared to oxide counterparts.

Li et al. [121] synthesized hybrid CoNi<sub>2</sub>S<sub>4</sub>/Ni<sub>3</sub>S<sub>2</sub> compound onto Ni-foam by hydrothermal method and tested as OER/HER electrocatalyst. OER and HER overpotentials of 360 mV at 30 mA cm<sup>-2</sup> and 173.8 mV at 10 mA cm<sup>-2</sup> and Tafel slopes of 69.7 mV dec<sup>-1</sup> and 98.8 mV dec<sup>-1</sup>, respectively. A stability test was also carried out and 13 hours long term stability was achieved. Similarly, Dai et al. [127] synthesized CoNi<sub>2</sub>S<sub>4</sub>/Ni<sub>3</sub>S<sub>2</sub> nanosheets onto Ni-foam and they reached OER and HER overpotentials of 243 mV and 171 mV at 10 mA cm<sup>-2</sup> in 1 M KOH. Wang et al. [128] used hydrothermal as a synthesis method of CoNi<sub>2</sub>S<sub>4</sub> at Ni-Mn double hydroxide on carbon cloth and performed as bi-functional electrocatalysts for water splitting. They obtained 82, 184, and 224 mV HER overpotentials at 10, 100, and 200 mA cm<sup>-2</sup> current densities. OER overpotentials were attained as 269, 301, 312 mV at 100, 300, and 500 mA cm<sup>-2</sup> current densities, respectively. Ranjith et al. [129] studied another heterostructure form of the CoNi<sub>2</sub>S<sub>4</sub>/carbon nanofiber/graphene oxide layer for water splitting purposes. They achieved 48-hours-stability, 228 mV HER overpotential, and 205 mV OER overpotential at 20 mA cm<sup>-2</sup> in an alkaline medium. Huang et al. [130] used hydrothermal synthesis for CoNi<sub>2</sub>S<sub>4</sub>/CoS<sub>2</sub> heterostructure onto Ni-foam, tested as a bi-functional water splitting electrocatalyst, and achieved OER and HER overpotentials of 259 mV and 173 mV at 10 mA cm<sup>-2</sup>. Rani et al. [131] studied nanostructured CoNi<sub>2</sub>S<sub>4</sub> and NiCo<sub>2</sub>O<sub>4</sub> compounds. They used solvothermal synthesis and obtained nano spherical morphology for both compounds. On the contrary of many studies, they observed better electrocatalytic activity from the oxide form instead of the sulfide form. Tafel slopes are obtained as 66 and 69 mV dec<sup>-1</sup> for NiCo<sub>2</sub>O<sub>4</sub> and CoNi<sub>2</sub>S<sub>4</sub> compounds in 1 M KOH. They also reported that 60% of OER activity was preserved for 20 hours to attain long-term-stability characteristics.

Mao et al. [158] reported the enhancements in the electrocatalytic activity of  $\text{CuNi}_2\text{S}_4/\text{CuWO}_4$  heterostructure for HER. They used the hydrothermal synthesis route and observed the improvements in HER efficiency by Z-type heterostructure construction. Adarakatti et al. [159] used the hydrothermal method as a synthesis route of the graphene- $\text{MoS}_2$ - $\text{CuNi}_2\text{S}_4$  heterostructure. They first exfoliated the graphite powder chemically to obtain graphene, then used the hydrothermal method to get graphene- $\text{MoS}_2$ - $\text{CuNi}_2\text{S}_4$  heterostructure. They improved the hydrogen adsorption efficiency by increasing active adsorption sites by constructing a heterostructure similar to Mao et al. They reported this hybrid compound as a cost-effective substitute of Pt with a remarkable HER activity, efficiency, and kinetics.

$\text{CuCo}_2\text{S}_4$  compound was synthesized with the hydrothermal method, decorated with FeO with magnetron sputtering by Ahmed et al. [160], and tested electrocatalytic activity for HER in alkaline media. They obtained HER overpotential of 107 mV at  $10 \text{ mA cm}^{-2}$  and Tafel slope of  $136 \text{ V dec}^{-1}$ , as well as excellent long-term stability. Hao et al. [161] reported improvements in electrocatalytic activity by self-assembled  $\text{CuCo}_2\text{S}_4$  structure in 1 M KOH. They observed an OER overpotential of 269 mV at  $10 \text{ mA cm}^{-2}$  and a Tafel slope of  $41 \text{ mV dec}^{-1}$ . Shao et al. [162] synthesized the  $\text{CuCo}_2\text{S}_4$  compound on Ni-foam by hydrothermal method and tested its electrocatalytic activity for water splitting and Al-air batteries. They achieved HER and OER overpotentials of 61 mV and 189 mV, respectively, at  $10 \text{ mA cm}^{-2}$  in 1 M KOH. Xu et al. [163] designed  $\text{CuCo}_2\text{O}_4$  onto  $\text{CuCo}_2\text{S}_4$  heterostructure as a bifunctional electrocatalyst for water splitting in alkaline media and achieved HER and OER overpotentials of 101 mV and 240 mV at  $10 \text{ mA cm}^{-2}$ , respectively as well as 36 hours stability at the same current density. Du et al. [164] studied the same  $\text{CuCo}_2\text{S}_4$  on Ni-foam and achieved an OER overpotential of 240 mV at  $50 \text{ mA cm}^{-2}$  and HER overpotential of 142 mV at  $10 \text{ mA cm}^{-2}$ .

## 2.4 Other Synthesis Methods and Performance of Metal Sulfides in Li-ion Battery and Li-S Battery Systems

$\text{FeCo}_2\text{S}_4$  cathode active materials were synthesized with a hydrothermal synthesis method by Guo et al. [165] on a carbon cloth to achieve flexible, binder-free electrodes for Li-sulphur batteries. This study focuses on the absorption behavior of the  $\text{FeCo}_2\text{S}_4$  compound and solves the polysulfide dissolution with this compound. They claim that this compound chemically absorbs the polysulfides, prevents the dissolution of them, and behaves as a catalyst due to an increase in reaction kinetics as a Li-S electrode. This compound exhibited  $1384 \text{ mAh g}^{-1}$  capacity at 0.1C with a 98 % coulombic efficiency.

$\text{NiCo}_2\text{S}_4$  compounds are one of the most studied  $\text{AB}_2\text{S}_4$  type metal sulfides in Li-ion/Li-S battery systems. Zhang et al. [109] synthesized  $\text{NiCo}_2\text{S}_4$  compounds via solution chemistry followed by the hydrothermal method. They achieved a superior high rate performance with  $540 \text{ mAh g}^{-1}$  capacity at 5C and an outstanding cyclic performance upon 800 cycles at 1C with a 0.05 % capacity fading rate for each cycle as a Li-S battery cathode additive. Similar studies on the same compound were carried out by Li et al. [110] and Wu et al. [166]. They both synthesized  $\text{NiCo}_2\text{S}_4$  compounds via the hydrothermal method and achieved  $1387 \text{ mAh g}^{-1}$  capacity at 0.2 C and  $1154 \text{ mAh g}^{-1}$  capacity at 0.1C, respectively. Zhang et al. [167] synthesized this compound traditionally with a hydrothermal method and tested its performance as a Li-ion battery anode. They performed 100 cycles and achieved good cyclic stability as well as a good capacity ( $1060 \text{ mAh g}^{-1}$ ) at  $0.2 \text{ A g}^{-1}$ . Zhang et al. [168] coated this compound with  $\text{SnS}_2$  nanosheets, tested it as a Li-ion battery anode, and achieved  $1260 \text{ mAh g}^{-1}$  capacity at  $0.1 \text{ A g}^{-1}$ .

$\text{CoNi}_2\text{S}_4$  compounds are also one of the most studied  $\text{AB}_2\text{S}_4$  type metal sulfides in Li-ion/Li-S battery systems, similar to  $\text{NiCo}_2\text{S}_4$  compounds. Bhardwaj et al. [123] studied this compound to inhibit polysulfide dissolution in Li-S cathodes as an additive. Jia et al. [124] synthesized  $\text{CoNi}_2\text{S}_4$  compounds with ultrasound-assisted stirring for homogeneous dispersion followed by a hydrothermal method and

achieved 1250 mAh g<sup>-1</sup> reversible capacity at 0.5 A g<sup>-1</sup> in a Li-ion battery system. Giagloglou et al. [169] distinctly synthesized this compound by solid-state reaction route and tested it as a primary Li-thermal battery cathode. They stated that 350 mAh g<sup>-1</sup> capacity was achieved at 500 °C, which is a comparable result with commonly used sulfides (FeS<sub>2</sub>, CoS<sub>2</sub>, and NiS<sub>2</sub>) for the same purpose. Sun et al. [125] and Yang et al. [126] both synthesized the CoNi<sub>2</sub>S<sub>4</sub> compound via the hydrothermal method, tested as Li-ion battery anodes, and achieved discharge capacities of 1575 mAh g<sup>-1</sup> (at 100 mA g<sup>-1</sup>) and 2363 mAh g<sup>-1</sup> (at 3.07 mA g<sup>-1</sup>), respectively.

CuCo<sub>2</sub>S<sub>4</sub> compound are tested as Li-ion battery anodes and 2510 mAh g<sup>-1</sup> at 200 mA g<sup>-1</sup> [170], 792 mAh g<sup>-1</sup> at 500 mA g<sup>-1</sup> [171], 802 mAh g<sup>-1</sup> at 100 mA g<sup>-1</sup> [172], 1715 mAh g<sup>-1</sup> at 100 mA g<sup>-1</sup> [173] and 1081 mAh g<sup>-1</sup> at 100 mA g<sup>-1</sup> [174] capacities were reached in these studies. Cai et al. [175] studied this compound as a cathode and coated it with Li<sub>7</sub>S<sub>3</sub>P<sub>11</sub> electrolyte to create an interface with the solid electrolyte for all-solid-state lithium batteries. As a result, they achieved 1102 mAh g<sup>-1</sup> capacity at 50 mA g<sup>-1</sup>.

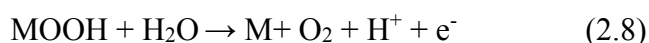
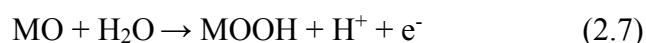
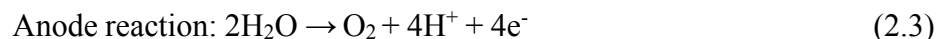
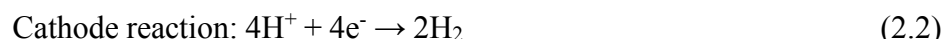
## 2.5 Theory of Electrocatalysis

### 2.5.1 OER Mechanisms

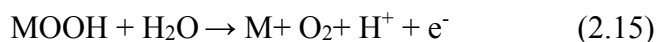
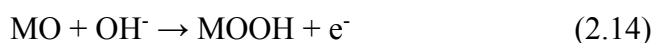
The oxygen evolution reaction (OER) mechanism is based on the adsorption of the reactant ions onto the electrocatalyst surface and the charge transfer between the adsorbed phase and the electrocatalyst. Therefore, reactants in the electrolyte solution significantly affect the electrocatalytic reaction. Oxygen evolution half-reaction of water splitting can be simply expressed by equation 2.1. However, anodic and cathodic half-reactions and the reaction mechanisms take place in different ways in the acidic (equations 2.2-2.8) and the alkaline (equations 2.9-2.15) environments [176].



i) Acidic environment:



ii) Alkaline environment:



### 2.5.2 Single or Multi-Electron Transfer

Tafel slope in electrocatalytic water splitting gives detailed information about the charge transfer mechanism of the electrocatalysts. Tafel slope can be expressed by equation 2.16, where  $R$  is the gas constant ( $8.314 \text{ J mole}^{-1} \text{ K}^{-1}$ ),  $T$  is the absolute temperature,  $a$  is the transfer coefficient which mainly implies the symmetry factor ( $\beta$ ) and  $F$  is the Faraday's constant ( $96485.3 \text{ C mole}^{-1}$ ). In a single electron mechanism, the Tafel slope can be calculated as  $120 \text{ mV dec}^{-1}$  with equation 2.16, where  $a = \beta = 0.5$ , meaning that the rate-determining step is the single-electron transfer step.

$$\text{Tafel slope, } b = (\partial\eta) / \partial \log(i) = (2.303RT) / (aF) \quad (2.16)$$

Bockris and Reddy [177] derived an equation (equation 2.17) related to the transfer coefficient for multi-electron transfer reaction, where  $\nu$  is the number of rate-determining steps,  $n_r$  is the number of electrons participating in the rate-determining step and  $n_b$  is the number of electrons transferring back to the electrode before the rate-determining step.  $n_b$  is equal to 1 when the rate-determining step is the electron transfer and it is equal to 0 when a chemical reaction takes place.

$$a_a = n_b / \nu + n_r\beta \quad (2.17)$$

Considering all this information, calculated Tafel slopes in different scenarios are given in Table 2.1. Tafel slopes were calculated as 120 mV dec<sup>-1</sup>, 60 mV dec<sup>-1</sup> and 30 mV dec<sup>-1</sup> when the rate-determining steps are the first e<sup>-</sup> transfer reaction, the chemical reaction after one e<sup>-</sup> transfer reaction and the third e<sup>-</sup> transfer reaction, respectively [178].

Table 2.1 Calculated Tafel slopes for different rate-determining steps.

<b>Rate-determining step</b>	$n_b$	$\nu$	$n_r$	$\beta$	$a_a$	<b>Tafel slope</b>
First e <sup>-</sup> transfer reaction	0	0	1	0.5	0.5	120 mV dec <sup>-1</sup>
Chemical reaction after one e <sup>-</sup> transfer reaction	1	1	0	1	1	60 mV dec <sup>-1</sup>
Third e <sup>-</sup> transfer reaction	2	1	0	0	2	30 mV dec <sup>-1</sup>

### 2.5.3 Calculations

Electrochemical surface area (ECSA) calculations require electrical double-layer capacitance from the non-Faradaic potential region. The non-Faradaic region can be

determined first from the cyclic voltammetry (CV) measurements carried out within a logical potential window. Another way of choosing a non-Faradaic potential region is using the 0.1 V below the open circuit potential (OCV) as a lower potential limit and 0.1 V above the open circuit potential (OCV) as a higher potential limit. Then, CV measurement can be carried out within this potential window at different scan rates. Figure 2.4 represents the cyclic voltammogram within the non-Faradaic potential region at different scan rates [179].

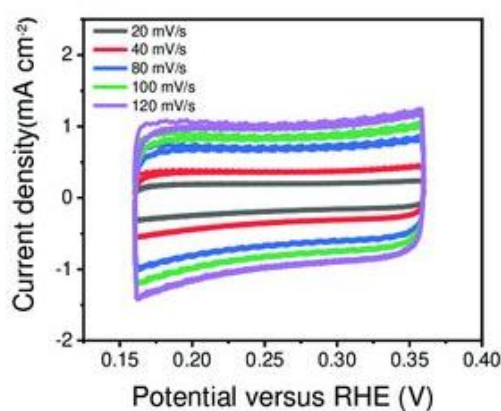


Figure 2.4. Cyclic voltammogram within the non-Faradaic potential region at different scan rates [179].

Electrochemical surface area (ECSA) can be calculated with equation 2.18, where  $C_{dl}$  is the electrical double-layer capacitance and  $C_s$  is the specific capacitance of a flat and atomically smooth surface (in 1.0 M KOH  $C_s=0.04 \text{ mF cm}^{-2}$ ). Electrical double-layer capacitance is equal to the slope of  $\Delta j$  ( $j_{anodic} - j_{cathodic} / \text{mA cm}^{-2}$ ) vs. scan rate ( $\text{mV s}^{-1}$ ) graph, where  $j_{anodic}$  and  $j_{cathodic}$  are the anodic and cathodic current densities at the mid-point potential.

$$ECSA = C_{dl} / C_s \quad (2.18)$$

Roughness factor (RF) can be calculated (Equation 2.19) simply by dividing ECSA to the geometrical surface area (0.196 cm<sup>2</sup>).

$$RF = ECSA / A_{geo} \quad (2.19)$$

The mass activity (A g<sup>-1</sup>) values can be calculated (Equation 2.20) by using the catalyst loading,  $m$  (mg cm<sup>-2</sup>) onto the glassy carbon electrode (with a geometric surface area of 0.196 cm<sup>2</sup>) and the current,  $i$  value corresponding to a logical overpotential, i.e.,  $\eta=0.375$  V. Mass loading values were averaged out of at least 10 measurements, i.e.,  $m_{average} = 0.25$  mg cm<sup>-2</sup>.

$$\text{Mass Activity} = i / m \quad (2.20)$$

Turnover frequency, TOF (s<sup>-1</sup>) values can be calculated by Equation 2.21, where  $j$  (mA cm<sup>-2</sup>) is the current density at a logical overpotential value, i.e.,  $\eta= 0.375$  V,  $A_{geo}$  is the geometric area of the glassy carbon electrode (0.196 cm<sup>2</sup>),  $m_{MW}$  (g mole<sup>-1</sup>) is the molecular weight of the active material,  $n_e$  is the number of electrons per mole of O<sub>2</sub>,  $F$  is the Faraday' s constant (96485.3 C mole<sup>-1</sup>) and  $m$  is the catalyst loading (mg) onto the glassy carbon electrode (with a geometric surface area of 0.196 cm<sup>2</sup>). In order to calculate TOF with Equation 2.21, it should be assumed that each atom in the active material is involved in the catalysis [180].

$$TOF = (j \times A_{geo} \times m_{MW}) / (n_e \times F \times m) \quad (2.21)$$

Onset potential, which was shown in Figure 2.6 (a), is a significant potential indicating the beginning of the oxygen evolution reaction. In other words, it is a start point for OER.

IR-corrected OER overpotentials vs. reversible hydrogen electrode (RHE) can be calculated with equations 2.22, 2.23 and 2.24, where  $i$  (A) is the current,  $R_s$  is the solution resistance (ohm), pH= 14 and  $E^0_{Hg/HgO} = 0.098$  V in 1.0 M KOH aqueous solution. Solution resistance can be obtained with electrochemical impedance spectroscopy (EIS) measurement at OCV and fitting a proper equivalent circuit model to the EIS data.

$$E_{Hg/HgO-corrected} (V) = E_{Hg/HgO} - (i \times R_s) \quad (2.22)$$

$$E_{RHE-corrected} (V) = E_{Hg/HgO-corrected} + E^0_{Hg/HgO} + (0.059 \times \text{pH}) \quad (2.23)$$

$$\eta \text{ (mV)} = (1.23 - E_{RHE-corrected}) \times 1000 \quad (2.24)$$

The electrocatalytic OER activity can be found in the IR-corrected LSV plots. The overpotential value at a current density of  $10 \text{ mA cm}^{-2}$  gives the OER activity, which is the widely used metric relevant in literature. However, the overpotential values at the current densities larger than  $10 \text{ mA cm}^{-2}$  can also be used for comparison. OER activity at a current density of  $50 \text{ mA cm}^{-2}$  was demonstrated in Figure 2.6 (a).

Tafel slope is a significant term in electrocatalysis, giving an idea about the kinetics of electrocatalysis. The smaller Tafel slope indicates the rapid increase in the current density with smaller overpotentials showing fast kinetics, which is a preferred feature in electrocatalysis. Tafel slope can also give information about the reaction mechanism of the electrocatalysis, which was already discussed in section 2.5.2. Figure 2.6 (b) represents the Tafel plot (overpotential (mV) vs. the logarithm of the current density ( $\text{mA cm}^{-2}$ ) plot). The Tafel slope can be calculated from the slope in the linear region of the Tafel plot.

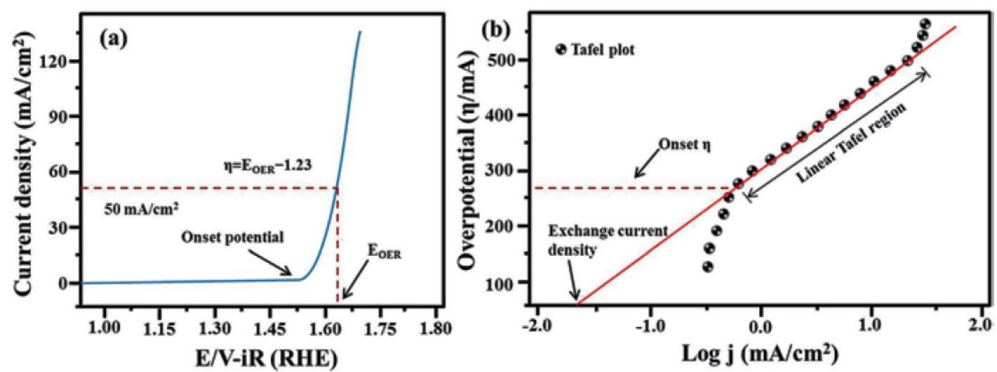


Figure 2.5. (a) Linear sweep voltammogram and (b) Tafel plot [180].

## CHAPTER 3

### EXPERIMENTAL PROCEDURE

Powder synthesis was carried out through two different synthesis routes; *i*) Microwave-assisted solvothermal synthesis and *ii*) Chemical precipitation synthesis. Various mole ratios and heat treatment temperatures were examined. Experimental details and labeling of all samples synthesized via microwave or co-precipitation method were given in Table 3.1.

#### 3.1 Powder Synthesis Procedure

##### 3.1.1 Materials

The precursor salts used in this research and their grades are listed below:

- Nickel(II) nitrate hexahydrate;  $\text{Ni}(\text{NO}_3)_2 \cdot 6\text{H}_2\text{O}$  (Merck, ACS reagent, 99%),
- Cobalt(II) nitrate hexahydrate;  $\text{Co}(\text{NO}_3)_2 \cdot 6\text{H}_2\text{O}$  (Merck, ACS reagent, 99%),
- Chromium (III) nitrate nonahydrate;  $\text{Cr}(\text{NO}_3)_3 \cdot 9\text{H}_2\text{O}$  (Sigma-Aldrich, ACS reagent, 99%),
- Titanium(IV) isopropoxide;  $\text{Ti}[\text{OCH}(\text{CH}_3)_2]_4$  (Sigma-Aldrich, ACS reagent, 99%),
- Ammonium molybdate tetrahydrate;  $(\text{NH}_4)_6\text{Mo}_7\text{O}_{24} \cdot 4\text{H}_2\text{O}$  (Sigma-Aldrich, ACS reagent, 99%),
- Thiourea;  $\text{CH}_4\text{N}_2\text{S}$  (Sigma-Aldrich, ACS reagent, 99%),
- Ethylene glycol;  $\text{C}_2\text{H}_6\text{O}_2$  (Merck, Anhydrous, 99.8%),
- Potassium hydroxide;  $\text{KOH}$  (Merck,  $\text{KOH} > 85.0\%$ , pellets).

### 3.1.2 Microwave-Assisted Solvothermal Synthesis Route

All precursor salts were dissolved in a 400 ml ethylene glycol-deionized water mixture (1:1 v/v) simultaneously under magnetic stirring. Different mole ratios were examined in the microwave-assisted synthesis route. Then, solution mixtures were transferred into Teflon-lined microwave reactors (Anton Paar, Multiwave- Pro). The temperature and reaction time was set to 180 °C and 2 h with stirring mode. The reaction temperature was reached in 5 minutes and cooling to 55 °C took approximately 30 min. After microwave irradiation, precipitates of each sample were collected from the reactor, washed with distilled water and ethanol several times in order, and finally dried at 80 °C under vacuum. All heat treatments were carried out under an N<sub>2</sub> atmosphere for 4 hours. Various mole ratios and heat treatment temperatures were examined.

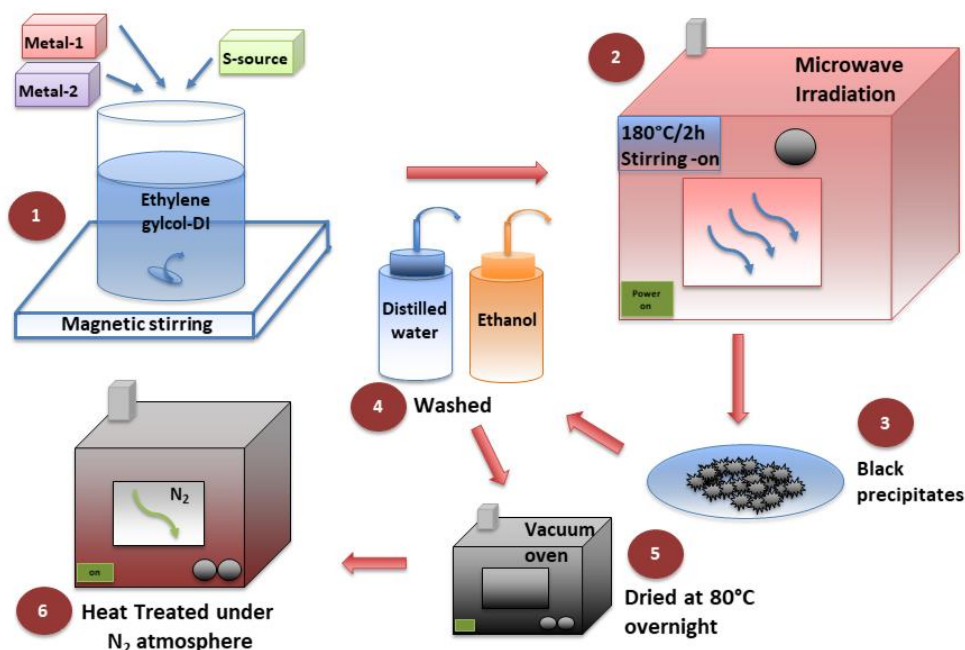


Figure 3.1. Experimental setup for microwave-assisted synthesis route.

### 3.1.3 Chemical Precipitation Route

Transition metal salts and thiourea were dissolved separately in the ethylene glycol. Metal solution with a lower mole ratio was added dropwise into the metal solution with a higher mole ratio. Then this transition metal solution mixture was added dropwise to the sulfur solution. pH values of all solutions were kept below 3.5. The final molarity of all solutions was kept constant at 0.2 M. Then, solution mixtures were refluxed at 180 °C for one hour. Black precipitates were collected, washed with distilled water several times and dried overnight at 100 °C. All heat treatments were carried out under an N<sub>2</sub> atmosphere for 4 hours.

In the case of single metal sulfide synthesis, two different mole ratios were examined; *i*) M:S = 3:7 or *ii*) M:S = 1:12. In the case of bi-metal sulfide synthesis four different mole ratios were studied; *i*) M<sub>1</sub>:M<sub>2</sub>:S = 1:2:12, *ii*) M<sub>1</sub>:M<sub>2</sub>:S = 1:3:12, *iii*) M<sub>1</sub>:M<sub>2</sub>:S = 1:2:16 and *iv*) M<sub>1</sub>:M<sub>2</sub>:S = 1:2:16. Synthesized powders were heat-treated at 300 °C, 400 °C, 450 °C, 500 °C, 600 °C, 750 °C and 900 °C. Some heat treatments resulted in more than two phases, while some resulted in no crystal structure being formed. Therefore, those samples were not used further in this study and were excluded from Table 3.1. The samples listed in Table 3.1 were investigated in detail in terms of chemistry, structure, morphology and particle size.

Table 3.1 Experimental details and sample labeling.

<b>Mole ratio of the precursors</b>	<b>Sample labeling</b>	<b>Synthesis method</b>	<b>Heat treatment temp. (°C)</b>
Co:S = 3:7	CoS	Precipitation	400
Co:S = 3:7	CoS/Co <sub>9</sub> S <sub>8</sub>	Precipitation	450
Co:S = 3:7	Co <sub>9</sub> S <sub>8</sub>	Precipitation	900
Co:Cr:S = 1:2:12	Cr <sub>3</sub> S <sub>4</sub> /CoCr <sub>2</sub> S <sub>4</sub>	Precipitation	900
Co:Cr:S = 1:2:12	CoCr <sub>2</sub> S <sub>4</sub>	Microwave	900

Table 3.1 (cont'd)

Co:Cr:S = 1:0.5:12	Cr/CoS <sub>2</sub>	Microwave	450
Co:Mo:S = 1:0.5:12	Mo/Co <sub>9</sub> S <sub>8</sub>	Microwave	450
Ni:S = 3:7	NiS-pp	Precipitation	400
Ni:S = 3:7	NiS-mw	Microwave	400
Ni:S = 1:12	NiS/NiS <sub>2</sub>	Microwave	400
Ni:S = 1:12	NiS/Ni <sub>3</sub> S <sub>2</sub>	Microwave	900
Ni:Cr:S = 1:2:12	Ni-Cr-S	Microwave	none
Ni:Cr:S = 1:2:12	NiS <sub>2</sub> /CrS	Microwave	300
Ni:Cr:S = 1:2:12	NiCr <sub>2</sub> S <sub>4</sub> -194	Microwave	450
Ni:Cr:S = 1:2:12	NiCr <sub>2</sub> S <sub>4</sub> -12/CrS	Precipitation	450
Ni:Cr:S = 1:2:12	NiCr <sub>2</sub> S <sub>4</sub> -12	Precipitation	900
Ni:Cr:S = 1:2:16	NiS <sub>2</sub> /NiCr <sub>2</sub> S <sub>4</sub> -12	Precipitation	900
Ni:Cr:S = 3:0.2:7	Cr/NiS	Microwave	450
Ni:Mo:S = 1:3:16	Ni <sub>3</sub> S <sub>4</sub> /NiMo <sub>3</sub> S <sub>4</sub>	Microwave	300
Ni:Mo:S = 1:3:16	Ni <sub>3</sub> S <sub>2</sub> /MoS <sub>2</sub>	Microwave	900
Ti:Cr:S = 1:2:12	TiCr <sub>2</sub> S <sub>4</sub>	Microwave	900

## 3.2 Characterization Methods

### 3.2.1 Structural Characterization

X-ray diffractometer (XRD, Bruker D8 Advance, CuK $\alpha$ ) was used to analyze the crystal structure of the samples. Rietveld refinement was carried out with Material Analysis Using Diffraction (MAUD) software [181] for crystal structure analysis. Morphology, chemical composition (EDS analysis) and EDS-mapping of the samples were investigated by field emission scanning electron microscopy (FE-SEM, Nova NanoSEM 430). Electronic structure and valance state designation were investigated by X-ray photoelectron spectroscopy (XPS, PHI 5000 VersaProbe, Al

$K\alpha$ ,  $h\nu=1486.6$  eV). Savitzky-Golay filter was applied for the purpose of smoothing the XPS data. After background subtraction, Gaussian peak fitting was applied for the deconvolution of the XPS peaks. Quantachrome Corporation, Autosorb-6 analyzer recorded  $N_2$  adsorption/desorption isotherms. The preheating temperature was set at 200 °C for 12 h to remove surface inhomogeneities. Brunauer Emmett Teller (BET) surface area, pore size and pore volume of the powders were calculated from the adsorption data.

Electrical conductivity measurements were carried out when considered to be necessary for the powders using a 2-probe direct current measurement system.

### **3.2.2 Electrode (Electrocatalyst) Preparation and Cell Configuration**

Active material, carbon (Printex L6 as conductive additive) and Nafion solution (5 % in isopropyl alcohol as a binder) were mixed with a mass ratio of 70:15:15, respectively in ultrapure water- isopropyl alcohol solvent mixture (4:1, v/v) by sonicator for 30 min in an ice-bath. Glassy carbon (5 mm diameter, as a rotating disc working electrode) was polished to a mirror finish before 10  $\mu$ l of catalyst mixture was dropped onto it. 1.0 M KOH (Merck, KOH > 85.0%, pellets) aqueous solution, graphite rod and Hg/HgO (1.0 M KOH) were used as an electrolyte, a counter electrode and a reference electrode, respectively. Tests were carried out at 1600 rpm and with a continuous oxygen gas flow through the electrolyte solution by Gamry, the RDE710 Rotating Electrode instrument.

Cyclic voltammetry (CV), linear sweep voltammetry, chronopotentiometry (CP) and electrochemical impedance spectroscopy (EIS) measurements were carried out by potentiostat/galvanostat (Bio-Logic Science Instruments, VMP-300). Cyclic voltammograms in the non-Faradaic region were obtained between 0.0-0.2 V vs. Hg/HgO at scan rates of 50, 100, 200, 500, 1000, 2000  $mV s^{-1}$  for electrochemical surface area (ECSA) and roughness factor (RF) calculations. Cyclic voltammetry with a 250  $mV s^{-1}$  sweep rate upon 100 cycles and linear sweep voltammetry (LSV)

with a 5 mV s<sup>-1</sup> scan rate were carried out from 0 V to 0.8 V vs. Hg/HgO. Stability tests were carried out with a chronopotentiometry (CP) method for 20 hours at a constant current density of 10 mA cm<sup>-2</sup>. Electrochemical impedance spectroscopy (EIS) data were collected from 100 kHz to 100 mHz with ±5 mV voltage amplitude at two different potential values (at 1.52 V and 1.62 V vs. RHE).

### **3.2.3 Electrode (Li-Battery) Preparation, Cell Configuration and Testing Procedure**

Active materials, carbon black (Super carbon C65 as conducting additive) and NMP-PVDF solution (5% PVDF) were mixed in a mixer mill with a mass ratio of 80:10:10 or 60:20:20, respectively. The slurry was coated on Cu-foil and Al-foil current collectors separately to investigate active materials' performance within a wider potential window. The coating was carried out by a doctor blade and the thickness of the slurry was set as 200 μm. Coated films were pre-dried at 120 °C for 2 h on a hot plate; then, they were cut into 18 mm discs and dried under vacuum overnight at 120 °C. Electrochemical cells were assembled in an argon-filled glove box. Lithium foil and glass microfiber paper were used as counter electrodes and separators. 1.5 M LiPF<sub>6</sub> in EC: EMC: DMC (3: 4: 3, v/v), 0.5% VC, 1 % AB43 solution was used as an electrolyte. First discharge capacities of the electrodes, which were coated onto Cu-foil, were tested with a 50 mA g<sup>-1</sup> constant current density between 0.01 V- 2V. Electrodes coated onto Al-foil were tested with a 0.2 mA constant current between 2.5 V- 4 V to obtain the capacitive performance as Li-battery cathodes.

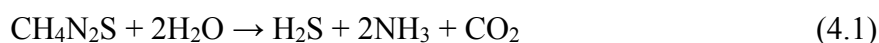
## CHAPTER 4

### RESULTS AND DISCUSSION

In this section, reaction mechanisms, structural features, electrocatalytic performance for OER and performance as Li-battery electrodes were investigated in detail. In the first section of this chapter, the reaction mechanisms for the formation of metal sulfides from the thiourea (sulfur source) in the microwave-assisted synthesis route were explained in detail. In the second section, structural, morphological and chemical characterizations of the samples were carried out. In the third section, electrocatalytic performance for oxygen evolution reaction (OER) focusing on the activity and kinetic features were investigated. Finally, samples were tested as Li-battery electrodes to present the capacitive behavior of the metal sulfides.

#### 4.1 Reaction Mechanism of Microwave-Assisted Synthesis of Metal Sulfides

One of the synthesis routes used in this study was the microwave-assisted solvothermal route. Thiourea ( $\text{CH}_4\text{N}_2\text{S}$ ) was used as a sulfur source and ethylene glycol-deionized water mixture (1:1 v/v) was used as a solvent. The reaction mechanism of metal sulfide formation in this method was given in Equations 4.1-4.5. In the first step, thiourea dissolves in water and forms  $\text{H}_2\text{S}$  and  $\text{NH}_3$  gases (Equation 4.1). Then metal ions in the solution react with  $\text{NH}_3$  and form a  $[\text{M}(\text{NH}_3)_4]^{(4-a)}$  ligand (Equation 4.2).  $\text{NH}_3$  also reacts with water molecules to form  $\text{OH}^-$  and  $\text{NH}_4^+$  ions (Equation 4.3).  $\text{H}_2\text{S}$  molecule formed in the first step and  $\text{OH}^-$  ions formed in the third step reacts to form  $\text{S}^{2-}$  ion (Equation 4.4). Finally, the sulfur ions react with the ligand formed in the second step to generate the metal sulfide compound [143].



## 4.2 Structural, Morphological and Chemical Characterization of the Transition Metal Sulfides

In this section, structural, morphological and chemical characterization of the samples was carried out. X-ray diffractometer (XRD, Bruker D8 Advance,  $\text{CuK}\alpha$ ) was used to analyze the crystal structure of the samples. Rietveld refinement was carried out with Material Analysis Using Diffraction (MAUD) software [181] for crystal structure analysis. XRD pattern and the quantitative phase analysis results, together with the crystal structure information of the samples, were given in Figure 4.1 and Table 4.1, respectively. Vertical dashed lines represent the Bragg positions of the related phases. Single-phase metal sulfides with space groups P63/mmc (no. 194) and C2/m (no. 12) were demonstrated in Figures 4.1(a) and (b), respectively. NiCr<sub>2</sub>S<sub>4</sub> sample is actually Ni<sub>0.25</sub>Cr<sub>0.5</sub>S phase which can be named as the Cr incorporated NiS structure. The reason is that the number of atoms in the NiS structure is similar to Ni<sub>0.25</sub>Cr<sub>0.5</sub>S. However, there is a certain difference between the stoichiometry of the Ni<sub>0.25</sub>Cr<sub>0.5</sub>S and NiS phases since 75 % of the transition metal site is occupied in the Ni<sub>0.25</sub>Cr<sub>0.5</sub>S. In other words, there is a deficient amount of transition metals in the Ni<sub>0.25</sub>Cr<sub>0.5</sub>S structure. In Figure 4.1(a), Ni-based sulfides showed small peak shifts due to the chemical composition differences. Cr incorporation to the NiS structure shifted peak positions to the smaller angles due to an increase in the lattice parameters since the ionic radius of Cr<sup>2+</sup> ion is larger (0.73 Å) than that of Ni<sup>2+</sup> (0.69 Å). CoS structure exhibited a notable peak shift with respect to NiS because of the lattice parameter differences arising from the chemistry

difference. The ionic radius of the  $\text{Co}^{2+}$  ion in the CoS phase is 0.65 Å since the ionic radius of the  $\text{Ni}^{2+}$  ion in the NiS phase is 0.69 Å [106]. The difference between the ionic radii of  $\text{Co}^{2+}$  and  $\text{Ni}^{2+}$  ions results in the difference in lattice parameters causing peak shifts. The peak shift to the smaller angles indicates the increase in lattice parameter explaining the peak shift to larger angles of the CoS phase.

Table 4.1 Phase analysis and crystal structure information.

Sample	Phase 1	Space Group & No	Phase 2	Space Group & No
CoS	%100 CoS	P63/mmc, 194	x	x
CoS/Co9S8	73% CoS	P63/mmc, 194	27% Co9S8	Fm-3m, 225
Co9S8	100% Co9S8	Fm-3m, 225	x	x
Cr3S4/CoCr2S4	98% Cr3S4	C2/m, 12	2% CoCr2S4	Fd-3m, 227
CoCr2S4	100% CoCr2S4	C2/m, 12	x	x
Cr/CoS2	100% CoS2	Pa-3, 205	x	x
Mo/Co9S8	100% Co9S8	Fm-3m, 225	x	x
NiS-pp	100% NiS	P63/mmc, 194	x	x
NiS-mw	100% NiS	P63/mmc, 194	x	x
NiS/NiS2	80% NiS	P63/mmc, 194	20% NiS2	Pa-3, 205
NiS/Ni3S2	25% NiS	P63/mmc, 194	75% Ni3S2	R32, 155
NiS2/CrS	85% NiS2	Pa-3, 205	15% CrS	P63/mmc, 194
NiCr2S4-194	100% NiCr2S4	P63/mmc, 194	x	x
NiCr2S4-12/CrS	98% NiCr2S4	C2/m, 12	2% CrS	P63/mmc, 194
NiCr2S4-12	100% NiCr2S4	C2/m, 12	x	x
NiS2/NiCr2S4-12	5% NiS2	Pa-3, 205	95% NiCr2S4	C2/m, 12
Cr/NiS	100% NiS	P63/mmc, 194	x	x
Ni3S4/NiMo3S4	86% Ni3S4	Fd-3m, 227	14% NiMo3S4	R-3, 148
Ni3S2/MoS2	81% Ni3S2	R32, 155	19% MoS2	P63/mmc, 194
TiCr2S4	100% TiCr2S4	C2/m, 12	x	x

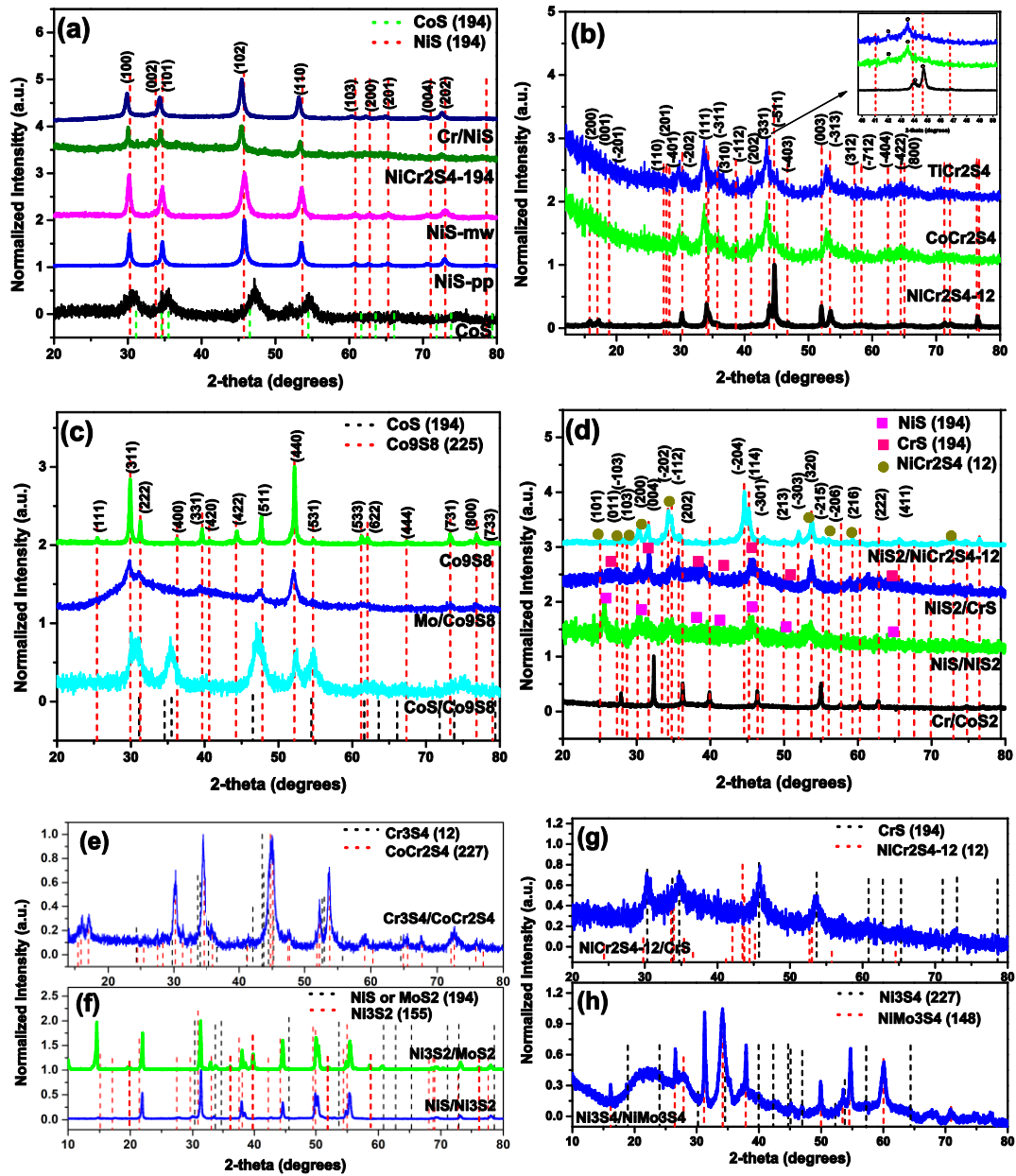


Figure 4.1. XRD pattern of single-phase metal sulfides with space group no (a) 194, (b) 12 and (c-h) phase mixtures.

Figure 4.1(c) demonstrates the cobalt sulfides with different crystal structures.  $\text{Co}_9\text{S}_8$  is a high-temperature phase formed at 900 °C with a cubic crystal structure (space group:  $\text{Fm}\bar{3}\text{m}$ , no.225). Keeping the Co:S ratio constant (Co: S=3:7), the CoS phase

with a hexagonal structure (space group: P63/mmc, no.194) was formed when heat treatment was carried out at 400 °C. When the heat treatment temperature was set to 450 °C, a phase mixture containing 27%  $\text{Co}_9\text{S}_8$  and 73%  $\text{CoS}$  was observed as expected. However, other than the temperature effect, the composition may be another reason for the formation of different crystal structures. An excess amount of sulfur was used to synthesize all-metal sulfides in this study since melting (115 °C) and evaporation (446 °C) temperatures are relatively small for the sulfur, causing sulfur losses at high temperatures.  $\text{CoS}$  phase tends to form in sulfur deficiency. These results are in good agreement with the Co-S binary phase diagram, which was given in Figure 4.2 [182].

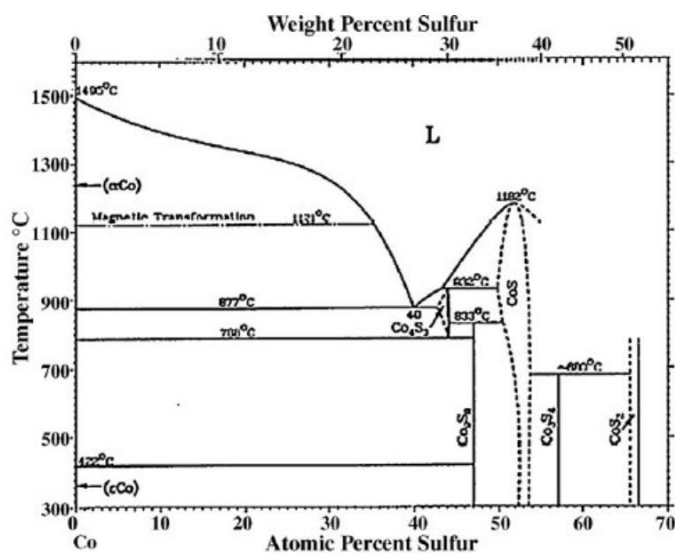


Figure 4.2. Binary phase diagram of cobalt and sulfur [182].

Chemical compositions and homogeneity of the samples were analyzed by energy dispersive spectroscopy (EDS) and EDS-mapping techniques, respectively. EDS results are given in Table 4.2. Most of the compositions agree with the target compositions with minor deviations. However, sulfur deficiency was still observed despite the addition of extra sulfur during the synthesis of all samples, which may be

one of the reasons for the secondary phase formation. Keeping the mole ratio constant and increasing the heat treatment temperature, a decrease in the sulfur contents in EDS measurements were observed for CoS, CoS/Co<sub>9</sub>S<sub>8</sub> and Co<sub>9</sub>S<sub>8</sub> samples gradually due to the volatility of the sulfur. EDS analysis showed that cobalt and sulfur contents are still acceptable values due to being very close to the stoichiometric amounts. Although an excessive amount of sulfur was used during the synthesis (mole ratio of Co:Mo: S=1:0.5:12) of the Mo/Co<sub>9</sub>S<sub>8</sub> sample, Mo addition to the Co<sub>9</sub>S<sub>8</sub> structure caused sulfur deficiency, i.e., Co:Mo: S=47:10:43 at.%, which led the formation of single-phase Mo incorporated Co<sub>9</sub>S<sub>8</sub> at much lower temperatures (at 450 °C). The lattice parameter, *a* of the cubic Co<sub>9</sub>S<sub>8</sub> has increased from 9.93 Å to 10.39 Å with Mo addition which is an indication of the successful incorporation of Mo to the Co<sub>9</sub>S<sub>8</sub> structure.

Figure 4.1 (d) demonstrates the XRD patterns of Cr/CoS<sub>2</sub>, NiS/NiS<sub>2</sub>, NiS<sub>2</sub>/CrS and NiS<sub>2</sub>/NiCr<sub>2</sub>S<sub>4</sub> samples. As shown in Table 4.1 that NiS<sub>2</sub> and CoS<sub>2</sub> samples have the same cubic crystal structure with a space group of Pa-3, no:205, which was established as dashed, red, vertical lines in Figure 4.1 (d). Chromium incorporation did not cause any phase transformation or secondary phase formation. Increase in lattice parameter, *a* of the cubic CoS<sub>2</sub> phase from 5.46 Å to 5.51 Å. Secondary phase formation was observed when the mole ratio of metal to sulfur increased from 3:7 to 1:12 for nickel sulfides. NiS-NiS<sub>2</sub> (Figure 4.1(d), green line) and NiS-Ni<sub>3</sub>S<sub>2</sub> (Figure 4.1(f), blue line) phase mixtures were obtained with microwave synthesis at 400 °C and 900 °C, respectively, when the precursor mole ratio was set to Ni: S=1:12. NiS<sub>2</sub>-CrS phase mixture formed at 300 °C when the mole ratio was set to Ni:Cr: S=1:2:12. Keeping the mole ratio constant, single-phase NiCr<sub>2</sub>S<sub>4</sub> phases with two different crystal structures formed (space group of P63/mmc, no.194 at 450 °C and space group of C2/m, no.12 at 900 °C). An increase in sulfur content resulted in the formation of the NiS<sub>2</sub>-NiCr<sub>2</sub>S<sub>4</sub> phase mixture at 900 °C when the mole ratio was set to Ni:Cr: S=1:2:16.

Table 4.2 EDS results of the samples in terms of at. %.

<b>Sample</b>	<b>Atom Percent Compositions</b>
CoS	Co= 49 at.%, S= 51 at.%
CoS/Co <sub>9</sub> S <sub>8</sub>	Co= 50 at.%, S= 50 at.%
Co <sub>9</sub> S <sub>8</sub>	Co= 58 at.%, S= 42 at.%
Cr <sub>3</sub> S <sub>4</sub> /CoCr <sub>2</sub> S <sub>4</sub>	Co= 17 at.%, Cr= 30 at.%, S= 53 at.%
CoCr <sub>2</sub> S <sub>4</sub>	Co= 15 at.%, Cr= 19 at.%, S= 66 at.%
Cr/CoS <sub>2</sub>	Co= 16 at.%, Cr= 50 at.%, S= 34 at.%
Mo/Co <sub>9</sub> S <sub>8</sub>	Mo= 47 at.%, Co= 10 at.%, S= 43 at.%
NiS-pp	Ni= 41 at.%, S= 59 at.%
NiS-mw	Ni= 51 at.%, S= 49 at.%
NiS/NiS <sub>2</sub>	Ni= 24 at.%, S= 76 at.%
NiS/Ni <sub>3</sub> S <sub>2</sub>	Ni= 60 at.%, S= 40 at.%
Ni-Cr-S	Ni= 22 at.%, Cr= 32 at.%, S= 46 at.%
NiS <sub>2</sub> /CrS	Ni= 15 at.%, Cr= 47 at.%, S= 38 at.%
NiCr <sub>2</sub> S <sub>4</sub> -194	Ni= 21 at.%, Cr= 33 at.%, S= 46 at.%
NiCr <sub>2</sub> S <sub>4</sub> -12/CrS	Ni= 16 at.%, Cr= 47 at.%, S= 37 at.%
NiCr <sub>2</sub> S <sub>4</sub> -12	Ni= 17 at.%, Cr= 37 at.%, S= 46 at.%
NiS <sub>2</sub> /NiCr <sub>2</sub> S <sub>4</sub> -12	Ni= 14 at.%, Cr= 32 at.%, S= 54 at.%
Cr/NiS	Ni= 46 at.%, Cr= 2 at.%, S= 52 at.%
Ni <sub>3</sub> S <sub>4</sub> /NiMo <sub>3</sub> S <sub>4</sub>	Ni= 62 at.%, Mo= 21 at.%, S= 17 at.%
Ni <sub>3</sub> S <sub>2</sub> /MoS <sub>2</sub>	Ni= 44 at.%, Mo= 14 at.%, S= 42 at.%
TiCr <sub>2</sub> S <sub>4</sub>	Ti= 18 at.%, Cr= 35 at.%, S= 47 at.%

Chromium addition to cobalt sulfide with a mole ratio of Co:Cr: S=1:2:12 resulted in the formation of Cr<sub>3</sub>S<sub>4</sub>-CoCr<sub>2</sub>S<sub>4</sub> phase mixture at 900 °C when chemical precipitation was used as a synthesis route (Figure 4.1(e)). However, a single-phase CoCr<sub>2</sub>S<sub>4</sub> (space group of C2/m, no.12) structure has formed by applying the same experimental conditions and heat treatment procedures to the microwave-assisted synthesis route (Figure 4.1(b), green line). Similarly, chromium addition to nickel sulfide with a mole ratio of Ni:Cr: S=1:2:12 resulted in the formation of a single-

phase  $\text{NiCr}_2\text{S}_4$  (space group of P63/mmc, no.194) structure at 450 °C when chemical precipitation was used as a synthesis route (Figure 4.1(a), green line). However, the  $\text{NiCr}_2\text{S}_4$ -CrS phase mixture has formed by applying the same experimental conditions and heat treatment procedures to the microwave-assisted synthesis route (Figure 4.1(g)). The structural differences can be due to the compositional differences arising from the precursor mole ratio, reaction duration or the inertness of the reaction atmosphere. Precipitation was carried out in an open atmosphere (at 1 atm pressure); however, microwave synthesis was carried out in a closed vessel with a pressure larger than atmospheric pressure causing differences in the reaction mechanisms. Molybdenum addition to nickel sulfide structure with a mole ratio of Ni:Mo:S=1:3:16 resulted in the formation of  $\text{Ni}_3\text{S}_2$ - $\text{MoS}_2$  (Figure 4.1(f), green line) and  $\text{Ni}_3\text{S}_4$ - $\text{NiMo}_3\text{S}_4$  (Figure 4.1(h)) phase mixtures at 900 °C and 300 °C, respectively.

Morphology of the samples was investigated by field emission scanning electron microscopy (FE-SEM, Nova NanoSEM 430). SEM micrographs of the samples were given in Figures 4.3 and 4.4. Figure 4.3 demonstrates the SEM micrographs of the samples synthesized via precipitation. Particle size and morphology exhibit different characteristics due to the differences in the synthesis procedure, heat treatment temperature/time and chemical content. However, the physical properties like the size and morphology of the particles significantly affect the electrochemical performance. Electrochemical events are surface reactions that impute a great significance to surface features. All samples except NiS-pp yielded irregularly-shaped, sub-micron-sized primary particles. NiS-pp sample is composed of spherical particles and the size of these spheres is much smaller than the particles of the other samples. Phase mixtures did not exhibit significant morphological differences, which can be seen in Figures 4.3 (b), (d), (f), (g). The SEM micrographs of the samples synthesized via microwave were given in Figure 4.4. Similarly, all samples except three samples (NiS/ $\text{Ni}_3\text{S}_2$ , Ni-Cr-S, Cr/NiS) yielded irregularly-shaped, sub-micron-sized primary particles. Spherical particles tend to form in the nickel sulfides within the experimental conditions in both of the synthesis routes of this study.

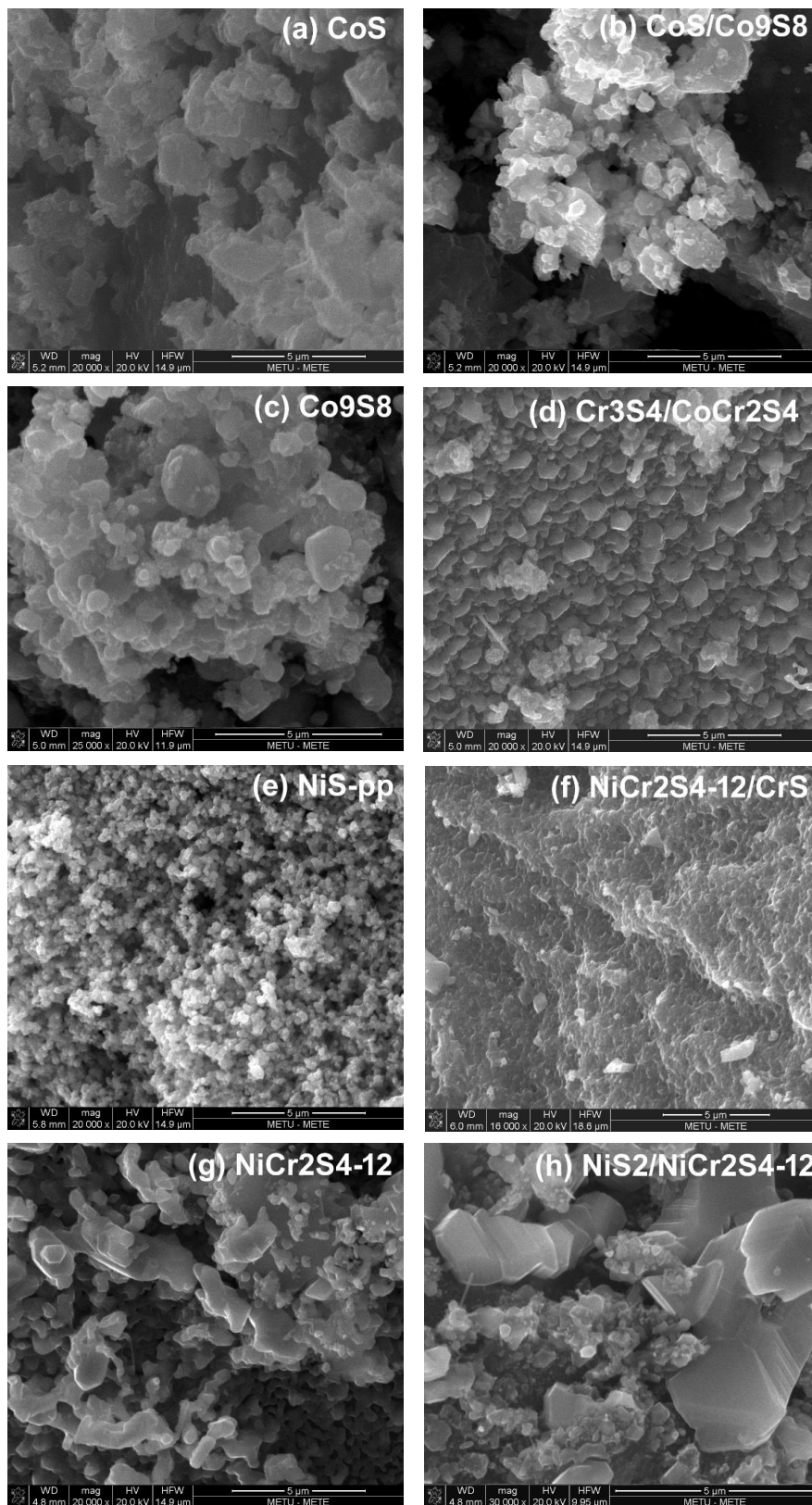


Figure 4.3. SEM micrographs of the samples synthesized via precipitation.

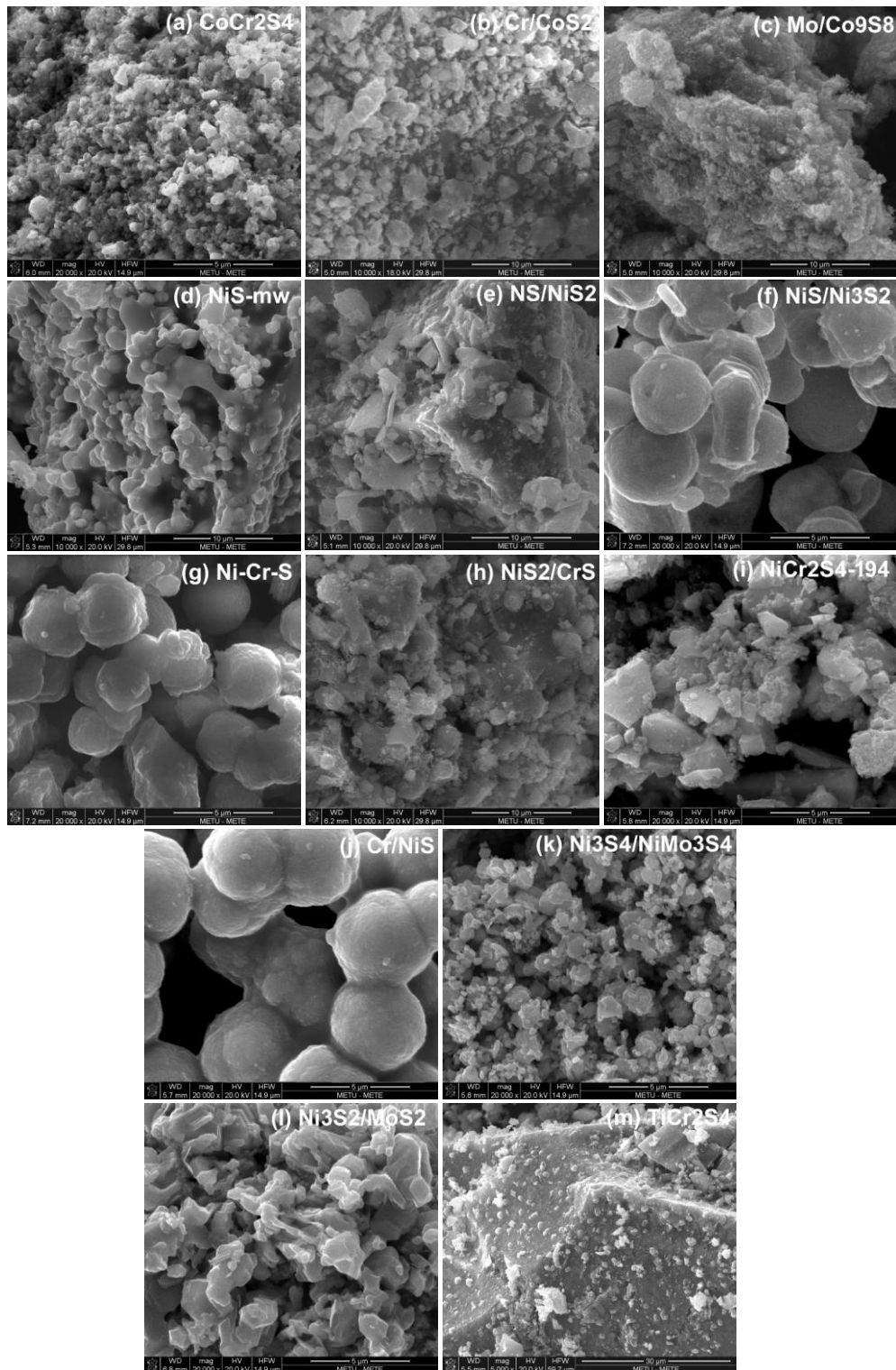


Figure 4.4. SEM micrographs of the samples synthesized via microwave.

The metal sulfides synthesized in this study were investigated in terms of chemical composition, morphology and crystal structure. Electrochemical performance tests were applied to samples with compositions matching well with the target chemical composition. Moreover, structural information such as phase analysis results and crystallographic information were also used choosing the samples for electrochemical analysis. Therefore, CoS, Co<sub>9</sub>S<sub>8</sub>, CoCr<sub>2</sub>S<sub>4</sub>, NiS-mw, NiCr<sub>2</sub>S<sub>4</sub>-194, NiCr<sub>2</sub>S<sub>4</sub>-12, Cr/NiS, TiCr<sub>2</sub>S<sub>4</sub> and Ni-Cr-S samples were determined to be further examined in terms of OER activity and OER kinetics.

### **4.3 Electrochemical Characterization of Transition Metal Sulfides as OER Electrocatalysts**

In this section, transition metal sulfides were tested as OER electrocatalysts. Firstly, the effects on the OER activity and kinetics of chromium incorporation to the NiS structure were investigated. Then, ACr<sub>2</sub>S<sub>4</sub> (A= Ni, Co, Ti) compounds were analyzed and tested as OER electrocatalysts. After that, the effect of crystal structure on the OER activity and OER kinetics was investigated. Finally, the effect of crystallinity was examined in detail.

#### **4.3.1 Effect of Chromium in Nickel Sulfide**

Crystal structure analysis was carried out by X-ray diffraction method (XRD, Bruker D8 Advance, CuK $\alpha$ ). XRD data were collected within the  $2\theta$  range of 10-80° with 2° min<sup>-1</sup> speed. Figure 4.5(a) demonstrates the XRD spectrum of a purely crystalline NiS-mw sample. Phase analysis showed that the NiS-mw sample is a single-phase NiS compound identical to the NiAs prototype with a hexagonal ordering (space group P63/mmc, no: 194). XRD pattern of the NiS-mw, Cr/NiS and NiCr<sub>2</sub>S<sub>4</sub>-194 samples in comparison were given in Figure 4.5(b). In the presence of the Cr in the structure, crystal ordering was preserved with only slight shifts in peak positions for Cr/NiS and NiCr<sub>2</sub>S<sub>4</sub>-194 samples (Figure 4.5(b)-inset). Rietveld refinement was

carried out by Material Analysis Using Diffraction (MAUD) software [183]. Lattice parameters  $a$ ,  $c$  and  $R_w$  factor (goodness of fit) were given in Table 4.3. Lattice parameters  $a$  and  $c$  both increased as the Cr content increased in the structure. An increase in lattice parameters is logical since the ionic radius of the  $\text{Cr}^{3+}$  atom in octahedral coordination ( $0.62 \text{ \AA}$ ) is larger than that of the  $\text{Ni}^{3+}$  ( $0.65 \text{ \AA}$ ) atom [106].

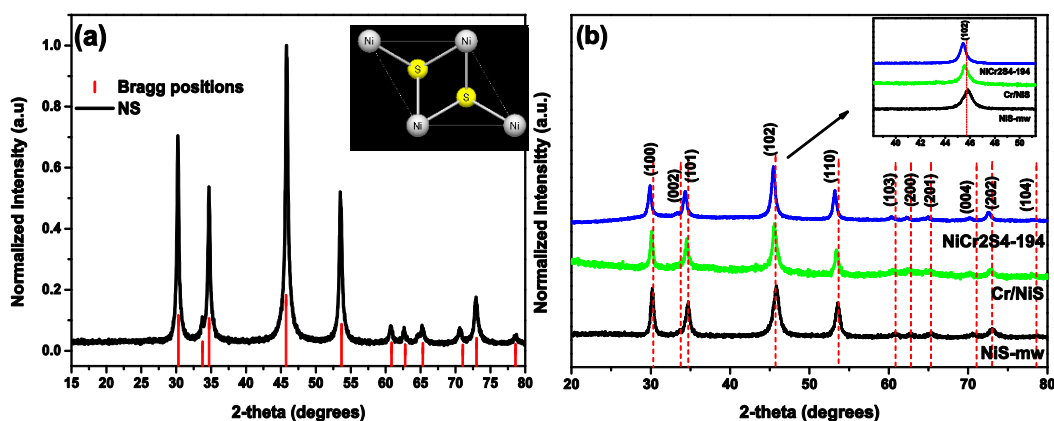


Figure 4.5. (a) XRD spectrum and phase analysis of NiS-mw sample and (b) XRD pattern of NiS-mw, Cr/NiS and NiCr<sub>2</sub>S<sub>4</sub>-194 samples in comparison.

EDS-mapping images were given in Figure 4.6 (a-c), showing that all constituent elements are well distributed throughout the structure. The differences in Cr content can also be seen in Figures 4.6 (b) and 4.6 (c) from the EDS-mapping images since Cr/NiS sample contains only 2 at. % Cr, the coloring is lighter than that of the NiCr<sub>2</sub>S<sub>4</sub>-194 sample.

Chemical compositions of each phase were demonstrated by EDS analysis (Figure 4.6(d)). NiS-mw and Cr/NiS samples contain the stoichiometric amounts of atoms in the structure. However, there is a slight difference from the stoichiometric amount (Ni:Cr: S=14:29:57 at. %) of the NiCr<sub>2</sub>S<sub>4</sub>-194 sample. NiCr<sub>2</sub>S<sub>4</sub> phase is a solid solution of CrS (space group P63/mmc, no: 194) and NiS (space group P63/mmc, no: 194) phases which can be seen in Figure 4.7. Ni and Cr atoms share the same

atomic positions in the NiCr<sub>2</sub>S<sub>4</sub> compound. In order to achieve exact stoichiometry of the NiCr<sub>2</sub>S<sub>4</sub> phase, each constituent phase (NiS and CrS) should form in a perfect stoichiometry separately. However, the S atom also has a solubility in each Ni and Cr atom, leading to the formation of non-stoichiometric NiS and CrS phases. Therefore, the deviation from exact stoichiometry is an acceptable result for the NiCr<sub>2</sub>S<sub>4</sub> compound. EDS analysis results were given in Figure 4.6 (d). NiS-mw sample contains 51 at. % Ni and 49 at. % S, which is in good agreement with the stoichiometric amount. Chemical composition of 2 at. % Cr incorporated NiS phase (Cr/NiS sample) is 46 at. % Ni, 2 at. % Cr and 52 at. % S showing the Cr substitution with Ni atom. The atom percent of Ni, Cr and S elements of the NiCr<sub>2</sub>S<sub>4</sub>-194 sample are 21 %, 33 % and 46 %, respectively.

Table 4.3 Rietveld analysis of NiS-mw, Cr/NiS and NiCr<sub>2</sub>S<sub>4</sub>-194 samples.

<b>Sample</b>	<b><i>a</i> (Å)</b>	<b><i>c</i> (Å)</b>	<b>% <i>R<sub>w</sub></i></b>
<b>NiS-standard</b>	<b>3.420</b>	<b>5.300</b>	
NiS-mw	3.428 ± 0.001	5.335 ± 0.001	2.87
Cr/NiS	3.434 ± 0.001	5.354 ± 0.001	2.68
NiCr <sub>2</sub> S <sub>4</sub> -194	3.435 ± 0.001	5.396 ± 0.002	3.19

N<sub>2</sub> adsorption/desorption isotherms were recorded by Quantachrome Corporation, Autosorb-6 analyzer. In order to remove the surface inhomogeneities, pre-heating was carried out at 200 °C for 12 h. Brunauer Emmett Teller (BET) surface area was calculated from the adsorption data. The BET surface areas of NiS-mw, Cr/NiS and NiCr<sub>2</sub>S<sub>4</sub>-194 samples are 3 m<sup>2</sup> g<sup>-1</sup>, 120 m<sup>2</sup> g<sup>-1</sup> and 170 m<sup>2</sup> g<sup>-1</sup>, respectively, which are listed in Table 4.4. As the chromium content in NiS structure increased, BET surface area also increased gradually. The large jump from 3 m<sup>2</sup> g<sup>-1</sup> to 120 m<sup>2</sup> g<sup>-1</sup> BET surface area values can be attributed to large agglomerates of the NiS-mw sample which can clearly be seen in SEM micrographs given in Figure 4.8.

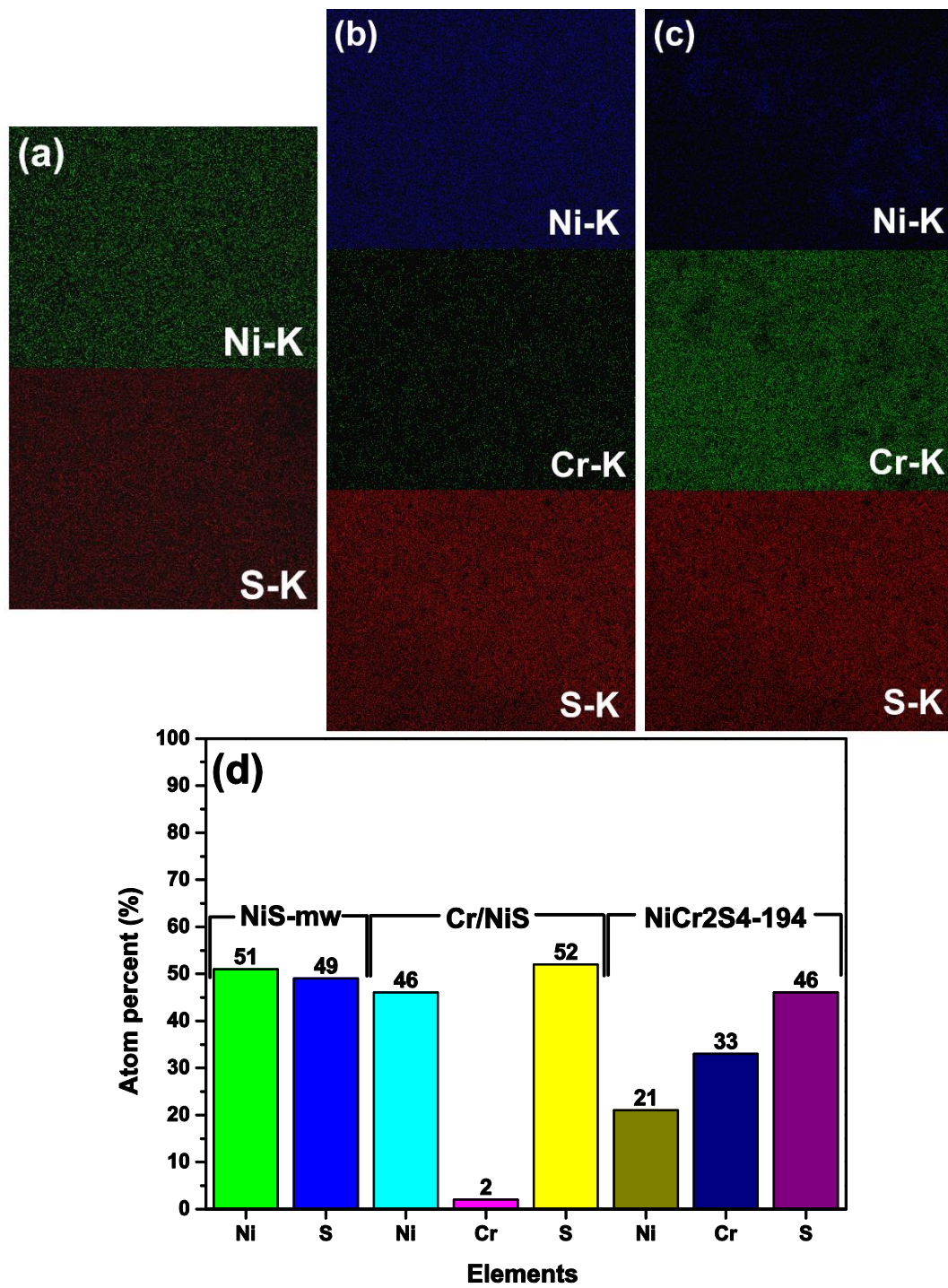


Figure 4.6. EDS-mapping images of (a) NiS-mw, (b) Cr/NiS, (c) NiCr<sub>2</sub>S<sub>4</sub>-194 samples and (d) EDS analysis results.

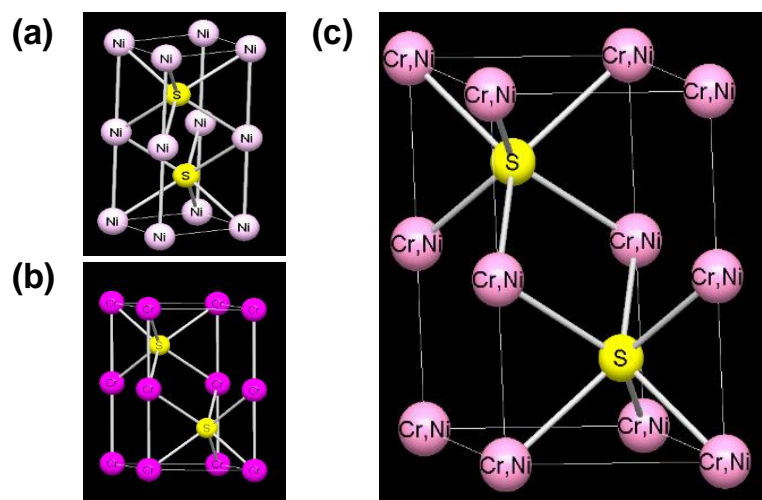


Figure 4.7. Crystal structures of (a) NiS (space group P63/mmc, no: 194), (b) CrS (space group P63/mmc, no: 194) and (c) NiCr<sub>2</sub>S<sub>4</sub> (space group P63/mmc, no: 194) compounds.

Table 4.4 Surface properties of the electrocatalysts.

Sample	BET Surface Area (m <sup>2</sup> g <sup>-1</sup> )	ECSA (cm <sup>2</sup> )	RF
NiS-mw	3	12.8	65.1
Cr/NiS	120	16.3	82.9
NiCr <sub>2</sub> S <sub>4</sub> -194	170	17.2	87.6

Electrochemically active surface area (ECSA) evaluation was carried out for a more precise examination of the surface area because some part of the BET surface area of the electrocatalyst has been lost due to sticking onto the electrode surface. Cyclic voltammograms were recorded within the potential range of 0.0-0.2 V vs. Hg/HgO/ 1 M KOH, which is the non-Faradaic potential range for the samples and CV curves were given in Figure 4.9. This data was also used to calculate the roughness factor (RF). Cyclic voltammetry data was collected at the scan rates of 50, 100, 200, 500, 1000 and 2000 mV s<sup>-1</sup>. ECSA and RF values were calculated with equations 2.18

and 2.19 as 12.8 cm<sup>2</sup> and 65.1 for NiS-mw, 16.3 cm<sup>2</sup> and 82.9 for Cr/NiS, 17.2 cm<sup>2</sup> and 87.6 for NiCr2S4-194 samples, respectively. It can be clearly seen that ECSA and RF values were increased gradually with the chromium incorporation. An increase in electrochemically active surface area and the roughness factor improves the OER activity of the electrocatalysts by making the adsorption of ions easier and facilitating the electron transfer [184]. The reason for the lack of large jump in ECSA values can be due to the breakdown of large agglomerates because of sonication of the samples for ECSA measurements.

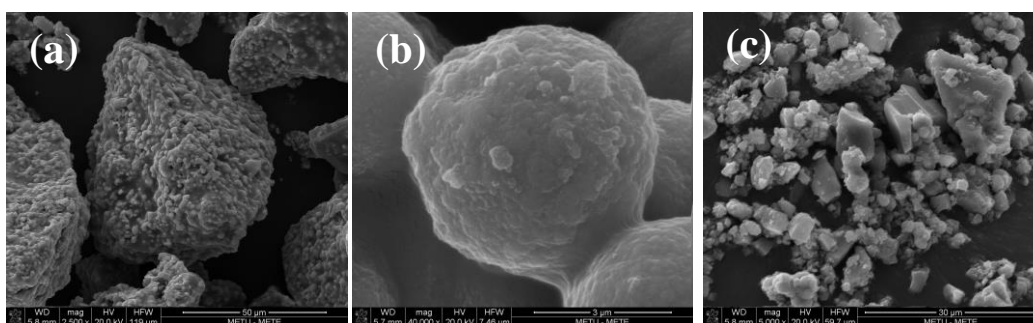


Figure 4.8. SEM micrographs of the (a) NiS-mw, (b) Cr/NiS and (c) NiCr2S4-194 samples.

X-ray photoelectron spectroscopy (XPS, PHI 5000 VersaProbe, Al K $\alpha$ , hV=1486.6 eV) was carried out to examine the valance state determination and the electronic structure. XPS spectra of the NiS-mw, Cr/NiS and NiCr2S4-194 electrocatalysts were given in Figure 4.10(a-c). Ni 2p<sub>1/2</sub> and 2p<sub>3/2</sub> peaks of the NiS-mw sample appeared at 871.8 eV and 853.9 eV. Ni 2p<sub>3/2</sub> peak doublets around 851.9 and 853.9 eV were reported as the Ni<sup>2+</sup> and Ni<sup>3+</sup> peaks in previous literature [185,186]. As Ni content decreases with chromium addition to NiS structure, Ni 2p<sub>1/2</sub> and 2p<sub>3/2</sub> peak positions shifted to the smaller binding energies. In that manner, Ni 2p<sub>1/2</sub> and 2p<sub>3/2</sub> peaks of the Cr/NiS sample appeared at 870.4 eV and 852.6 eV. Ni 2p<sub>1/2</sub> and 2p<sub>3/2</sub> peaks of the NiCr2S4-194 sample were shown up at 869.2 eV and 851.5 eV,

respectively. The area under the  $\text{Ni}^{2+}$  curve increased with chromium addition, meaning that the amount of  $\text{Ni}^{2+}$  ions in the structure has increased with chromium. The rate-determining step in oxygen evolution reactions is mostly the chemical reaction step where  $\text{Ni}^{2+}$  ions are the reactants of this chemical reaction and the following electron transfer step [176]. An increase in the amount of  $\text{Ni}^{2+}$  ions has a positive effect on OER activity and kinetics in a way that an increase in the amount of  $\text{Ni}^{2+}$  ions increases the rate of these two reactions providing faster kinetics [187].

Cr  $2p_{1/2}$  and  $2p_{3/2}$  peaks of the Cr/NiS sample were observed at 584.98 eV and 575.21 eV. As the chromium content increases, the intensity of the Cr peaks in the XPS spectrum increases, as shown in Figure 4.9 (b). Cr  $2p_{1/2}$  and  $2p_{3/2}$  peaks of the NiCr<sub>2</sub>S<sub>4</sub>-194 sample appeared around binding energies of 587.14 eV and 577.38 eV. The values of the Cr  $2p_{3/2}$  peaks of the Cr/NiS and NiCr<sub>2</sub>S<sub>4</sub>-194 samples match well with the  $\text{Cr}^{3+}$  ions, which was reported in the previous literature [188].

S 2p spectra of the NiS-mw, Cr/NiS and NiCr<sub>2</sub>S<sub>4</sub>-194 samples were shown in Figure 4.9(c). S  $2p_{1/2}$  and  $2p_{3/2}$  peaks of the samples were observed around 164.1 eV and 162.2 eV for NiS-mw. Peak positions shifted to the higher values of the binding energies as the amount of chromium in the NiS structure increased [189].

Redox peaks around 1.4 V ( $\eta = 0.17$  V) were obtained by cyclic voltammetry and curves were analyzed to determine the reversibility of these peaks. Cyclic voltammetry measurements were carried out within the potential window of 0-0.8 V vs. Hg/HgO/1 M KOH with a sweep rate of 250 mV s<sup>-1</sup> upon 100 cycles. Electrocatalysts were coated onto glassy carbon electrodes. O<sub>2</sub>-saturated 1 M KOH was used as an electrolyte. Figures 4.11(a-d) and 4.12(a-c) represent the cyclic voltammograms of the NiS-mw, Cr/NiS and NiCr<sub>2</sub>S<sub>4</sub>-194 samples after the 1<sup>st</sup>, 2<sup>nd</sup>, 50<sup>th</sup> and 100<sup>th</sup> cycles. The quasi-reversible redox peaks between 1.3-1.5 V were the signs of the formation of the  $\text{Ni}^{2+}/\text{Ni}^{3+}$  redox couple due to the oxidation of Ni ions [190].

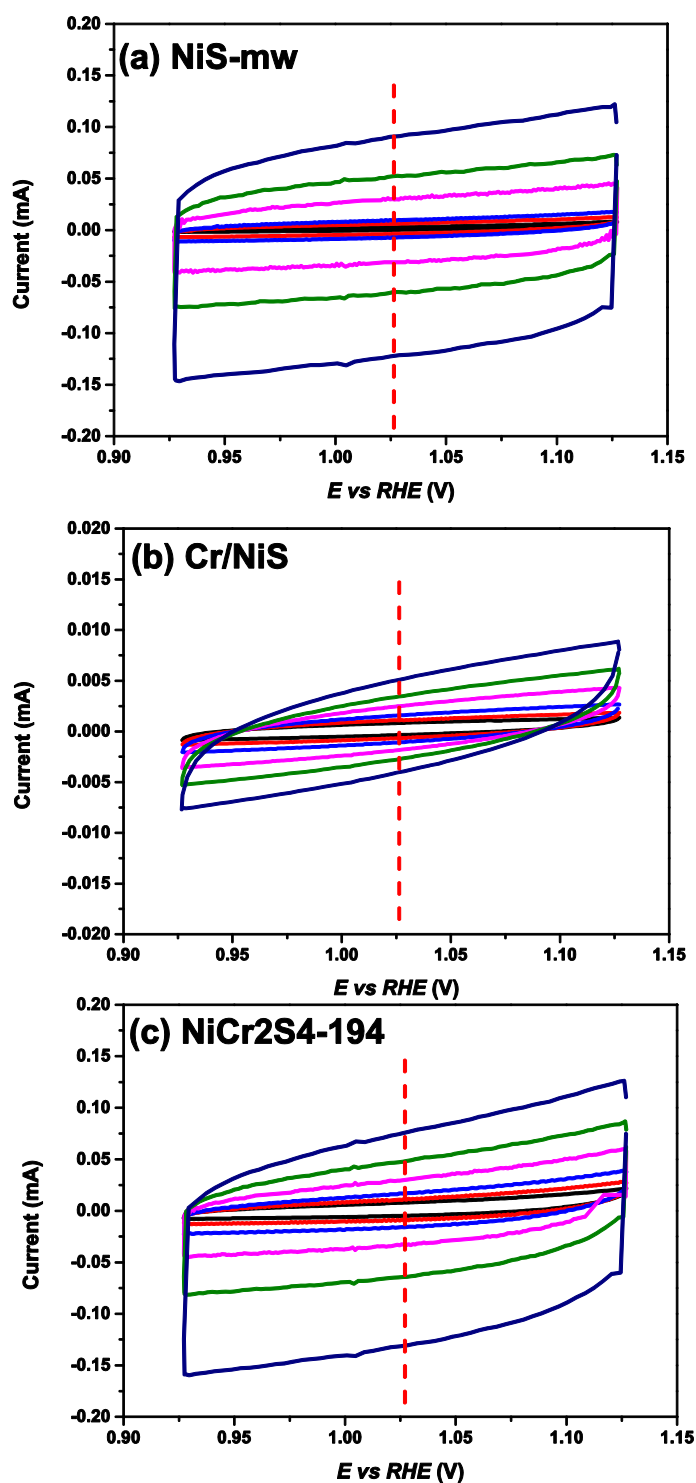


Figure 4.9. Cyclic voltammetry curves of (a) NiS-mw, (b) Cr/NiS and (c) NiCr<sub>2</sub>S<sub>4</sub>-194 electrocatalysts in the non-Faradaic region.

The intensity of the redox peaks was similar for the chromium incorporated Cr/NiS and NiCr<sub>2</sub>S<sub>4</sub>-194 samples and larger than that of the bare NiS-mw sample. OER potentials of the Cr incorporated samples also shifted to the lower potentials, which is a significant contribution of Cr in the NiS structure. The reason for the enhanced OER activity can be the modification of the electronic structure by chromium addition. Stability is reached up to 50 cycles for each of the samples since there is no difference between 50<sup>th</sup> and 100<sup>th</sup> cycles in terms of peak currents and potentials.

Electrochemical impedance spectroscopy (EIS) data were collected within the frequency range of 100 kHz – 100 Hz at the open-circuit voltage (OCV) with a voltage amplitude of  $\pm 10$  mV in order to eliminate the Ohmic potential (*iR*) drops due to the solution resistance. *iR*-correction was carried out by equation 2.22, where solution resistance was obtained from the EIS data as 5.1  $\Omega$ . *iR*-corrected potential values vs. Hg/HgO/1 M KOH received from linear sweep voltammetry (LSV) measurements were converted to potential values vs. reversible hydrogen electrode (RHE) with equation 2.23 and OER overpotentials were calculated with equation 2.24.

OER activity of the catalysts was investigated by linear sweep voltammetry (LSV) measurements within the potential window of 0-0.8 V vs. Hg/HgO/1 M KOH with a scan rate of 5 mV s<sup>-1</sup>. Electrocatalysts were coated onto glassy carbon electrode and bare glassy carbon was tested under the same conditions as the electrocatalyst samples to estimate the background current. O<sub>2</sub>-saturated 1 M KOH was used as electrolyte and measurements were carried out with a rotating disc electrode system at 1600 rpm with a continuous O<sub>2</sub> flow through the electrolyte.

The differences in the uncorrected and *iR*-corrected LSV curves are demonstrated in Figure 4.13. Solid lines represent uncorrected values and dashed lines show the *iR*-corrected potential values of a bare glassy carbon electrode and electrocatalyst samples. It can be clearly seen that *iR*-correction has a remarkable effect on the OER potential of the electrocatalysts. The OER potential of the NiCr<sub>2</sub>S<sub>4</sub>-194 sample was shifted from 1.573 V to 1.564 V, which counts a  $\sim 10$  mV decrease in OER potential

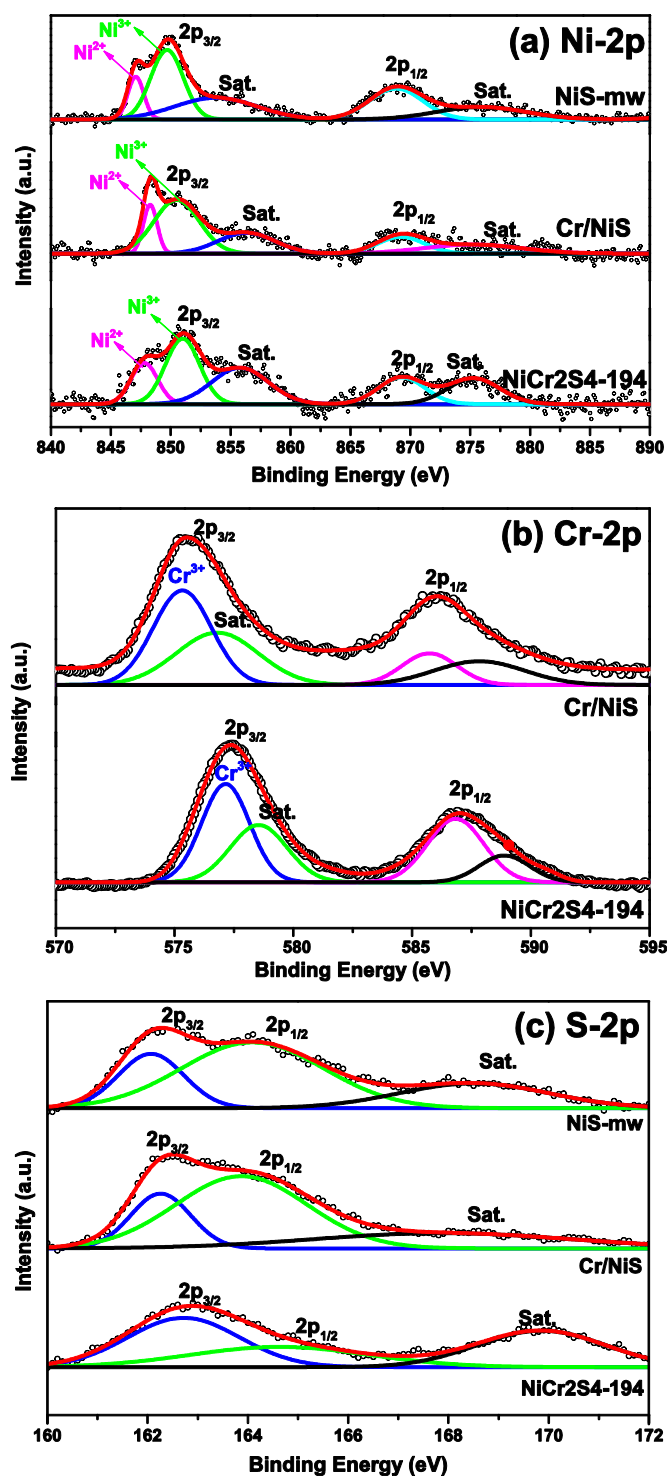


Figure 4.10. (a) Ni-2p, (b) Cr-2p and (c) S-2p XPS spectra of the NiS-mw, Cr/NiS and NiCr<sub>2</sub>S<sub>4</sub>-194 electrocatalysts.

for all samples since solution resistance ( $R_s$ ) was taken as the same ( $5.1 \Omega$ ) for all samples.  $R_s$  values were measured with the EIS technique for each sample separately and the average value ( $5.1 \Omega$ ) was used as solution resistance.

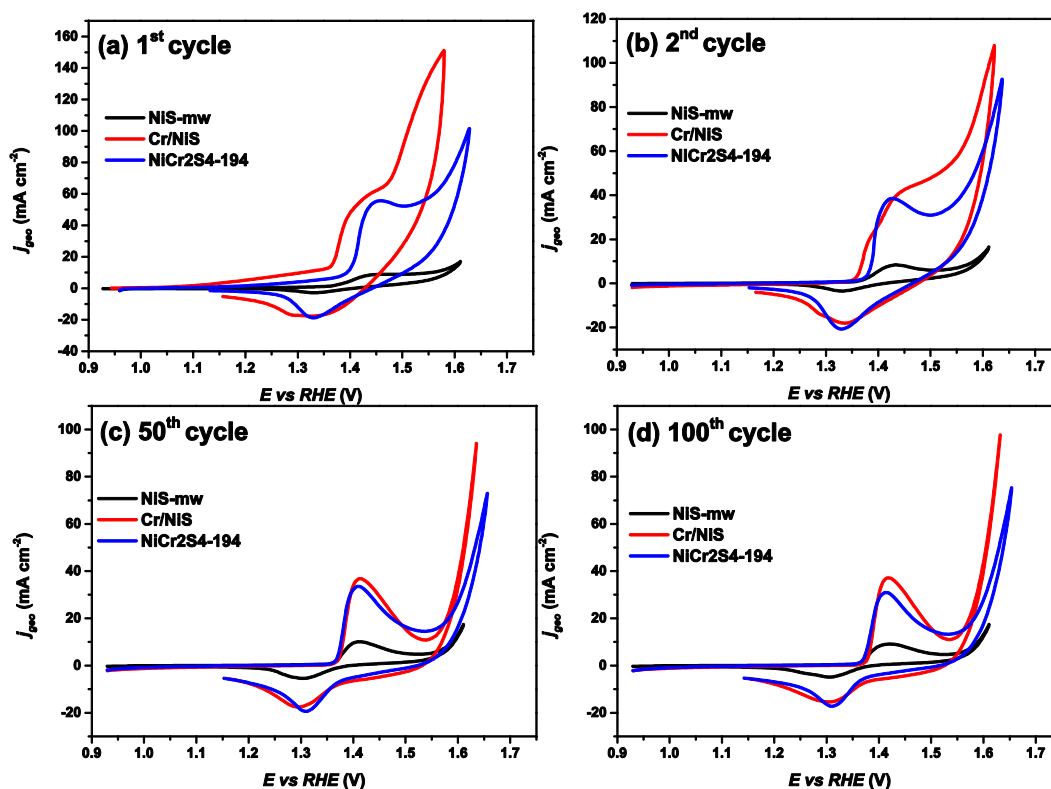


Figure 4.11. Cyclic voltammograms at the (a) 1<sup>st</sup>, (b) 2<sup>nd</sup>, (c) 50<sup>th</sup> and (d) 100<sup>th</sup> cycles of the NiS-mw, Cr/NiS and NiCr2S4-194 samples.

Catalyst performance test graphs were given in Figure 4.14(a-e). NiS-mw, Cr/NiS and NiCr2S4-194 samples exhibited 372 mV, 334 mV and 354 mV OER overpotentials, respectively (Figure 4.14(a)). Tahir et al. [191] categorized the OER catalysts with respect to overpotential values at  $10 \text{ mA cm}^{-2}$  as satisfactory (more than 500 mV), good (400-500 mV), excellent (300-400 mV) and ideal (200-300 mV)

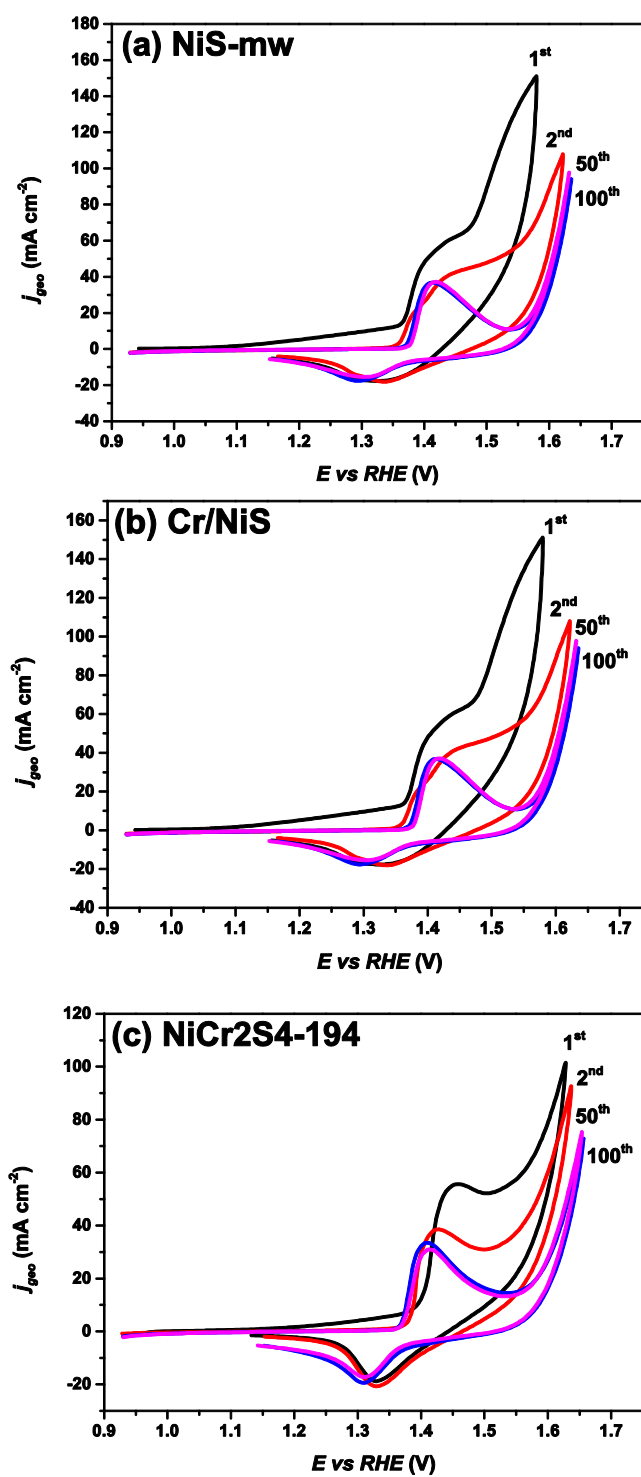


Figure 4.12. Cyclic voltammety curves of the (a) NiS-mw, (b) Cr/NiS and (c) NiCr<sub>2</sub>S<sub>4</sub>-194 electrocatalysts at 1<sup>st</sup>, 2<sup>nd</sup>, 50<sup>th</sup> and 100<sup>th</sup> cycles.

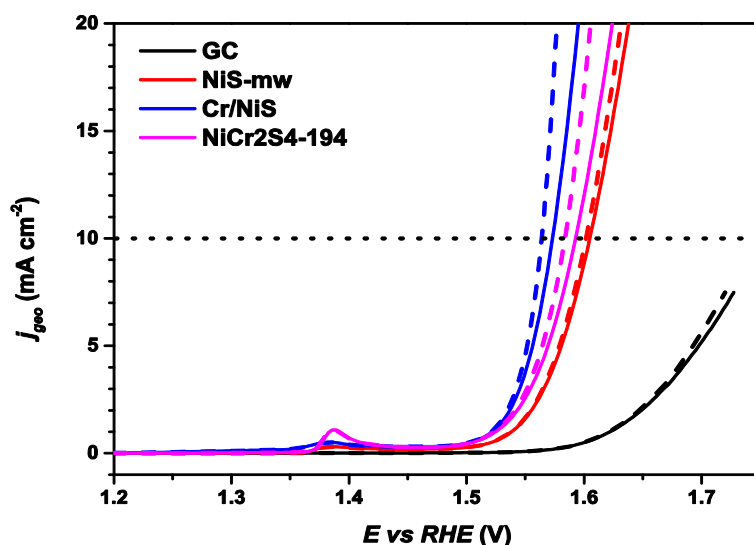


Figure 4.13. Comparison of the uncorrected (solid) and iR-corrected (dashed) LSV curves of NiS-mw, Cr/NiS and NiCr<sub>2</sub>S<sub>4</sub>-194 samples and bare glassy carbon electrode (GC).

According to this classification, all three samples showed excellent OER activity. Chromium incorporation has a significant contribution to the OER activities. All three samples exhibited better OER activity than the benchmark RuO<sub>2</sub> with an overpotential value of 387 mV at 10 mA cm<sup>-2</sup> current density [192]. The presence of Cr atoms in NiS structure may create extra active sites for electrocatalysis as well as causes the reconstruction of electronic structure, which may result in the change in the charge and mass transport mechanisms [193]. These effects are clearly seen in not only the OER performance and kinetics but also in stability tests of Cr incorporated NiS samples (Figure 4.14(b)). Chronopotentiometry measurements at 10 mA cm<sup>-2</sup> were carried out to test the durability of the samples for 20 hours. NiS-mw sample showed poor catalyst stability since it can maintain its performance only for 9 hours due to chemical degradation. However, Cr incorporated samples exhibited excellent OER stability within 20 hours.

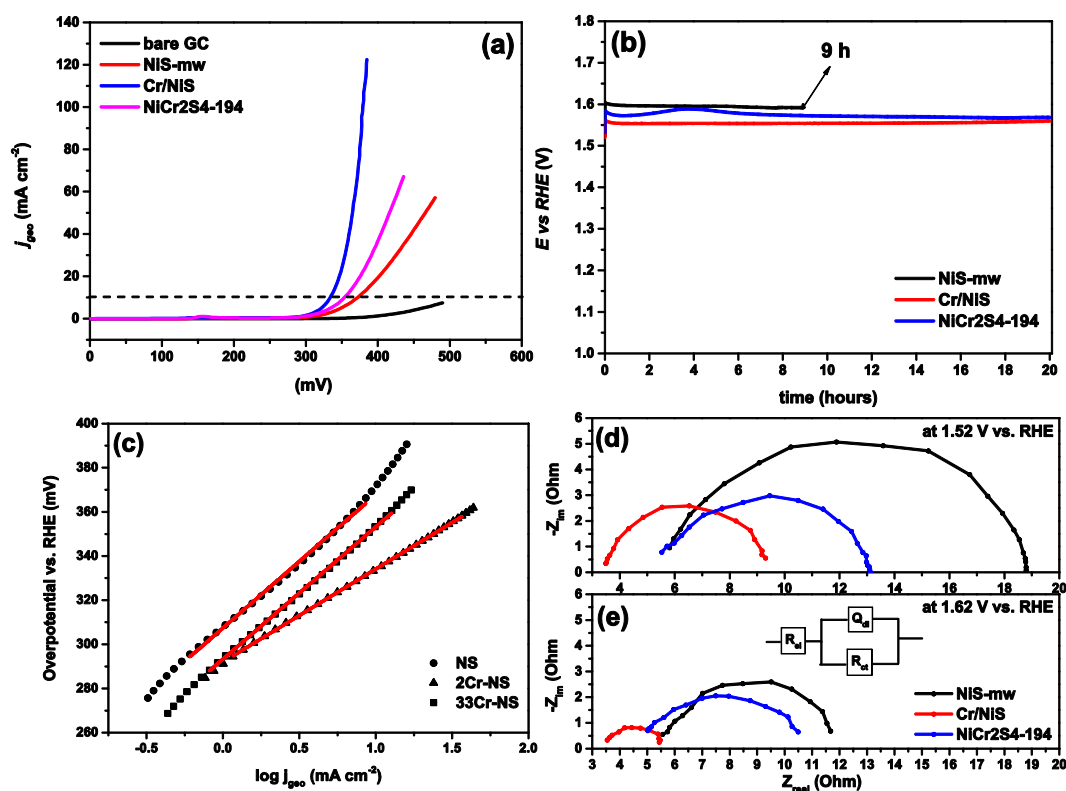
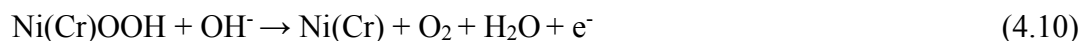


Figure 4.14. (a) LSV curves, (b) CP curves, (c) Tafel slopes and EIS plots at (d) 1.52 V and (e) 1.62 V of the electrocatalysts.

Figure 4.14(c) shows the Tafel slopes. Zhou et al. [194] investigated the  $\text{Ni}_3\text{S}_2$  onto Ni foam for OER electrocatalyst and achieved a  $159 \text{ mV dec}^{-1}$  Tafel slope for this sample. NiS-mw, Cr/NiS and NiCr2S4-194 samples yielded 60, 42, 59  $\text{mV dec}^{-1}$  Tafel slopes, respectively, which shows much better kinetics than the  $\text{Ni}_3\text{S}_2$  in Zhou's study. These values are also smaller than the Tafel slope of the benchmark  $\text{RuO}_2$  ( $90 \text{ mV dec}^{-1}$ ), indicating a superior kinetic behavior for all three samples. Since all the slopes are lower than  $120 \text{ mV dec}^{-1}$ , multi-electron transfer reaction is the mechanism for all samples, which were proposed in equations 4.6-4.9. It was concluded that the rate-determining step is the chemical reaction step for NiS-mw and NiCr2S4-194 samples since their Tafel slopes are almost the same. However,

the rate-determining step for the Cr/NiS sample is the third electron transfer reaction indicating enhanced kinetics due to modified electronic structure (more extensive amount of Ni<sup>2+</sup> ions) [176]. Cr/NiS sample showed the best OER performance and kinetics among the three samples.



Intrinsic OER activities of all samples were given in Table 4.5 in comparison. Mass activities of the electrocatalysts were calculated with equation 2.20 and exhibited as 8.4 A g<sup>-1</sup>, 60.5 A g<sup>-1</sup> and 15.1 A g<sup>-1</sup> for NiS-mw, Cr/NiS and NiCr2S4-194 samples, respectively. Cr/NiS sample has the largest mass activity (~2 times higher than the benchmark RuO<sub>2</sub> catalyst), which is an outperforming value of all samples. Intrinsic OER activities were further analyzed by turnover frequency (TOF) calculations which were carried out with equation 2.21. NiS-mw, Cr/NiS and NiCr2S4-194 samples yielded 0.00194 s<sup>-1</sup>, 0.01423 s<sup>-1</sup> and 0.00284 s<sup>-1</sup> TOF values, respectively. The highest TOF value was achieved by the Cr/NiS sample, which supports the Tafel behavior (smallest Tafel slope value) of this sample, meaning that the number of active catalytic sites is the largest for Cr/NiS among the other samples. The possible reasons for the increase in the number of active catalytic sites with Cr addition can be an increase in the BET surface area, larger ECSA and RF values compared to the NiS-mw sample and the modification of the electronic structure (increase in the Ni<sup>2+</sup> ions content).

Table 4.5 Intrinsic OER activities and Tafel slopes of the NiS-mw, Cr/NiS and NiCr2S4-194 samples.

Sample	mass activity			
	$\eta$ (mV) at $j=10 \text{ mA cm}^{-2}$	( $\text{A g}^{-1}$ ) at $\eta=375 \text{ mV}$	TOF ( $\text{s}^{-1}$ ) at $\eta=375 \text{ mV}$	Tafel Slope ( $\text{mV dec}^{-1}$ )
NiS-mw	372	8.4	0.00194	60
Cr/NiS	334	60.5	0.01423	42
NiCr2S4-194	354	15.1	0.00284	59

Electrochemical impedance spectroscopy (EIS) data were collected at two different potential values in order to investigate the differences in the kinetic of the samples. In this manner, EIS measurements were carried out at 1.52 V (the onset potential) and at 1.62 V, where a high OER activity can be seen for all samples. Nyquist plots obtained from EIS were given in Figures 4.14(d) and (e). These plots were fitted to an equivalent circuit model (Randles model), shown in Figure 4.14 (e) inset, which consists of a constant phase element ( $Q_{dl}$ ) used for calculations of the double-layer capacitance and a charge transfer resistance ( $R_{ct}$ ) connected in parallel to the  $Q_{dl}$ . The model also contains electrolyte resistance ( $R_s$ ) connected in series to both the  $R_{ct}$  and  $Q_{dl}$ . The reason for using constant phase element ( $Q_{dl}$ ) instead of pure capacitor element ( $C_{dl}$ ) is that electrodes mostly deviate from the ideal capacitor behavior due to surface roughness, surface inhomogeneities, porosity, *etc.* related potential distributions [195]. Resistance values of the NiS-mw, Cr/NiS and NiCr2S4-194 samples were given in Table 4.6. NiS-mw, Cr/NiS and NiCr2S4-194 samples yielded 13.5  $\Omega$ , 6.1  $\Omega$  and 7.8  $\Omega$  charge transfer resistances, respectively, at the onset potential (at 1.52 V).  $R_{ct}$  values exhibited as 6.5  $\Omega$ , 2.1  $\Omega$  and 5.5  $\Omega$  for NiS-mw, Cr/NiS and NiCr2S4-194 samples, respectively, at 1.62 V. Decrease in the charge transfer resistance was an expected result indicating a higher charge transport efficiency at this potential. Moreover, all charge transfer resistance values are correlated to the Tafel slopes, which can be attributed to the enhanced kinetic

behavior with Cr incorporation into the NiS structure due to better conductivity [196].

Table 4.6 Resistance values of the NiS-mw, Cr/NiS and NiCr2S4-194 samples.

<b>Samples</b>	<b>R<sub>ct</sub> at 1.52 V (Ω)</b>	<b>R<sub>ct</sub> at 1.62 (Ω)</b>
NiS-mw	13.5	6.5
Cr/NiS	6.1	2.1
NiCr2S4-194	7.8	5.5

#### 4.3.2 Effect of A-site Element in ACr<sub>2</sub>S<sub>4</sub> (A = Ni, Co, Ti) Structure

XRD pattern of ACr<sub>2</sub>S<sub>4</sub> (where A= Ni, Co, Ti) samples which are NiCr<sub>2</sub>S<sub>4</sub>-12, CoCr<sub>2</sub>S<sub>4</sub> and TiCr<sub>2</sub>S<sub>4</sub>, were given in Figure 4.15. Vertical red dashed lines represent the Bragg positions of the Cr<sub>3</sub>S<sub>4</sub> phase. All three phases match well with the Cr<sub>3</sub>S<sub>4</sub> prototype with a space group of C12/m1, no: 12. In this study, one Cr atom in the Cr<sub>3</sub>S<sub>4</sub> prototype was substituted by Ni, Co or Ti atoms separately, which can be visualized by crystal structure images of the NiCr<sub>2</sub>S<sub>4</sub>, CoCr<sub>2</sub>S<sub>4</sub> and TiCr<sub>2</sub>S<sub>4</sub> compounds with space group C12/m1, no: 12 given in Figures 4.16(a-c).

Lattice parameters obtained from Rietveld Analysis and ionic radius with six-fold octahedral coordination of Ti, Cr, Co and Ni atoms were given in Table 4.7 [106]. The ionic radius of Co and Ni atoms is smaller than Cr, while the Ti atom is larger than Cr. Increase/decrease in lattice parameters *a*, *b* and *c* coincide with the ionic radius of atoms being larger or smaller than the Cr atom for all samples. In other words, all lattice parameters were increased by substituting the Ti atom with Cr since the ionic radius of Ti is larger than that of the Cr atom. However, lattice parameters *a*, *b* and *c* were all decreased by substituting Ni or Co atoms with Cr atoms. Changes

in lattice parameters also caused shifts in peak positions in the XRD spectrums (Figure 4.15 inset).

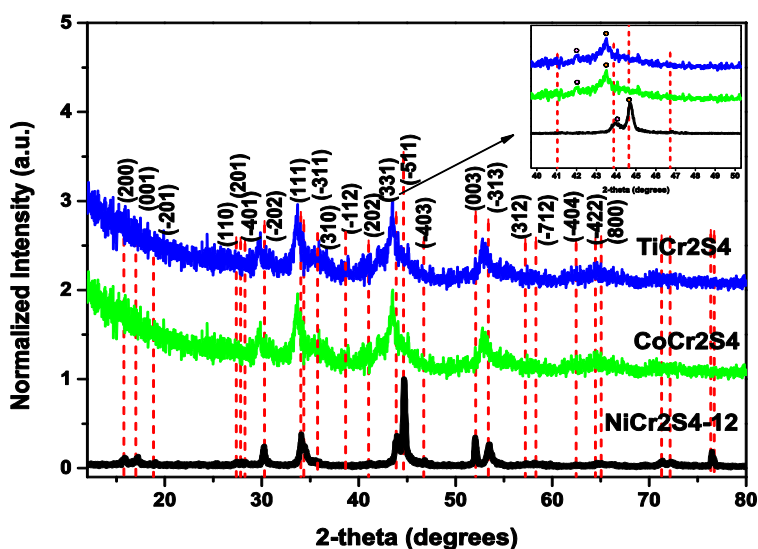


Figure 4.15. XRD pattern of NiCr<sub>2</sub>S<sub>4</sub>-12, CoCr<sub>2</sub>S<sub>4</sub> and TiCr<sub>2</sub>S<sub>4</sub> samples.

EDS-mapping images given in Figures 4.17(a-c) show that all constituent elements are well distributed throughout the structure. NiCr<sub>2</sub>S<sub>4</sub>-12 and TiCr<sub>2</sub>S<sub>4</sub> samples contain the stoichiometric amounts of atoms in the structure. However, there is a slight difference from the stoichiometric amount of the CoCr<sub>2</sub>S<sub>4</sub> sample. Despite the deviation from the stoichiometry, phase change was not observed in the CoCr<sub>2</sub>S<sub>4</sub> sample (Figure 4.15). Chemical compositions of each phase obtained from the EDS analysis were demonstrated in Figure 4.17(d)). The NiCr<sub>2</sub>S<sub>4</sub>-12 sample contains 17 at. % Ni, 37 at. % Cr and 46 at. % S, which is in good agreement with the stoichiometric amount. Similarly, 18 at. % Ti, 35 at. % Cr and 47 at. % S content of the TiCr<sub>2</sub>S<sub>4</sub> sample is very close to the stoichiometric composition with minor deviations. However, the chemical composition of the CoCr<sub>2</sub>S<sub>4</sub> sample (15 at. % Co, 19 at. % Cr and 66 at. % S) clearly deviate from the stoichiometry. The reason

is that Ni, Co and Ti atoms have a solubility in the NiCr<sub>2</sub>S<sub>4</sub>, CoCr<sub>2</sub>S<sub>4</sub> and TiCr<sub>2</sub>S<sub>4</sub> compounds, respectively, making the non-stoichiometric compositions acceptable.

Table 4.7 Rietveld analysis of NiCr<sub>2</sub>S<sub>4</sub>-12, CoCr<sub>2</sub>S<sub>4</sub> and TiCr<sub>2</sub>S<sub>4</sub> samples and ionic radius with six-fold octahedral coordination of Ti, Cr, Co and Ni atoms [106], respectively.

Samples	<i>a</i> (Å)	<i>b</i> (Å)	<i>c</i> (Å)	% <i>R<sub>w</sub></i>	Ionic radius (Å)
TiCr <sub>2</sub> S <sub>4</sub>	12.831±0.0015	3.455±0.0019	6.053±0.0013	4.18	Ti <sup>2+</sup> :0.86, Ti <sup>3+</sup> :0.67
<b>Cr<sub>3</sub>S<sub>4</sub>-standard</b>	<b>12.720</b>	<b>3.420</b>	<b>6.000</b>		Cr <sup>2+</sup> :0.80, Cr <sup>3+</sup> :0.62
CoCr <sub>2</sub> S <sub>4</sub>	12.684±0.0007	3.416±0.0011	5.979±0.0009	3.27	Co <sup>2+</sup> :0.75, Co <sup>3+</sup> :0.61
NiCr <sub>2</sub> S <sub>4</sub> -12	12.673±0.0031	3.414±0.0023	5.917±0.0016	3.84	Ni <sup>2+</sup> :0.69, Ni <sup>3+</sup> :0.60

Cyclic voltammetry measurements were carried out within the potential window of 0-0.9 V vs. Hg/HgO/1 M KOH with a sweep rate of 250 mV s<sup>-1</sup> upon 100 cycles. Electrocatalysts were coated onto glassy carbon electrodes. O<sub>2</sub>-saturated 1 M KOH was used as an electrolyte. Figures 4.18(a-d) and 4.19(a-c) represent the cyclic voltammograms of the NiCr<sub>2</sub>S<sub>4</sub>-12, CoCr<sub>2</sub>S<sub>4</sub> and TiCr<sub>2</sub>S<sub>4</sub> samples after the 1<sup>st</sup>, 2<sup>nd</sup>, 50<sup>th</sup> and 100<sup>th</sup> cycles. Stability is reached up to 50 cycles for each of the samples since there is no difference between the CV curves at the 50<sup>th</sup> and 100<sup>th</sup> cycles. CoCr<sub>2</sub>S<sub>4</sub> sample reached the highest current density within the experimental potential range, which may be a sign of faster kinetics and better performance. TiCr<sub>2</sub>S<sub>4</sub> sample did not exhibit any redox peaks upon 100 cycles. Similarly, the NiCr<sub>2</sub>S<sub>4</sub>-12 sample did not exhibit any obvious redox peaks at the 1<sup>st</sup> and 2<sup>nd</sup> cycles. However, quasi-reversible redox peaks were observed upon cycling between 1.3-1.5 V. This behavior resembles the NiCr<sub>2</sub>S<sub>4</sub>-194 sample under the same testing conditions, which was already discussed in detail in section 4.3.1. Therefore, these peaks were attributed to the formation of the Ni<sup>2+</sup>/Ni<sup>3+</sup> redox couple due to the oxidation of Ni ions [190]. Oxidation peak at 1.1 V and reduction peak at 1.0 V were observed in the CV plot of the CoCr<sub>2</sub>S<sub>4</sub> sample. These peaks became sharper upon

cycling due to the OER potentials of all samples shifting to the higher potentials, which can be due to the decrease in the number of active species upon cycling. Redox peaks of the CoCr<sub>2</sub>S<sub>4</sub> sample between 1.0-1.1 V were attributed to the Co<sup>2+</sup>/Co<sup>3+</sup> redox couple, which was reported in the previous literature [26].

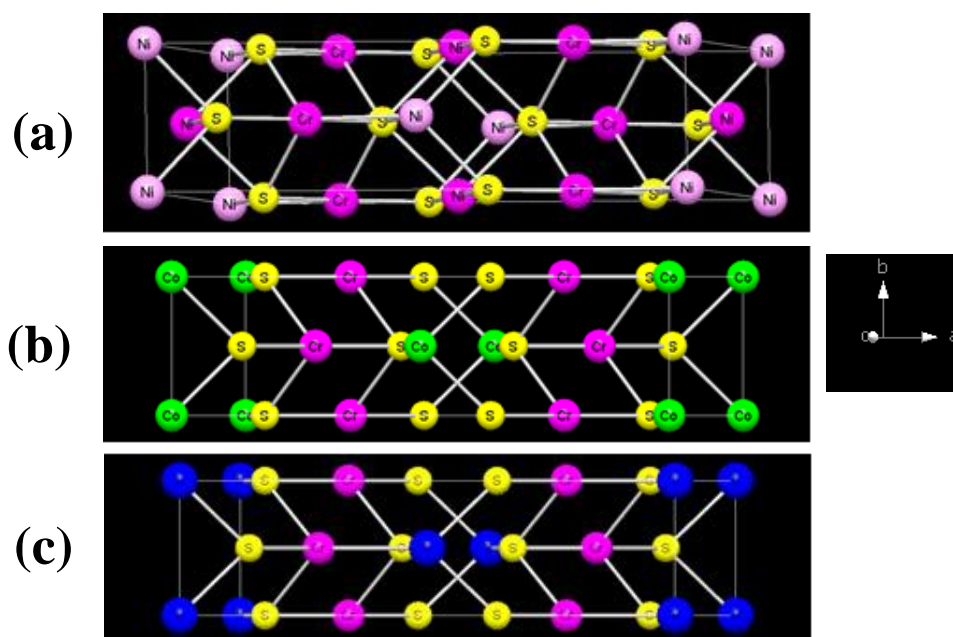


Figure 4.16. Crystal structures of (a) NiCr<sub>2</sub>S<sub>4</sub> (space group C12/m1, no: 12), (b) CoCr<sub>2</sub>S<sub>4</sub> (space group C12/m1, no: 12) and (c) TiCr<sub>2</sub>S<sub>4</sub> (space group C12/m1, no: 12) compounds.

Cyclic voltammograms were recorded within the potential range of 0.0-0.2 V vs. Hg/HgO/1 M KOH, which is the non-Faradaic potential range for the samples and CV curves were given in Figure 4.20. This data was also used to calculate the roughness factor (RF). Cyclic voltammetry data was collected at the scan rates of 50, 100, 200, 500, 1000, and 2000 mV s<sup>-1</sup>. ECSA and RF values were calculated with

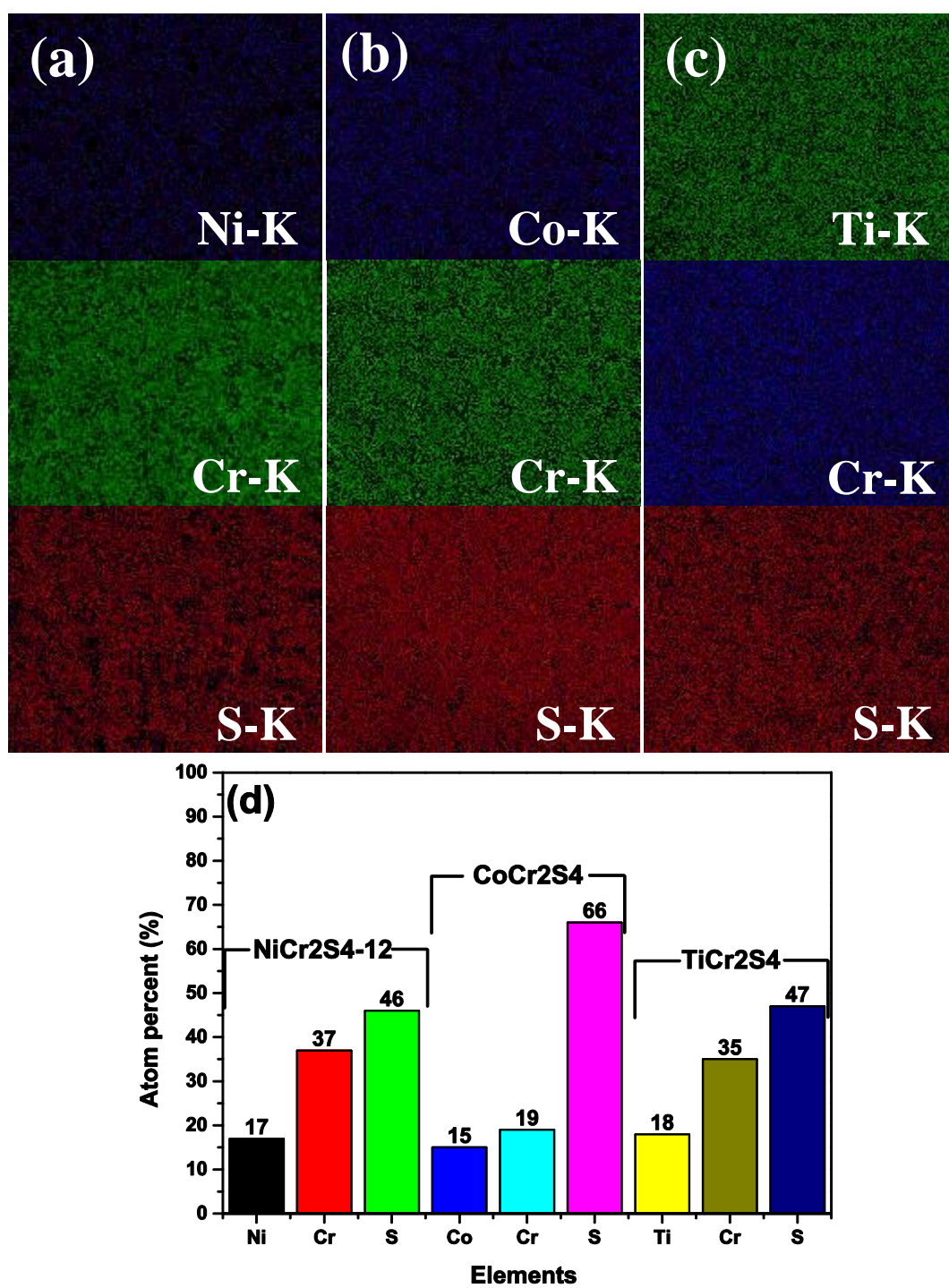


Figure 4.17. EDS-mapping images of (a) NiCr<sub>2</sub>S<sub>4</sub>-12, (b) CoCr<sub>2</sub>S<sub>4</sub>, (c) TiCr<sub>2</sub>S<sub>4</sub> samples and (d) EDS analysis results.

equations 2.18 and 2.19 as  $35 \text{ cm}^2$  and  $178.6$  for NiCr2S4-12,  $75 \text{ cm}^2$  and  $382.7$  for CoCr2S4,  $25 \text{ cm}^2$  and  $127.6$  for TiCr2S4 samples, respectively and given in Table 4.8. It can be clearly seen that the CoCr2S4 sample exhibited the largest ECSA and RF values. Therefore, the best OER activity was expected from the CoCr2S4 sample, then NiCr2S4-12. The poorest performance (but close to the NiCr2S4-12 sample) was expected from the TiCr2S4 due to ECSA and RF values.

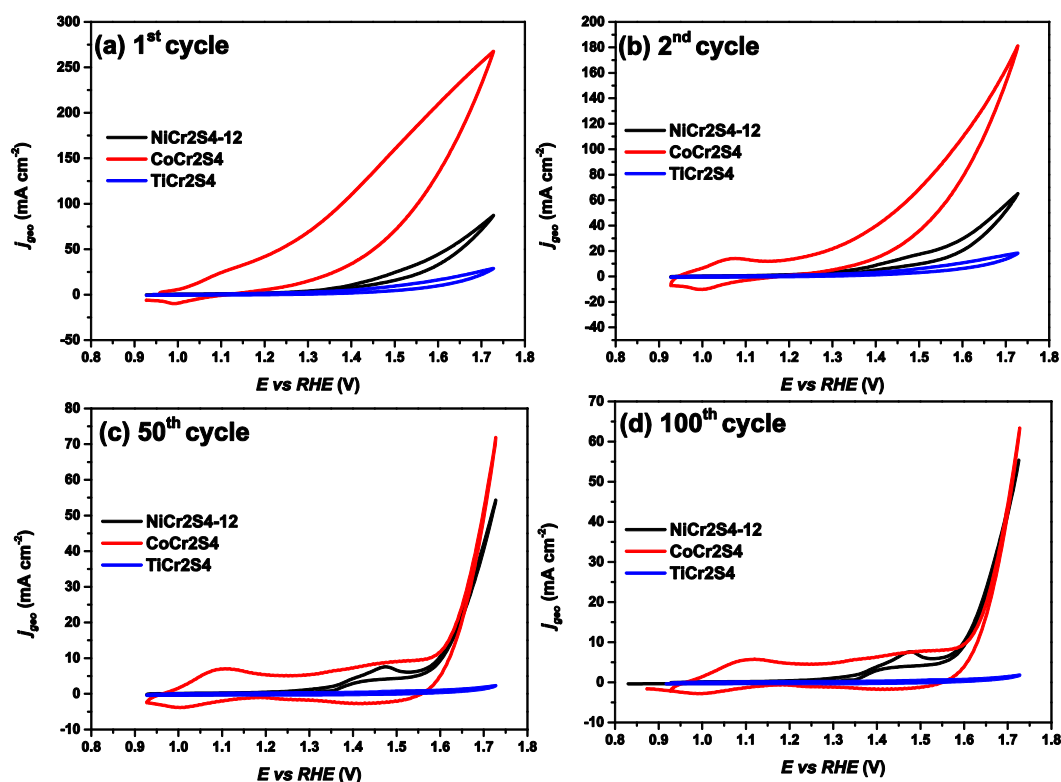


Figure 4.18. Cyclic voltammograms at the (a) 1<sup>st</sup>, (b) 2<sup>nd</sup>, (c) 50<sup>th</sup> and (d) 100<sup>th</sup> cycles of the NiCr2S4-12, CoCr2S4 and TiCr2S4 samples.

Catalyst performance test graphs were given in Figure 4.21(a-e). NiCr<sub>2</sub>S<sub>4</sub>-12, CoCr<sub>2</sub>S<sub>4</sub> and TiCr<sub>2</sub>S<sub>4</sub> samples exhibited 356 mV, 338 mV and 363 mV OER overpotentials, respectively (Figure 4.21(a)). According to Tahir's [191] classification, all three samples showed excellent OER activity. All three samples exhibited better OER activity than the benchmark RuO<sub>2</sub> with an overpotential value of 387 mV at 10 mA cm<sup>-2</sup> current density [192]. Chronopotentiometry measurements at 10 mA cm<sup>-2</sup> were carried out to test the durability of the samples for 20 hours. In addition to OER activity, all samples showed good stability upon 20 h, as shown in Figure 4.21(b).

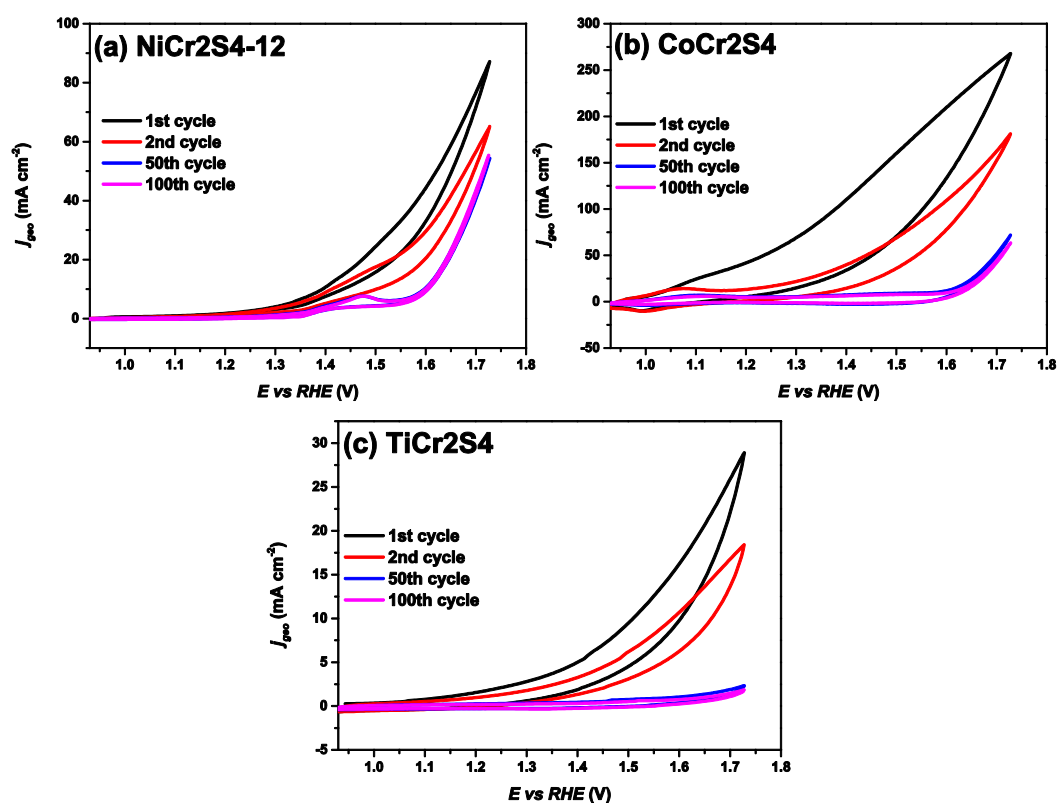


Figure 4.19. Cyclic voltammetry curves of the (a) NiCr<sub>2</sub>S<sub>4</sub>-12, (b) CoCr<sub>2</sub>S<sub>4</sub> and (c) TiCr<sub>2</sub>S<sub>4</sub> electrocatalysts at 1<sup>st</sup>, 2<sup>nd</sup>, 50<sup>th</sup> and 100<sup>th</sup> cycles.

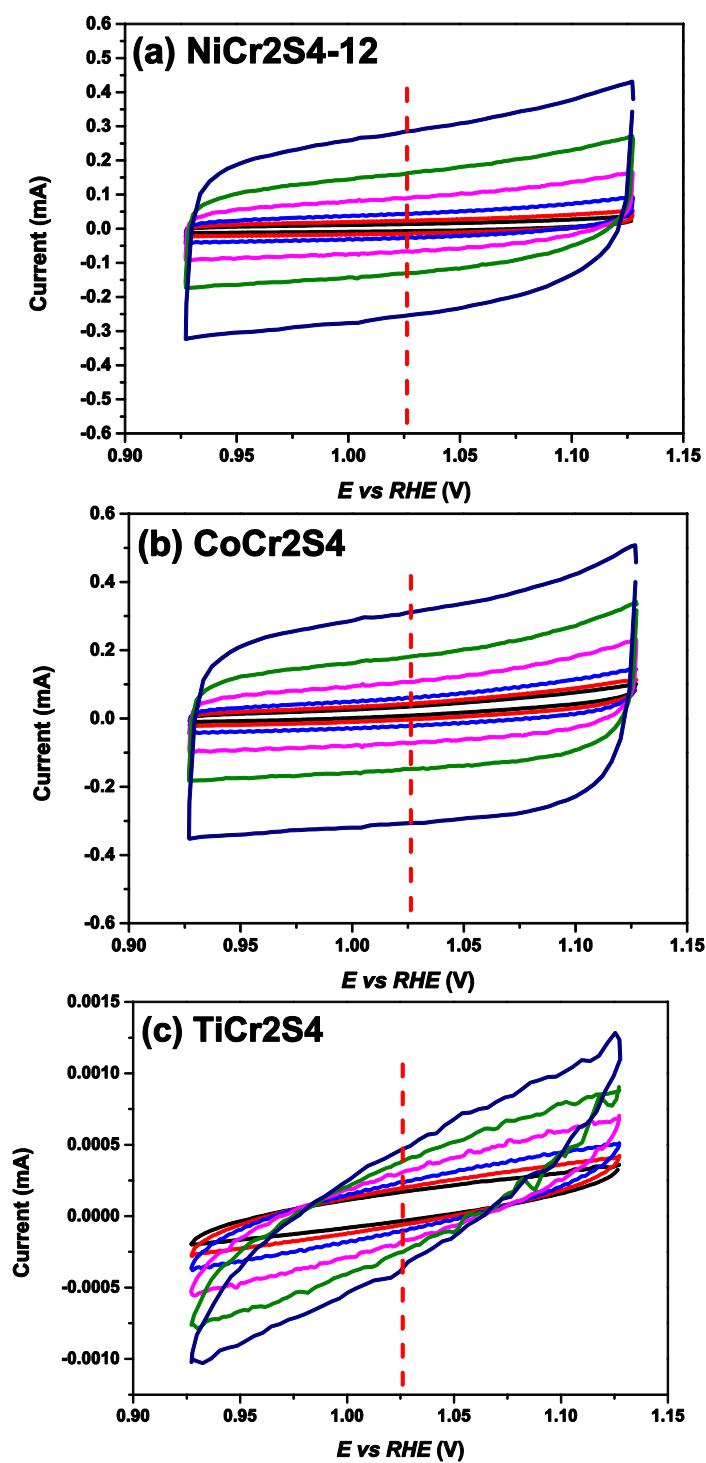


Figure 4.20. Cyclic voltammety curves of (a) NiCr<sub>2</sub>S<sub>4</sub>-12, (b) CoCr<sub>2</sub>S<sub>4</sub> and (c) TiCr<sub>2</sub>S<sub>4</sub> electrocatalysts in the non-Faradaic region.

Table 4.8 Electrochemical surface area (ECSA) and roughness factor (RF) values of the NiCr2S4-12, CoCr2S4 and TiCr2S4 samples.

<b>Sample</b>	<b>ECSA (cm<sup>2</sup>)</b>	<b>RF</b>
NiCr2S4-12	35.1	178.6
CoCr2S4	75.3	382.7
TiCr2S4	25.2	127.6

Figure 4.21(c) shows the Tafel slopes. NiCr2S4-12, CoCr2S4 and TiCr2S4 samples yielded 117, 82, 42 mV dec<sup>-1</sup> Tafel slopes, respectively. Tafel slopes of the CoCr2S4 and TiCr2S4 samples are smaller than the Tafel slope of the benchmark RuO<sub>2</sub> (90 mV dec<sup>-1</sup>), indicating a superior kinetic behavior. However, NiCr2S4-12 exhibited the largest Tafel slope among the three samples. Since all the slopes are lower than 120 mV dec<sup>-1</sup>, multi-electron transfer reaction is the mechanism for all samples, which were proposed in equations 4.6-4.9. It was concluded that the rate-determining step is the first electron transfer reaction for NiCr2S4-12, chemical reaction after one electron transfer for the CoCr2S4 and the third electron transfer reaction for the TiCr2S4 samples. Although the TiCr2S4 sample showed a superior kinetic behavior to the other two samples, it exhibited the lowest OER activity. TiCr2S4 sample has the largest lattice parameters, which makes this sample a more open structure as compared to NiCr2S4-12 and CoCr2S4. This crystal structure may contribute to the kinetics of this sample; however, the OER activity is affected by the number of active sites, surface morphology and the electronic structure. ECSA and RF values showed that these properties dominated the OER performance rather than the crystal structure. Electrical conductivity can be another factor that may affect the OER performances of the samples. Electrical conductivities of the NiCr2S4-12, CoCr2S4 and TiCr2S4 samples were measured as  $8.43 \times 10^{-2}$ ,  $2.47 \times 10^{-1}$ ,  $2.81 \times 10^{-2}$  S cm<sup>-1</sup>, respectively. The lowest conductivity belongs to the TiCr2S4 sample, which may be the reason, together with the ECSA and RF values, for the lowest OER activity of this sample. Comparison of the electrical conductivity values with the literature

shows that conductivities are much better than that of  $\text{ZnS}_2$  ( $1 \times 10^{-6} \text{ S cm}^{-1}$ ) or  $\text{Bi}_2\text{S}_3$  ( $1.8 \times 10^{-7} \text{ S cm}^{-1}$ ) which can be examples for being better conductors of thiospinels than the single-metal sulfides [197]. However, proper comparison can be made when factors effecting electrical conductivity (crystal structure, chemistry, particle size, defects, *etc.*) are almost the same for the samples in this study and the literature [198]. Therefore, electrical conductivity values can only be compared roughly with the literature values.

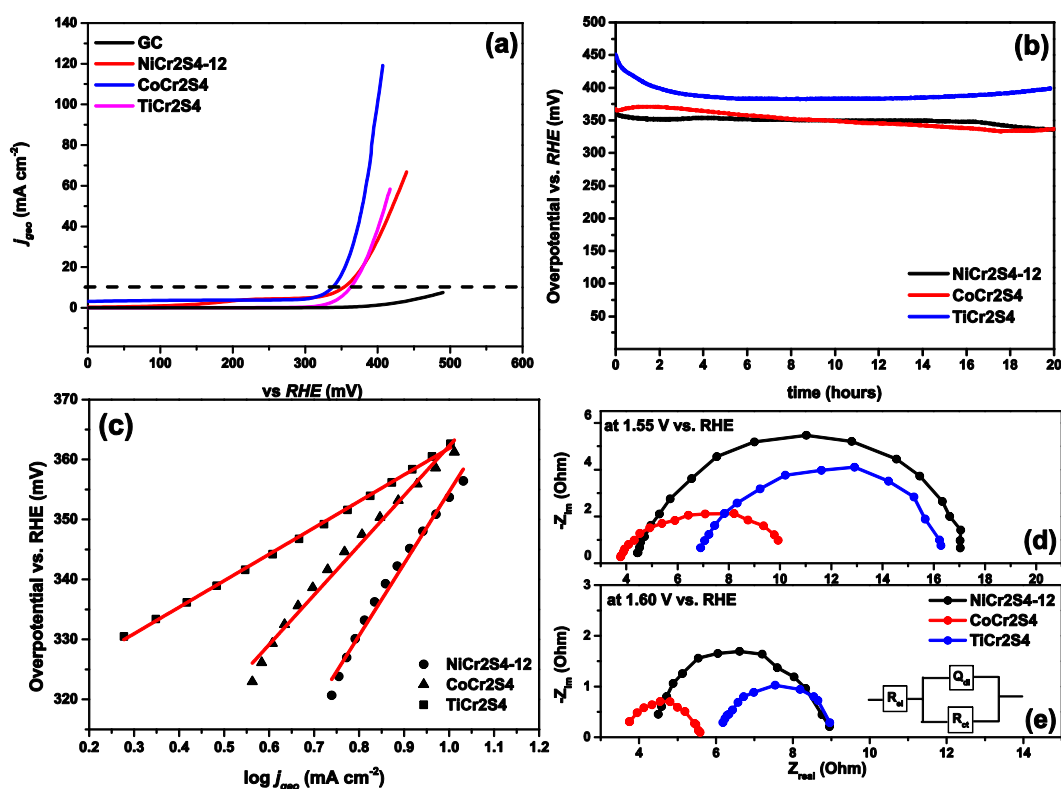


Figure 4.21. (a) LSV curves, (b) CP curves, (c) Tafel slopes and EIS plots at (d) 1.55 V and (e) 1.60 V of the NiCr2S4-12, CoCr2S4 and TiCr2S4 samples.

Intrinsic OER activities of all samples were given in Table 4.9 in comparison. Mass activities of the electrocatalysts were calculated with equation 2.20 and exhibited as  $10.8 \text{ A g}^{-1}$ ,  $23.3 \text{ A g}^{-1}$  and  $8.9 \text{ A g}^{-1}$  for NiCr2S4-12, CoCr2S4 and TiCr2S4 samples,

respectively. CoCr2S4 sample has the largest mass activity supporting the OER performance of this sample. NiCr2S4-12, CoCr2S4 and TiCr2S4 samples yielded 0.00813 s<sup>-1</sup>, 0.01758 s<sup>-1</sup> and 0.00644 s<sup>-1</sup> TOF values, respectively. The highest TOF value was achieved by the CoCr2S4 sample, which again supports the OER activity of this sample, meaning that the number of active catalytic sites is the largest for CoCr2S4 among the other samples. The possible reasons for a large number of active catalytic sites can be the synergetic effect of larger ECSA and RF values together with the electrical conductivity.

Table 4.9 Intrinsic OER activities and Tafel slopes of the NiCr2S4-12, CoCr2S4 and TiCr2S4 samples.

Sample	mass activity			
	$\eta$ (mV) at $j=10 \text{ mA cm}^{-2}$	(A g <sup>-1</sup> ) at $\eta=365 \text{ mV}$	TOF (s <sup>-1</sup> ) at $\eta=365 \text{ mV}$	Tafel Slope (mV dec <sup>-1</sup> )
NiCr2S4-12	356	10.8	0.00813	117
CoCr2S4	338	23.3	0.01758	82
TiCr2S4	363	8.9	0.00644	42

Electrochemical impedance spectroscopy (EIS) data were collected at two different potential values in order to investigate the differences in the kinetic of the samples. In this manner, EIS measurements were carried out at 1.55 V (the onset potential) and at 1.60 V, where a high OER activity can be seen for all samples. Nyquist plots obtained from EIS were given in Figures 4.21(d) and (e). These plots were fitted to Randles equivalent circuit model, shown in Figure 4.21(e) inset. This model consists of an electrolyte resistance ( $R_s$ ), a constant phase element ( $Q_{dl}$ ) and a charge transfer resistance ( $R_{ct}$ ). The fitted parameters are given in Table 4.10. NiCr2S4-12, CoCr2S4 and TiCr2S4 samples yielded 10.6  $\Omega$ , 4.9  $\Omega$  and 7.9  $\Omega$  charge transfer resistances, respectively, at the onset potential (at 1.55 V).  $R_{ct}$  values exhibited as 4.5  $\Omega$ , 1.9  $\Omega$  and 3.1  $\Omega$  for NiCr2S4-12, CoCr2S4 and TiCr2S4 samples, respectively, at 1.60 V.

Decrease in the charge transfer resistance was an expected result indicating a higher charge transport efficiency with increasing working potential.

Table 4.10 Resistance values of the NiCr<sub>2</sub>S<sub>4</sub>-12, CoCr<sub>2</sub>S<sub>4</sub> and TiCr<sub>2</sub>S<sub>4</sub> samples.

<b>Samples</b>	<b>R<sub>ct</sub> at 1.55 V (Ω)</b>	<b>R<sub>ct</sub> at 1.60 (Ω)</b>
NiCr <sub>2</sub> S <sub>4</sub> -12	10.6	4.5
CoCr <sub>2</sub> S <sub>4</sub>	4.9	1.9
TiCr <sub>2</sub> S <sub>4</sub>	5.9	3.1

### 4.3.3 Effect of Crystal Structure on the OER Activity

In this section, the effect of the crystal structure on the OER performance of the nickel-based and cobalt-based metal sulfides was investigated. Firstly, the NiCr<sub>2</sub>S<sub>4</sub>-194 sample, which is identical to the NiAs prototype with a hexagonal ordering (space group P6<sub>3</sub>/mmc, no: 194), was compared to the NiCr<sub>2</sub>S<sub>4</sub>-12 sample, which is identical to the Cr<sub>3</sub>S<sub>4</sub> prototype with a monoclinic structure (space group of C12/m1, no: 12). Crystal structure images of the NiCr<sub>2</sub>S<sub>4</sub>-194 and NiCr<sub>2</sub>S<sub>4</sub>-12 samples were given in Figures 4.22(a) and (b), respectively. Crystal structure information, including the atomic positions and distances between metal and sulfur atoms of the NiCr<sub>2</sub>S<sub>4</sub>-194 and NiCr<sub>2</sub>S<sub>4</sub>-12 samples, were given in Tables 4.11 and 4.12, respectively. Ni and Cr atoms share the same atomic position (Wyckoff position of 2c) in the NiCr<sub>2</sub>S<sub>4</sub>-194 sample, while sulfur atoms occupy 2a sites. The distance between the Ni and S atoms in this structure is 2.399 Å forming perfect octahedral coordination in the hexagonal ordering. In the NiCr<sub>2</sub>S<sub>4</sub>-12 sample having a monoclinic structure, the Ni atoms occupy 2a sites while 4i sites are shared by the S and Cr atoms. The sulfur atoms occupy two different positions in the 4i site, while the Cr atom has only one position in this site. The atomic distances between Ni-S<sub>1</sub>, Ni-S<sub>2</sub>, Cr-S<sub>1</sub> and Cr-S<sub>2</sub> are 2.422, 2.372, 2.461 and 2.442 Å, forming a distorted

octahedra. The crystal structure difference creates differences in the surface atom reconstruction during the OER process [199]. This feature may result in more facile kinetic during the oxygen evolution reaction of the NiCr2S4-194 sample. Crystallographic information of the NiCr2S4-194 and NiCr2S4-12 samples also reveal the structural differences between these two samples leading to differences in the electronic structure. Since the electronic structure has a direct effect on the OER performance, differences in the OER activity and kinetics can be expected with changing crystal structure. The effect of the distances between the atoms on the catalyst performance was already studied in previous literature [200,201]. Jin et al. [202] exhibited that the decreasing distance between the Fe and N atoms in the Fe-N<sub>4</sub> (SAC) structure causes a decrease in the ORR overpotential due to the weakened binding energy of OH<sup>-</sup>. This observation clearly shows that crystal structure affects the catalyst performance by influencing the dynamics in the OER mechanism. However, density functional theory (DFT) calculations can be carried out in order to prove the effects of the crystal structure on the OER performance, but these calculations are not the subject of this study.

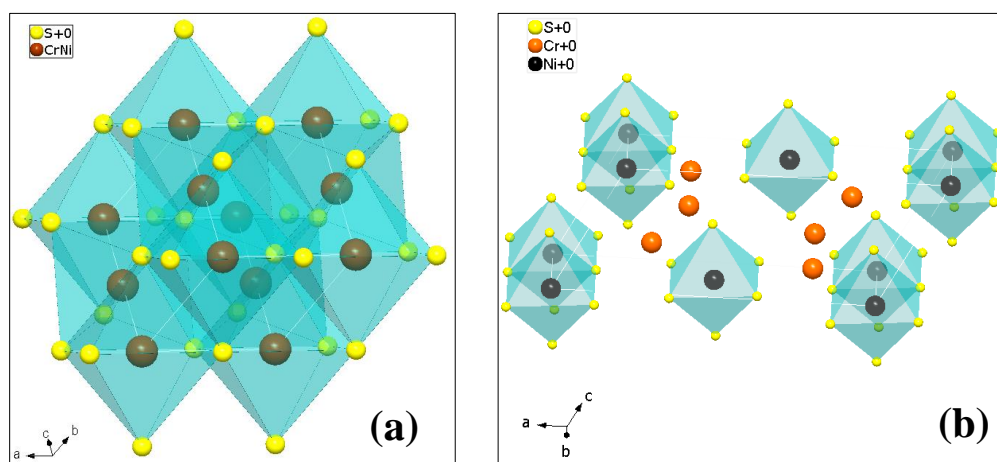


Figure 4.22. Crystal structure images of (a) NiCr<sub>2</sub>S<sub>4</sub>-194 (space group P63/mmc, no: 194) and (b) NiCr<sub>2</sub>S<sub>4</sub>-12 (space group C2/m, no: 12) compounds.

The EDS analysis results of the NiCr<sub>2</sub>S<sub>4</sub>-194 and NiCr<sub>2</sub>S<sub>4</sub>-12 samples were compared in Table 4.13. Elemental compositions are very close to each other within the error limits. Therefore, the composition cannot be a contributing factor to the OER activity of these two samples.

Table 4.11 Crystal structure information of the NiCr<sub>2</sub>S<sub>4</sub>-194 sample.

<b>Atom</b>	<b>Wyckoff position</b>	<b>x</b>	<b>y</b>	<b>z</b>
Ni(Cr)	2c	0	0	0
S	2a	1/3	2/3	1/4
<b>Ni-S distance (Å)</b>		2.399		

Table 4.12 Crystal structure information of the NiCr<sub>2</sub>S<sub>4</sub>-12 sample.

<b>Atom</b>	<b>Wyckoff position</b>	<b>x</b>	<b>y</b>	<b>z</b>
Ni	2a	0	0	0
Cr	4i	0.2563	0	0.2737
S1	4i	0.3705	0	0.0268
S2	4i	0.1092	0	0.4491
<b>Ni-S1 distance (Å)</b>		2.422		
<b>Ni-S2 distance (Å)</b>		2.372		
<b>Cr-S1 distance (Å)</b>		2.461		
<b>Cr-S2 distance (Å)</b>		2.442		

ECSA and RF values were calculated as 17.2 cm<sup>2</sup> and 87.6 for NiCr<sub>2</sub>S<sub>4</sub>-194, 35.1 cm<sup>2</sup> and 178.6 for NiCr<sub>2</sub>S<sub>4</sub>-12 samples, respectively. These values are given in Table 4.14. It can be clearly seen that the NiCr<sub>2</sub>S<sub>4</sub>-12 sample exhibited larger ECSA and RF values than the NiCr<sub>2</sub>S<sub>4</sub>-194 sample. Therefore, better OER activity was expected from the NiCr<sub>2</sub>S<sub>4</sub>-12 sample.

Table 4.13 EDS analysis results of the NiCr2S4-194 and NiCr2S4-12 samples.

<b>Samples</b>	<b>Ni (at %)</b>	<b>Cr (at %)</b>	<b>S (at %)</b>
NiCr2S4-194	21	33	46
NiCr2S4-12	17	37	46

Chronopotentiometry measurements at  $10 \text{ mA cm}^{-2}$  were carried out to test the durability of the samples for 20 hours. Both samples maintained their stability for 20 hours which can be seen in Figures 4.14(b) and 4.21(b). Catalyst performance test graphs were given in Figure 4.23(a-d). NiCr2S4-194 and NiCr2S4-12 samples exhibited 354 mV and 356 mV OER overpotentials, respectively (Figure 4.23(a)). The OER activities are almost the same for these two samples. It seemed that ECSA and RF values have a small contribution to the OER overpotential of the NiCr2S4-12 sample.

Table 4.14 Electrochemical surface area (ECSA) and roughness factor (RF) values of the NiCr2S4-194 and NiCr2S4-12 samples.

<b>Samples</b>	<b>ECSA (cm<sup>2</sup>)</b>	<b>RF</b>
NiCr2S4-194	17.2	87.6
NiCr2S4-12	35.1	178.6

Figure 4.23(b) compares the Tafel slopes of the two samples. NiCr2S4-194 and NiCr2S4-12 samples yielded 59 and 117  $\text{mV dec}^{-1}$  Tafel slopes. Since Tafel slopes are lower than  $120 \text{ mV dec}^{-1}$ , multi-electron transfer reaction is the mechanism for both samples, which were proposed in equations 4.6-4.9. NiCr2S4-12 exhibited a larger Tafel slope than the NiCr2S4-194 sample. It was concluded that the rate-determining step is the chemical reaction after one electron transfer for the NiCr2S4-194 sample while it is the first electron transfer for NiCr2S4-12. The differences in

the OER kinetics are presumably due to the crystal structure effect on the dynamics of the OER mechanism.

Intrinsic OER activities of the samples were given in Table 4.15 in comparison. Mass activities of the electrocatalysts were calculated as 11.8 A g<sup>-1</sup> and 10.8 A g<sup>-1</sup> for NiCr2S4-194 and NiCr2S4-12 samples, respectively. Mass activities were almost the same at the overpotential of 365 mV resulting in the almost the same OER overpotential. Intrinsic OER activities were further analyzed by turnover frequency (TOF) calculations. NiCr2S4-194 and NiCr2S4-12 samples yielded 0.00284 s<sup>-1</sup> and 0.00892 s<sup>-1</sup> TOF values. There is again no significant difference between the TOF values of the two samples.

Table 4.15 Intrinsic OER activities and Tafel slopes of the NiCr2S4-194 and NiCr2S4-12 samples.

Sample	mass activity			
	$\eta$ (mV) at $j=10 \text{ mA cm}^{-2}$	(A g <sup>-1</sup> ) at $\eta=365 \text{ mV}$	TOF (s <sup>-1</sup> ) at $\eta=365 \text{ mV}$	Tafel Slope (mV dec <sup>-1</sup> )
NiCr2S4-194	354	11.8	0.00284	59
NiCr2S4-12	356	10.8	0.00892	117

Electrochemical impedance spectroscopy (EIS) data were collected at two different potential values in order to investigate the differences in the kinetic of the samples. In this manner, EIS measurements were carried out at a small working potential which are the onset potential values of the samples (1.52 V for the NiCr2S4-194 sample and 1.55 V for NiCr2S4-12) and at a large working potential (1.62 V for the NiCr2S4-194 sample and 1.60 V for NiCr2S4-12) where a high OER activity can be seen for the samples. Nyquist plots obtained from EIS were given in Figures 4.23(c) and (d). These plots were fitted to equivalent circuit models, which were shown in the insets. The fitted parameters are given in Table 4.16.

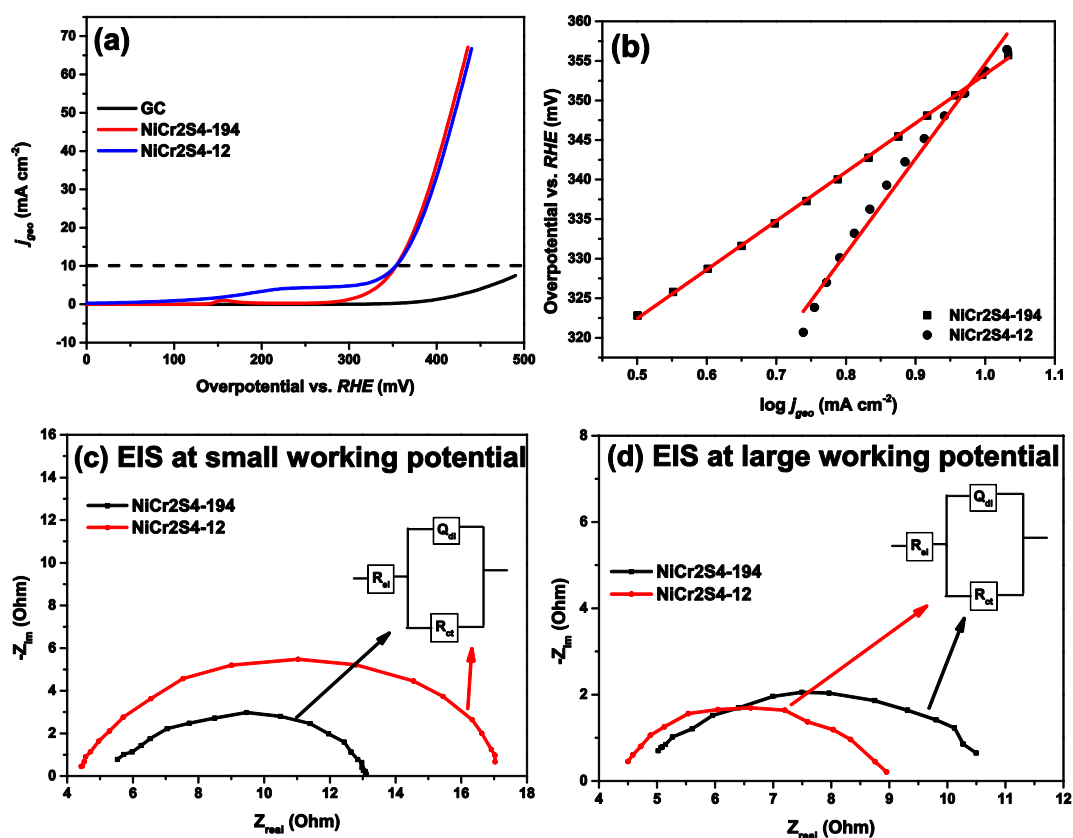


Figure 4.23. (a) LSV curves, (b) Tafel slopes and EIS plots at (c) small and (d) large working potentials of the NiCr2S4-194 and NiCr2S4-12 samples.

NiCr2S4-194 and NiCr2S4-12 samples yielded 7.8  $\Omega$  and 10.6  $\Omega$  charge transfer resistances, respectively, at the onset potential.  $R_{\text{ct}}$  values exhibited as 4.5  $\Omega$  and 5.5  $\Omega$  for NiCr2S4-194 and NiCr2S4-12 samples, respectively, at the large working potential. A decrease in the charge transfer resistance was an expected result indicating a higher charge transport efficiency with increasing working potential. The crystal structure difference creates differences in the surface atom reconstruction during the OER process, which may create easier reaction kinetics as well as lower charge transfer resistance values for the NiCr2S4-194 sample [199]. However, there is no significant effect of the crystal structure on the OER activity of the NiCr2S2-

194 and the NiCr2S4-12 samples. Only kinetic features were affected by the crystal structure of the electrocatalysts.

Table 4.16 Resistance values of the NiCr2S4-194 and NiCr2S4-12 samples.

<b>Samples</b>	<b>R<sub>ct</sub> at the onset potential ( at small working potential)</b>	<b>R<sub>ct</sub> at high OER activity region ( at large working potential)</b>
NiCr2S4-194	7.8 $\Omega$	4.5 $\Omega$
NiCr2S4-12	10.6 $\Omega$	5.5 $\Omega$

The effect of the crystal structure on the OER performance of the cobalt-based sulfides was also investigated. In this manner, the CoS sample, which is identical to the NiAs prototype with a hexagonal ordering (space group P63/mmc, no: 194), was compared to the Co9S8 sample, which is identical to the NaCl prototype with a cubic structure (space group of Fm-3m, no: 225). Crystal structure images of the CoS and Co9S8 samples were given in Figures 4.24(a) and (b), respectively. As can be seen in these Figures that atoms in the hexagonal structure have different surrounding atoms from the cubic phase, which may provide a difference in the surface reconstruction during the OER process. Crystal structure information, including the atomic positions and distances between metal and sulfur atoms of the CoS and Co9S8 samples, were given in Tables 4.17 and 4.18, respectively. Similar to atomic ordering in the NiCr2S4 sample, the Co atoms occupy 2a sites while S atoms occupy 2c sites in the CoS sample. The distance between the Co and S atoms in this structure is 2.327 Å forming perfect octahedral coordination in the hexagonal ordering. The Co and S atoms in the Co9S8 sample occupy two different Wyckoff sites. 32f, 4a, 24e and 8c are the Wyckoff positions of the Co1, Co2, S1 and S2 atoms in the cubic structure. The atomic distances between the Co1-S1, Co1-S2 and Co2-S1 are 2.230, 2.121 and 2.358 Å, forming a distorted octahedral similar to the NiCr2S4-12 sample. Performance differences are expected between the CoS and Co9S8 samples due to

the effect of the crystal structure on the electronic structure, causing changes in the OER mechanism.

The EDS analysis results of the CoS and Co<sub>9</sub>S<sub>8</sub> samples are given in Table 4.19. Elemental analysis results are very close to stoichiometric compositions within the error limits. The Co<sub>9</sub>S<sub>8</sub> sample contains a larger amount of Co and a smaller amount of S than the CoS sample. The effect of Co/S content on OER performance can also be examined since the Co and S contents of the CoS and Co<sub>9</sub>S<sub>8</sub> samples are different from each other.

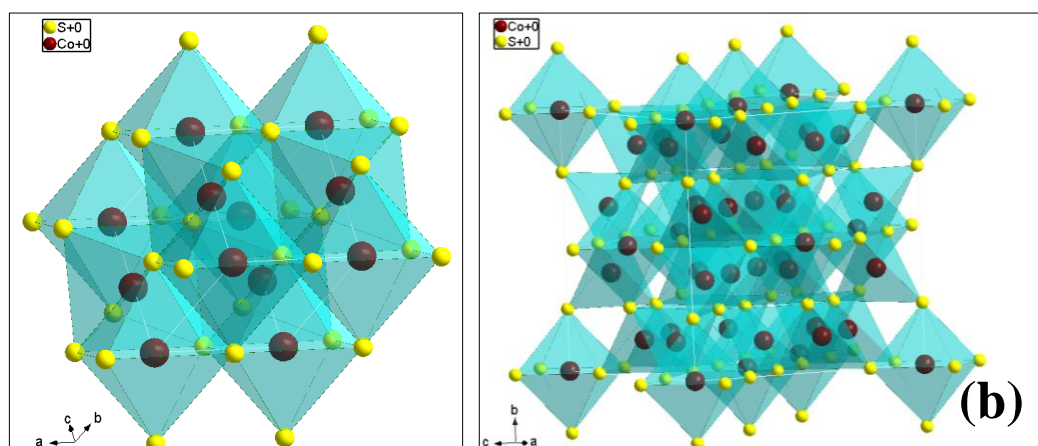


Figure 4.24. Crystal structure images of (a) CoS (space group P63/mmc, no: 194) and (b) Co<sub>9</sub>S<sub>8</sub> (space group Fm-3m, no: 225) compounds.

Table 4.17 Crystal structure information of the CoS sample.

Atom	Wyckoff position	x	y	z
Co	2c	0	0	0
S	2a	1/3	2/3	1/4
<b>Co-S distance (Å)</b>		2.326		

Table 4.18 Crystal structure information of the Co9S8 sample.

<b>Atom</b>	<b>Wyckoff position</b>	<b>x</b>	<b>y</b>	<b>z</b>
Co1	32f	0.3734	0.3734	0.3734
Co2	4a	0	0	0
S1	24e	0.2376	0	0
S2	8c	1/4	1/4	1/4
<b>Co1-S1 distance (Å)</b>		2.230		
<b>Co1-S2 distance (Å)</b>		2.121		
<b>Co2-S1 distance (Å)</b>		2.358		

Catalyst performance test graphs were given in Figure 4.25(a-d). CoS and Co9S8 samples exhibited 364 mV and 381 mV OER overpotentials, respectively (Figure 4.25(a)). There are remarkable differences in OER performances of the Co-based electrocatalysts. The CoS sample yielded a better OER activity than the Co9S8 sample.

Figure 4.25(b) compares the Tafel slopes of the three samples. CoS and Co9S8 samples yielded 46 and 70 mV dec<sup>-1</sup> Tafel slopes, respectively. Since Tafel slopes are lower than 120 mV dec<sup>-1</sup>, multi-electron transfer reaction is the mechanism for both of the samples, which were proposed in equations 4.6-4.9. CoS sample exhibited a smaller Tafel slope than the Co9S8 sample, which can be due to the crystal structure effect facilitating its kinetic. Tafel slopes showed that the rate-determining step is the chemical reaction after one electron transfer for CoS and Co9S8 samples.

ECSA and RF values were calculated as 62.5 cm<sup>2</sup> and 318.9 for CoS, 36.3 cm<sup>2</sup> and 184.9 for Co9S8 samples, respectively. These values are given in Table 4.20. It can be clearly seen that the CoS sample exhibited larger ECSA and RF values than the Co9S8 sample. Therefore, better OER activity was expected from the CoS sample.

Table 4.19 EDS analysis results of the CoS and Co9S8 samples.

<b>Samples</b>	<b>Co (at %)</b>	<b>S (at %)</b>
CoS	49	51
Co9S8	58	42

Table 4.20 Electrochemical surface area (ECSA) and roughness factor (RF) values of the CoS and Co9S8 samples.

<b>Samples</b>	<b>ECSA (cm<sup>2</sup>)</b>	<b>RF</b>
CoS	62.5	318.9
Co9S8	36.3	184.9

Intrinsic OER activities of the samples were given in Table 4.21 in comparison. Mass activities of the electrocatalysts were calculated as 29.7 A g<sup>-1</sup> and 13.1 A g<sup>-1</sup> for CoS and Co9S8 samples, respectively. CoS sample has a larger mass activity supporting the OER performance of this sample. Intrinsic OER activities were further analyzed by turnover frequency (TOF) calculations which were carried out with equation 2.21. CoS and Co9S8 samples yielded 0.00701 s<sup>-1</sup> and 0.00312 s<sup>-1</sup> TOF values, respectively. The TOF value of the CoS sample is larger than that of the Co9S8 sample showing that the number of active sites is larger in the CoS sample. TOF and mass activity values also support the OER performance of the CoS sample.

Chronopotentiometry measurements at 10 mA cm<sup>-2</sup> were carried out to test the durability of the samples for 20 hours. CoS and Co9S8 samples could not maintain their stability for 20 hours. Co9S8 sample showed poorer stability (~20 minutes only) at the current density of 10 mA cm<sup>-2</sup>; however, the CoS sample maintained its stability for 14 hours. It was reported that the O<sub>2</sub> bubbles formed during the OER process could accumulate within the catalyst layer, which may hinder the contact of the electrolyte with the catalyst surface, causing a sudden rise in the OER potential affecting the stability of the samples [203]. Another reason for the sudden increase

in the OER potential resulting in poor stability can be the surface degradation with the applied constant current [204].

Table 4.21 Intrinsic OER activities and Tafel slopes of the CoS and Co9S8 samples.

<b>Samples</b>	<b>mass activity</b>			
	<b><math>\eta</math> (mV) at <math>j=10 \text{ mA cm}^{-2}</math></b>	<b>(A g<sup>-1</sup>) at <math>\eta=395 \text{ mV}</math></b>	<b>TOF (s<sup>-1</sup>) at <math>\eta=395 \text{ mV}</math></b>	<b>Tafel Slope (mV dec<sup>-1</sup>)</b>
CoS	364	29.7	0.00701	46
Co9S8	381	13.1	0.00312	70

Electrochemical impedance spectroscopy (EIS) data were collected at two different potential values in order to investigate further kinetic features of the samples. In this manner, EIS measurements were carried out at a small working potential which are the onset potential values of the samples (1.58 V) and at a large working potential (1.62 V), where a high OER activity can be seen for the samples. Nyquist plots obtained from EIS were given in Figures 4.25(c) and (d). These plots were fitted to equivalent circuit models given in the insets. The fitted parameters to the equivalent circuit models are given in Table 4.22.

Table 4.22 Resistance values of the CoS and Co9S8 samples.

<b>Samples</b>	<b>R<sub>ct</sub> at 1.58 V (<math>\Omega</math>)</b>	<b>R<sub>ct</sub> at 1.62 (<math>\Omega</math>)</b>
CoS	5.4	1.8
Co9S8	18.7	3.4

CoS and Co9S8 samples yielded 5.4  $\Omega$  and 18.7  $\Omega$  charge transfer resistances, respectively, at the onset potential. R<sub>ct</sub> values exhibited as 1.8  $\Omega$  and 3.4  $\Omega$  for CoS and Co9S8 samples, respectively, at a large working potential. A decrease in the

charge transfer resistance at larger potential values was an expected result indicating a higher charge transport efficiency with increasing working potential.

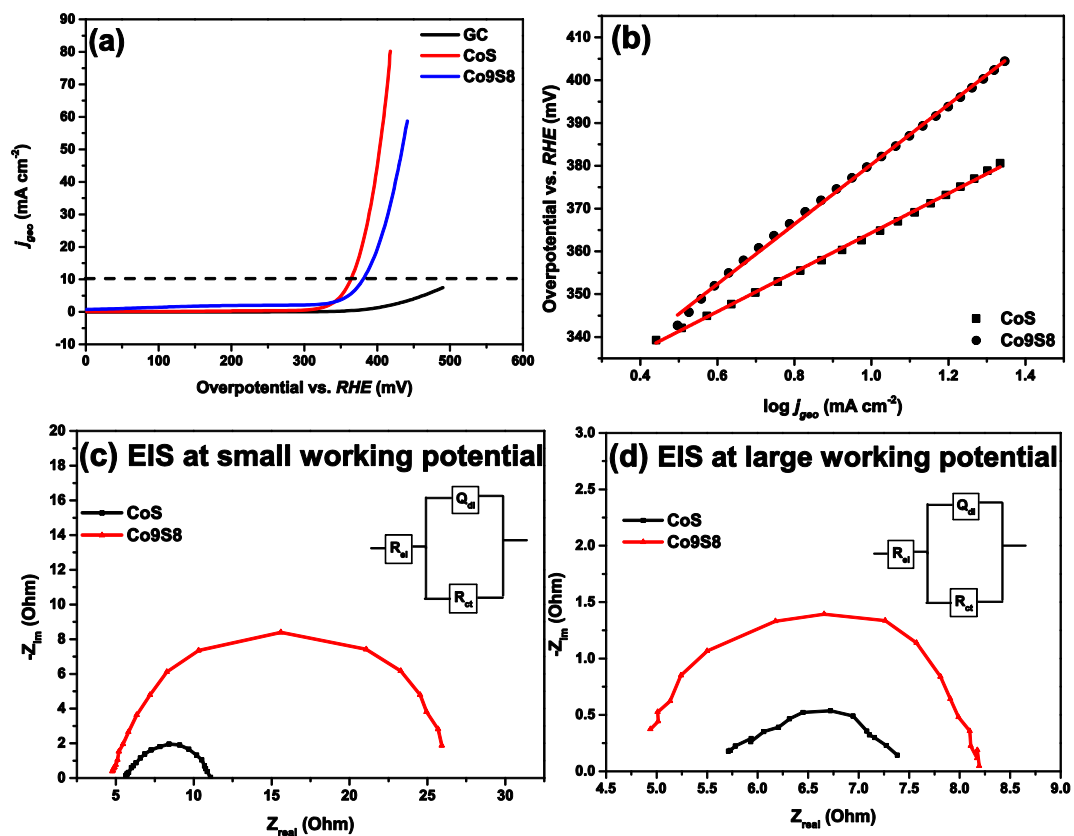


Figure 4.25. (a) LSV curves, (b) Tafel slopes and EIS plots at (c) small and (d) large working potentials of the CoS and Co9S8 samples.

#### 4.3.4 Effect of Crystallinity

The effect of the crystallinity on the OER performance of the Ni, Cr and S containing samples was investigated. In this manner, the NiCr2S4-194 sample, which is identical to the NiAs prototype with a hexagonal ordering (space group P63/mmc, no: 194), was compared to the Ni-Cr-S sample. XRD patterns of these two samples

were given in Figure 4.26. As can be seen in this Figure that there is no peak formation in the XRD pattern of the Ni-Cr-S sample indicating the amorphous structure of this sample. The only difference between the two samples is the heat treatment step. No heat treatment was applied to the Ni-Cr-S sample, while the NiCr2S4-194 sample was heat-treated at 450 °C for 4 h under the N<sub>2</sub> atmosphere.

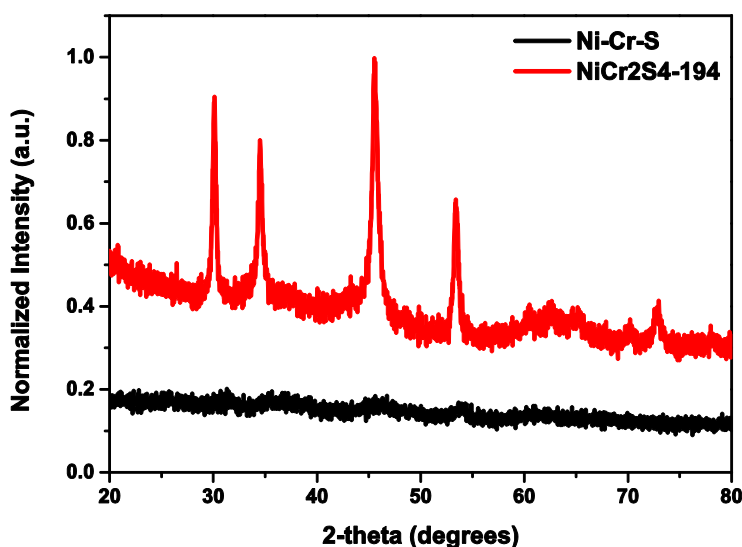


Figure 4.26. XRD pattern of the NiCr2S4-194 and Ni-Cr-S samples.

The EDS analysis results of the NiCr2S4-194 and Ni-Cr-S samples are given in Table 4.23. Ni, Cr and S contents of the NiCr2S4-194 and Ni-Cr-S samples are almost identical and very close to stoichiometric compositions within the error limits. The composition of the Ni, Cr and S containing sample did not change upon heat treatment at 450 °C.

ECSA and RF values were calculated with equations 2.18 and 2.19 as 17.2 cm<sup>2</sup> and 87.6 for NiCr2S4-194, 36.7 cm<sup>2</sup> and 187.3 for Ni-Cr-S samples, respectively. These values are given in Table 4.24. It can be clearly seen that the Ni-Cr-S sample exhibited larger ECSA and RF values than the NiCr2S4-194 sample. Therefore, better OER activity was expected from the Ni-Cr-S sample.

Table 4.23 EDS analysis results of the NiCr2S4-194 and Ni-Cr-S samples.

<b>Samples</b>	<b>Ni (at %)</b>	<b>Cr (at %)</b>	<b>S (at %)</b>
NiCr2S4-194	21	33	46
Ni-Cr-S	22	32	46

Catalyst performance test graphs were given in Figure 4.26(a-d). NiCr2S4-194 and Ni-Cr-S samples exhibited 354 mV and 329 mV OER overpotentials, respectively (Figure 4.27(a)). There are remarkable differences in OER performances of the NiCr2S4-194 and Ni-Cr-S electrocatalysts. The Ni-Cr-S sample yielded better OER activity than the crystalline sample. A larger number of active sites and more rapid ionic transport may be the two significant reasons explaining the differences between the OER activities of the NiCr2S4-194 and Ni-Cr-S samples [205]. The calculated ECSA and RF values in Table 4.24 also support this explanation.

Table 4.24 Electrochemical surface area (ECSA) and roughness factor (RF) values of the NiCr2S4-194 and Ni-Cr-S samples.

<b>Samples</b>	<b>ECSA (cm<sup>2</sup>)</b>	<b>RF</b>
NiCr2S4-194	17.2	87.6
Ni-Cr-S	36.7	187.3

Figure 4.27(b) compares the Tafel slopes of the two samples. NiCr2S4-194 and Ni-Cr-S samples yielded 59 and 44 mV dec<sup>-1</sup> Tafel slopes. Since Tafel slopes are lower than 120 mV dec<sup>-1</sup>, multi-electron transfer reaction is the mechanism for both of the samples, which were proposed in equations 4.6-4.9. The Ni-Cr-S sample exhibited a smaller Tafel slope than the NiCr2S4-194 sample, which can be due to the smaller particle size of the Ni-Cr-S sample. Nano-sized particles of the Ni-Cr-S sample (Figure 4.4(g)) provided better OER activity and more rapid kinetics due to increased surface area as compared to the sub-micron-sized NiCr2S4-194 sample (Figure

4.4(f)). Tafel slopes showed that the rate-determining step is the chemical reaction after one electron transfer for the NiCr2S4-194 sample and the third electron transfer reaction for the Ni-Cr-S sample indicating an enhanced reaction kinetics.

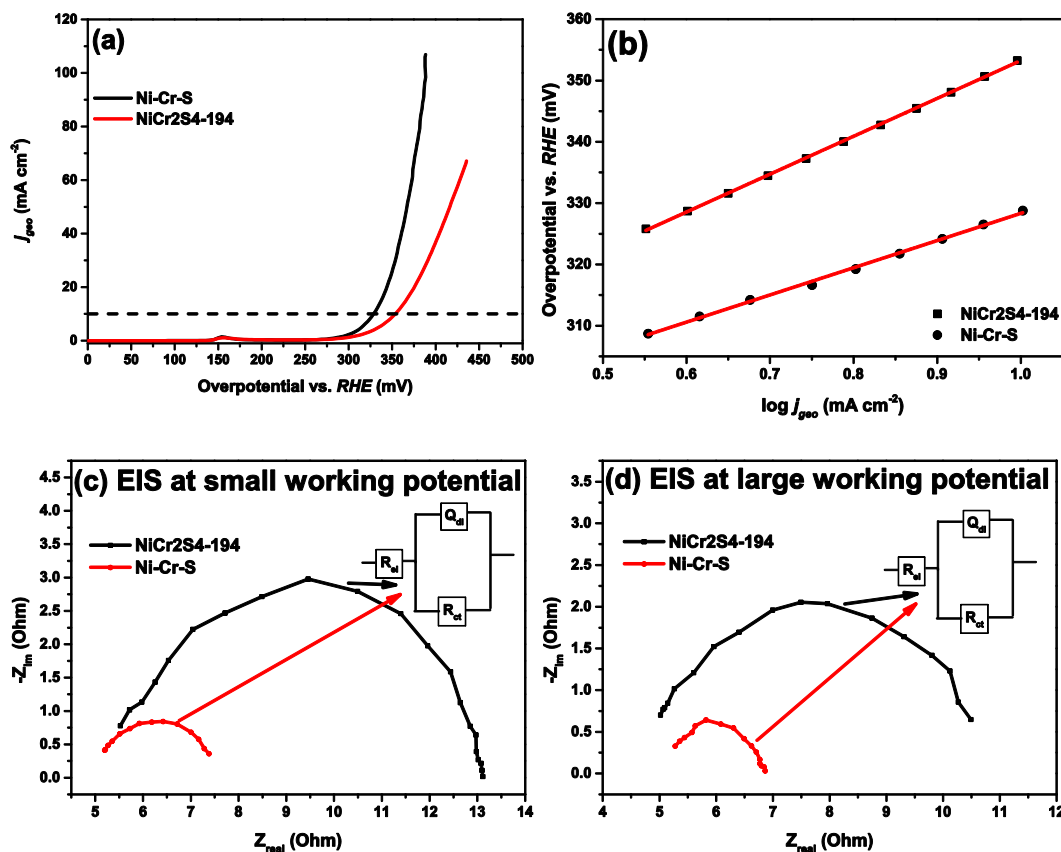


Figure 4.27. (a) LSV curves, (b) Tafel slopes and EIS plots at (c) small and (d) large working potentials of the NiCr2S4-194 and Ni-Cr-S samples.

The electrical conductivity of the amorphous structures is generally lower than that of their crystalline form due to the disordered arrangement of atoms in the structure. In order to see that, electrical conductivity measurements of the samples were also carried out and NiCr2S4-194 and Ni-Cr-S samples exhibited  $8.55 \times 10^{-7} \text{ S cm}^{-1}$  and  $2.16 \times 10^{-7} \text{ S cm}^{-1}$  conductivity values, respectively. The conductivity of the Ni-Cr-S sample was lower than that of the crystalline NiCr2S4-194 sample, as expected. However, OER activity and reaction kinetics were not affected much by the

conductivity values. Larger values of the ECSA and RF may be the dominating reason for the better performance of the Ni-Cr-S as compared to the crystalline NiCr2S4-194 sample.

Chronopotentiometry measurements at  $10 \text{ mA cm}^{-2}$  were carried out to test the durability of the samples for 20 hours. NiCr2S4-194 sample showed good stability upon 20 h, which was already discussed in section 4.3.1. However, the amorphous Ni-Cr-S sample exhibited extremely poor stability ( $\sim 30$  minutes only) at the current density of  $10 \text{ mA cm}^{-2}$  which can be seen in Figure 4.28. Surface degradation, the difference in the electronic structure of the amorphous and crystalline samples and the accumulation of the  $\text{O}_2$  bubbles within the catalyst layer may be the possible reasons for the poor stability of the amorphous Ni-Cr-S sample [203,204].

Intrinsic OER activities of the samples were given in Table 4.25 in comparison. Mass activities of the electrocatalysts exhibited  $9.3 \text{ A g}^{-1}$  and  $31.6 \text{ A g}^{-1}$  for NiCr2S4-194 and Ni-Cr-S samples, respectively. Ni-Cr-S sample has a larger mass activity supporting the OER performance of this sample. Intrinsic OER activities were further analyzed by turnover frequency (TOF) calculations. NiCr2S4-194 and Ni-Cr-S samples yielded  $0.00223 \text{ s}^{-1}$  and  $0.00757 \text{ s}^{-1}$  TOF values, respectively. The Ni-Cr-S sample exhibited a larger TOF value than the NiCr2S4-194 sample due to a larger number of active sites of the Ni-Cr-S sample. TOF and mass activity values also support the OER performance of the Ni-Cr-S sample.

Table 4.25 Intrinsic OER activities and Tafel slopes of the NiCr2S4-194 and Ni-Cr-S samples.

Samples	$\eta$ (mV) at	mass activity		
	$j=10 \text{ mA cm}^{-2}$	( $\text{A g}^{-1}$ ) at $\eta=360 \text{ mV}$	TOF ( $\text{s}^{-1}$ ) at $\eta=360 \text{ mV}$	Tafel Slope ( $\text{mV dec}^{-1}$ )
NiCr2S4-194	354	9.3	0.00223	59
Ni-Cr-S	329	31.6	0.00757	44

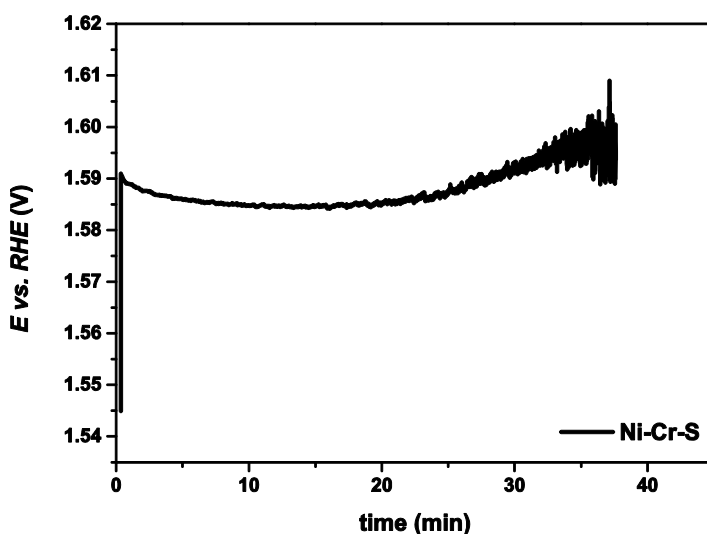


Figure 4.28. CP curve of the amorphous Ni-Cr-S sample.

Electrochemical impedance spectroscopy (EIS) data were collected at two different potential values in order to investigate further kinetic features of the samples. In this manner, EIS measurements were carried out at a small working potential which are the onset potential values of the samples (1.52 V) and at a large working potential (1.62 V), where a high OER activity can be seen for the samples. Nyquist plots obtained from EIS were given in Figures 4.27(c) and (d). These plots were fitted to Randles equivalent circuit models, which were shown in the insets. The fitted parameters to Randles equivalent circuit model are given in Table 4.26.

NiCr<sub>2</sub>S<sub>4</sub>-194 and Ni-Cr-S samples yielded 7.8  $\Omega$  and 2.6  $\Omega$  charge transfer resistances, respectively, at the onset potential.  $R_{ct}$  values exhibited as 5.5  $\Omega$  and 1.8  $\Omega$  for NiCr<sub>2</sub>S<sub>4</sub>-194 and Ni-Cr-S samples, respectively, at a large working potential. A decrease in the charge transfer resistance was an expected result indicating a higher charge transport efficiency with increasing working potential. Ni-Cr-S sample exhibited very small charge transfer resistance values together with the smaller Tafel slope as compared to the NiCr<sub>2</sub>S<sub>4</sub>-194 sample indicating enhanced kinetic features of the amorphous sample.

Table 4.26 Resistance values of the NiCr2S4-194 and Ni-Cr-S samples.

<b>Samples</b>	<b>R<sub>ct</sub> at the onset potential (at small working potential)</b>	<b>R<sub>ct</sub> at high OER activity region (at large working potential)</b>
NiCr2S4-194	7.8 Ω	5.5 Ω
Ni-Cr-S	2.6 Ω	1.8 Ω

#### **4.4 Electrochemical Characterization of Transition Metal Sulfides in Li-Battery Systems**

The electrochemical energy storage performance of NiCr2S4-194 samples was tested with galvanostatic cycling with a potential limitation procedure. Electrodes were coated on Cu-foil and Al-foil current collectors separately in order to investigate the performance of active materials within a wider potential window. 1.5 M LiPF<sub>6</sub> in EC: EMC: DMC (3: 4: 3, v/v), 0.5% VC, 1 % AB43 solution was used as an electrolyte. Samples coated onto Al-foil were tested from 2.5 V to 4 V, but high voltage performances were extremely poor. However, sample coated onto Cu-foil yielded 793 mAh g<sup>-1</sup> first discharge capacity (within the potential range of 0.001 V – 2 V at 50 mA g<sup>-1</sup>) in 1.5 M LiPF<sub>6</sub> in EC: EMC: DMC electrolyte system. This first discharge capacity is a very promising result as compared to the literature since Fan et al. [206] received 738 mAh g<sup>-1</sup> capacity (within 0.001 V - 3 V at 50 mA g<sup>-1</sup>) from NiCo<sub>2</sub>S<sub>4</sub> and Guo et al. [207] received 920 mAh g<sup>-1</sup> capacity (within 0.005 V - 3 V at 100 mA g<sup>-1</sup>) from FeNi<sub>2</sub>S<sub>4</sub> anodes for Li-systems.

It was reported in the literature that sulfur-based materials are not stable in the carbonate-based electrolytes causing a poor discharge capacity even in the first cycle [208]. However, Yamauchi et al. [209] exhibited an improvement in the carbonate-based electrolyte system for the Li<sub>2</sub>S positive electrode by making a composite structure with FeS and coating it with TiO<sub>2</sub> by preventing the sulfur deactivation causing the surface degradation. NiCr2S4-194 sample in 1.5 M LiPF<sub>6</sub> in EC: EMC:

DMC electrolyte showed a promising performance which can be due to the fact that negative effects of the electrolyte on the performance could already be suppressed by the chemistry of the NiCr<sub>2</sub>S<sub>4</sub>-194 sample similar to FeS compounding of the Li<sub>2</sub>S electrode in the Yamauchi's study [209].

Figure 4.29 compares the performances of Ni-Cr-S and NiCr<sub>2</sub>S<sub>4</sub>-194 samples. It demonstrates the effect of the crystallinity on performances as Li-ion battery electrodes. Ni-Cr-S and NiCr<sub>2</sub>S<sub>4</sub>-194 samples were coated onto Cu-foil and tested in a 1.5 M LiPF<sub>6</sub> in EC: EMC: DMC electrolyte system with a current density of 50 mA g<sup>-1</sup> from 2 V to 0.001 V. Ni-Cr-S and NiCr<sub>2</sub>S<sub>4</sub>-194 samples yielded 344 mAh g<sup>-1</sup> and 793 mAh g<sup>-1</sup> specific discharge capacities, respectively. Amorphous Ni-Cr-S exhibited much lower specific discharge capacity, presumably due to its poorer electrical conductivity ( $2.16 \times 10^{-7}$  S cm<sup>-1</sup>) compared to that of the NiCr<sub>2</sub>S<sub>4</sub>-194 sample ( $8.55 \times 10^{-7}$  S cm<sup>-1</sup>). Moreover, the disordered arrangement of the Ni-Cr-S atoms throughout the structure may hinder the motion of the lithium ions within the structure, which may cause capacity losses.

The binder and additive effect were analyzed by changing the electrode composition. Figure 4.30 demonstrates the NiCr<sub>2</sub>S<sub>4</sub>-194 samples with electrode compositions of (active material: carbon: binder) 8:1:1 and 6:2:2. Electrodes were coated onto Cu-foil and tested in a 1.5 M LiPF<sub>6</sub> in EC: EMC: DMC electrolyte system with a current density of 50 mA g<sup>-1</sup> from 2 V to 0.001 V. NiCr<sub>2</sub>S<sub>4</sub>-194-(8:1:1) and NiCr<sub>2</sub>S<sub>4</sub>-194-(6:2:2) samples yielded 794 mAh g<sup>-1</sup> and 815 mAh g<sup>-1</sup> specific discharge capacities, respectively. An increase in carbon and binder content resulted in the 21 mAh g<sup>-1</sup> increase in specific discharge capacity.

The effect of crystal structure on the performance as a Li-ion battery electrode was demonstrated in Figure 4.31. Electrodes were coated onto Cu-foil and tested in a 1.5 M LiPF<sub>6</sub> in EC: EMC: DMC electrolyte system with a current density of 50 mA g<sup>-1</sup> from 2 V to 0.001 V. NiCr<sub>2</sub>S<sub>4</sub>-194 and NiCr<sub>2</sub>S<sub>4</sub>-12 samples yielded 815 mAh g<sup>-1</sup> and 764 mAh g<sup>-1</sup> specific discharge capacities, respectively. The specific discharge capacity of the hexagonal NiCr<sub>2</sub>S<sub>4</sub>-194 sample was 51 mAh g<sup>-1</sup> larger than that of

the NiCr2S4-12 sample. One of the possible reasons for this difference can be the differences in particle sizes. As can be seen in the SEM micrographs of NiCr2S4-12 and NiCr2S4-194 samples given in Figures 4.3(g) and 4.4(i), the particle size of the NiCr2S4-12 sample is larger than that of NiCr2S4-194 sample. The heat treatment temperature of the NiCr2S4-12 sample was 900 °C, while the heat treatment of the NiCr2S4-194 sample was carried out at 450 °C. High temperatures may induce the coarsening of the particles. If the active material of an electrode is composed of large particles, it may cause inhomogeneous distribution of the slurry onto the current collector and a decrease in the electrical conductivity as well, which may result in capacity losses.

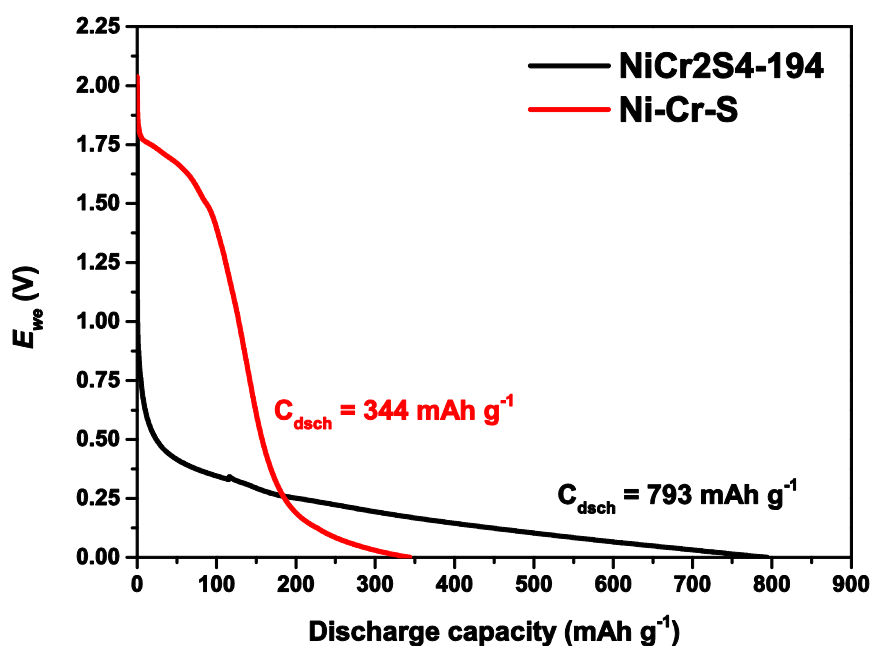


Figure 4.29. Cell potential vs. specific discharge capacity curves of NiCr2S4-194 and Ni-Cr-S samples coated onto Cu-foil in 1.5 M LiPF<sub>6</sub> in EC: EMC: DMC electrolyte system.

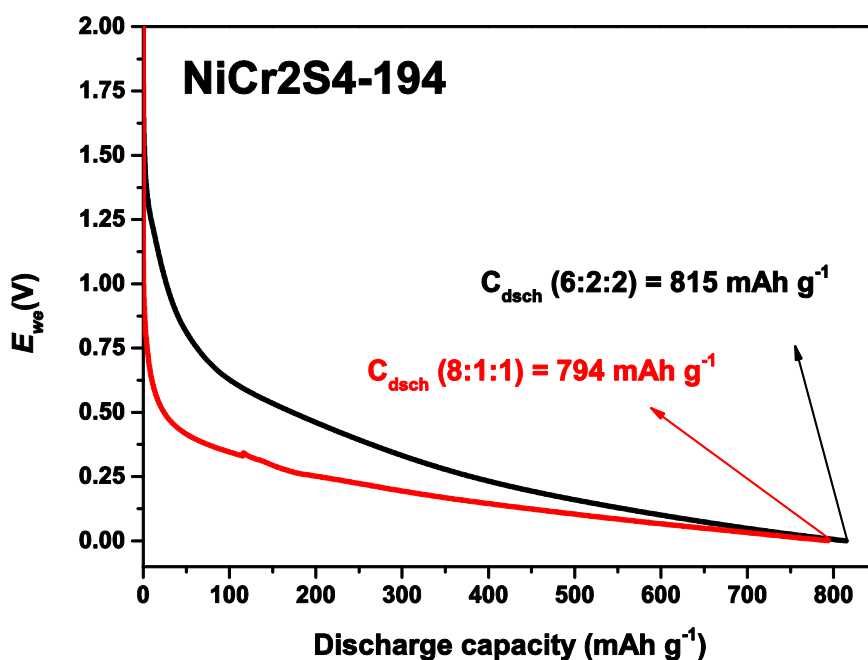


Figure 4.30. Cell potential vs. specific discharge capacity curves of NiCr<sub>2</sub>S<sub>4</sub>-194 samples with electrode compositions of (active material: carbon: binder) 8:1:1 and 6:2:2.

Another possible reason for the capacity difference can be the effect of crystal structure on performance. As can be seen in Figures 1.2 (a) and (b), a hexagonal structure with a space group no. 194 is a more open structure to accept Li-ions during charging/discharging which may be the reason for the better specific discharge capacity of NiCr<sub>2</sub>S<sub>4</sub>-194 sample. The atomic arrangement in the monoclinic structure with a space group no. 12 may restrict the diffusion of lithium ions into the structure, which may cause capacity losses.

The chemistry effect on the Li-ion battery performance was investigated in monoclinic ACr<sub>2</sub>S<sub>4</sub> (where A= Ni, Co, Ti) systems. Specific capacity curves at the first cycle at 50 mA g<sup>-1</sup> were given in Figure 4.32(a). The first specific discharge capacities yielded 764 mAh g<sup>-1</sup>, 954 mAh g<sup>-1</sup> and 879 mAh g<sup>-1</sup> for the NiCr<sub>2</sub>S<sub>4</sub>-12, CoCr<sub>2</sub>S<sub>4</sub>, TiCr<sub>2</sub>S<sub>4</sub> electrodes, respectively. CoCr<sub>2</sub>S<sub>4</sub> sample demonstrated the best first discharge capacity at 50 mA g<sup>-1</sup> among all samples investigated in this study.

Coulombic efficiency values of the NiCr2S4-12, CoCr2S4, TiCr2S4 electrodes were 99 %, 96 % and 98 %, respectively. Similarly, coulombic efficiencies of the electrodes were significantly high at 100 mA g<sup>-1</sup> upon 50 cycles as well, which can clearly be seen in Figure 4.32(b).

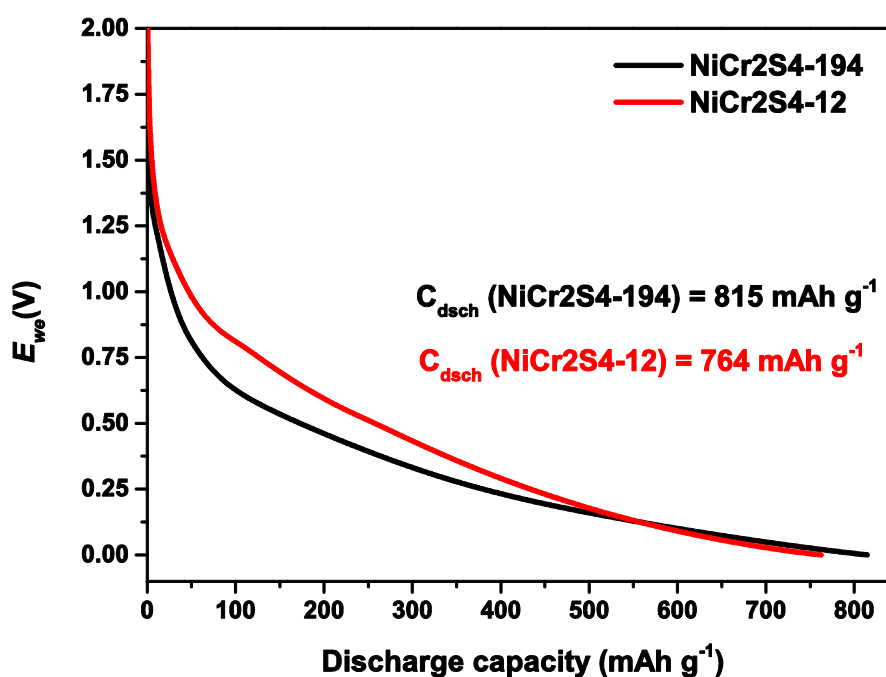


Figure 4.31. Cell potential vs. specific discharge capacity curves of NiCr2S4-194 and NiCr2S4-12 samples.

Capacity retention values were also obtained from Figure 4.32(b) as 50 %, 20 % and 73 % for the NiCr2S4-12, CoCr2S4, TiCr2S4 samples, respectively. Among the three samples, the TiCr2S4 electrode showed the best capacity retention value upon 50 cycles. TiCr2S4 sample exhibited 610  $\text{mAh g}^{-1}$  and 442  $\text{mAh g}^{-1}$  specific discharge capacity at the beginning and the end of the 50 cycles, respectively. The specific discharge capacity of the TiCr2S4 sample after 50 cycles was larger than that of NiCr2S4-12 and CoCr2S4 samples. Although CoCr2S4 (675  $\text{mAh g}^{-1}$ ) sample

started cycling with a capacity larger than that of NiCr2S4-12 and TiCr2S4 samples, it ended cycling with a capacity value (129 mAh g<sup>-1</sup>) lower than that of NiCr2S4-12 (183 mAh g<sup>-1</sup>) and TiCr2S4 (442 mAh g<sup>-1</sup>) electrodes. Specific discharge capacities and the capacity retention values after 50 cycles at 100 mA g<sup>-1</sup> of the samples were summarized in Table 4.27.

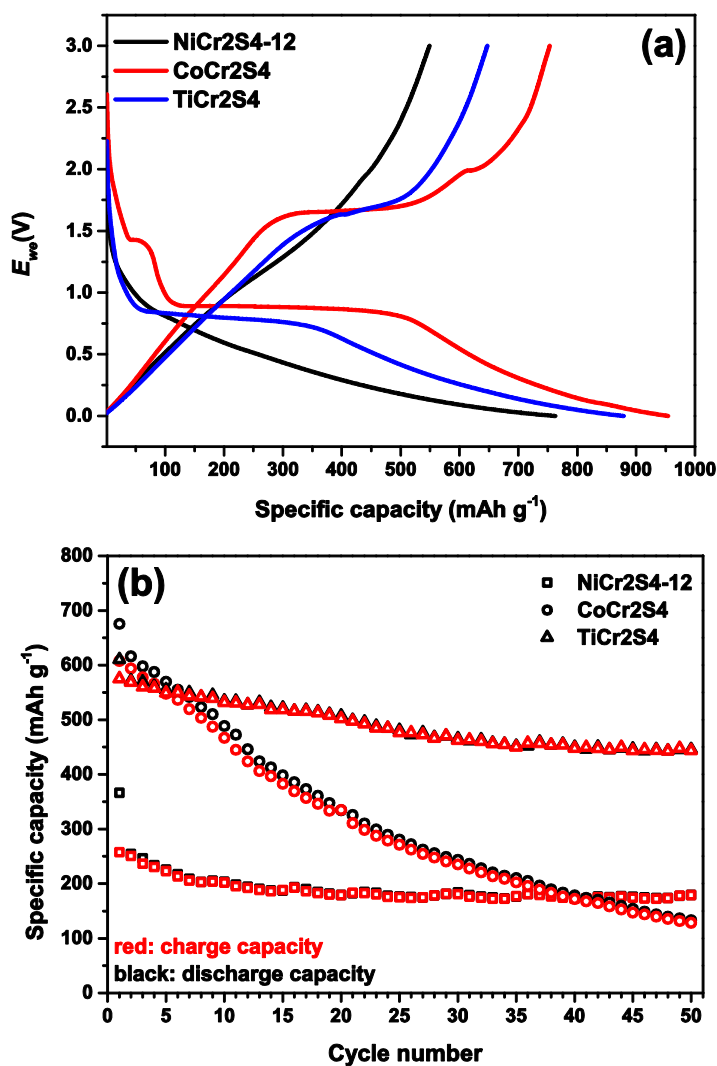


Figure 4.32. (a) Specific capacity curves at the first cycle at 50 mA g<sup>-1</sup> and (b) Capacity retention cycles of the NiCr2S4-12, CoCr2S4, TiCr2S4 at 100 mA g<sup>-1</sup>.

Table 4.27 Li-ion battery performances of the NiCr2S4-12, CoCr2S4, TiCr2S4 electrodes.

<b>Samples</b>	<b>First Discharge Capacity at 50 mA g<sup>-1</sup> (mAh g<sup>-1</sup>)</b>	<b>Discharge Capacity at 100 mA g<sup>-1</sup> (mAh g<sup>-1</sup>)</b>	<b>Discharge Capacity at 100 mA g<sup>-1</sup> after 50 cycles (mAh g<sup>-1</sup>)</b>	<b>Capacity Retention after 50 cycles (%)</b>
NiCr2S4-12	764	366	183	50
CoCr2S4	954	675	129	20
TiCr2S4	879	610	442	73

Electrochemical impedance spectroscopy (EIS) data were collected from the as-assembled cells and the electrodes after 50 cycles at 100 mA g<sup>-1</sup>. Nyquist plots obtained from EIS measurements were given in Figures 4.32(a) and (b). All plots have one semi-circle in the high-medium frequency range indicating the charge transfer kinetics of the electrodes [210] and an inclined line at the low-frequency range, which was ascribed to the finite space Warburg (FSW) due to semi-infinite diffusion of the ions in structure [211]. These plots were fitted to an equivalent circuit model, shown in the insets of Figure 4.33. Equivalent circuit models consist of constant phase elements (Q<sub>dl</sub> and Q<sub>ct</sub>) used for calculations of the double-layer capacitance and charge transfer capacitance, surface film resistance (R<sub>sf</sub>) and charge transfer resistance (R<sub>ct</sub>) connected in parallel to the Q<sub>dl</sub>. The model also contains electrolyte resistance (R<sub>s</sub>) connected in series to all other equivalent circuit elements.

Figure 4.33(a) represents the electrochemical impedance spectra of the as-assembled cells. Electrolyte resistance values of the NiCr2S4-12, CoCr2S4, TiCr2S4 samples were 3.8 Ω, 3.7 Ω and 4.3 Ω, respectively, which were very close to each other as expected since the same electrolyte solution was used for all of the samples. Surface film resistances were not observed in the as-assembled cells because it forms upon cycling of the battery [212]. NiCr2S4-12, CoCr2S4, and TiCr2S4 samples exhibited 16.3 Ω, 18.1 Ω and 23.7 Ω charge transfer resistance values, respectively. Charge transfer resistance values were very close to each other. Therefore, resistance values

did not cause any distinctive results. The larger slope of the inclined line part of the CoCr2S4 sample in the low-frequency region shows rapid ion transfer characteristics [109] which may be the reason for the best discharge capacity of this sample in the first cycle.

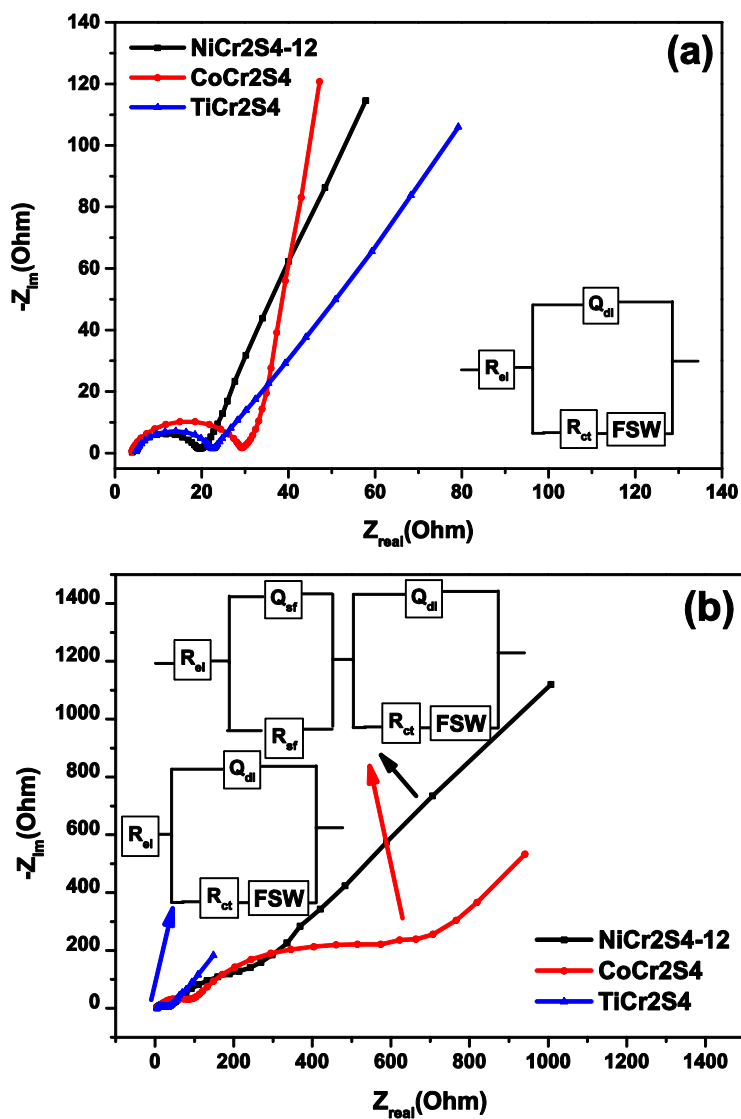


Figure 4.33. Nyquist plots of (a) as-assembled and (b) after 50 cycles at  $100 \text{ mA g}^{-1}$  of the NiCr2S4-12, CoCr2S4, TiCr2S4 electrodes.

Figure 4.33(b) demonstrates the Nyquist plots of the NiCr<sub>2</sub>S<sub>4</sub>-12, CoCr<sub>2</sub>S<sub>4</sub>, and TiCr<sub>2</sub>S<sub>4</sub> electrodes after 50 cycles at 100 mA g<sup>-1</sup>. A second semi-circle was observed upon cycling in the NiCr<sub>2</sub>S<sub>4</sub> and CoCr<sub>2</sub>S<sub>4</sub> electrode surfaces, indicating a surface film formation which may be the reason for the large capacity loss of these two samples. Nyquist plot of the TiCr<sub>2</sub>S<sub>4</sub> sample remained unchanged after 50 cycles which were ascribed to its electrochemical stability upon cycling. The slopes of the inclined line part of the NiCr<sub>2</sub>S<sub>4</sub> and CoCr<sub>2</sub>S<sub>4</sub> samples in the low-frequency region were decreased upon cycling. At the end of the 50 cycles, the TiCr<sub>2</sub>S<sub>4</sub> sample exhibited the largest slope indicating rapid ion transfer characteristics [109].

CoCr<sub>2</sub>S<sub>4</sub> sample showed the best performance among the other samples. All samples, except the Ni-Cr-S sample (344 mAh g<sup>-1</sup>), exhibited a specific discharge capacity larger than 750 mAh g<sup>-1</sup>. These values were very close to their counterparts in the literature [213–215]. Therefore, transition metal sulfides investigated in this study are promising Li-ion battery anodes.

#### 4.5 Summary

Transition metal sulfides were synthesized via microwave-assisted synthesis method and their performances as OER electrocatalysts and Li-battery electrodes were tested. The reaction mechanism of microwave-assisted synthesis of metal sulfides was proposed when thiourea was used as a sulfur source in the first section. Unary and/or binary forms of the CoS, Co<sub>9</sub>S<sub>8</sub>, Cr<sub>3</sub>S<sub>4</sub>, CoCr<sub>2</sub>S<sub>4</sub>, CoS<sub>2</sub>, NiS, NiS<sub>2</sub>, NiCr<sub>2</sub>S<sub>4</sub>, Ni<sub>3</sub>S<sub>4</sub>, N<sub>3</sub>S<sub>2</sub> and TiCr<sub>2</sub>S<sub>4</sub> phases were the materials groups which were tested in this study. Then structural, morphological and chemical features were investigated. The heat treatment process was carried out at different temperatures (400, 450 and 900 °C) for the Co-S system and CoS, Co<sub>9</sub>S<sub>8</sub> phases and CoS-Co<sub>9</sub>S<sub>8</sub> phase mixture were obtained. Similarly, NiS<sub>2</sub>- CrS phase mixture formed at 300 °C, NiCr<sub>2</sub>S<sub>4</sub> with a space group no:194 at 450 °C, NiCr<sub>2</sub>S<sub>4</sub> with a space group no:12 at 900 °C were also obtained. The same chemistry with different crystal structures provided distinctive performances as OER electrocatalysts. OER overpotentials and Tafel

slopes of the OER electrocatalysts in this study were given in Table 4.28. All samples exhibited better OER activity than the benchmark RuO<sub>2</sub> electrocatalyst [192]. The kinetics of the samples were also better than the benchmark RuO<sub>2</sub> (except the NiCr<sub>2</sub>S<sub>4</sub>-12 sample) indicating that all samples in this study are promising electrocatalysts for oxygen evolution reaction.

Table 4.28 Summary of the OER electrocatalyst performances.

<b>Sample</b>	<b>OER Overpotential (mV)</b>	<b>ECSA (cm<sup>2</sup>)</b>	<b>RF</b>	<b>Tafel Slope (mv dec<sup>-1</sup>)</b>
RuO <sub>2</sub> [192]	387			90
CoS	364	62.5	318.9	46
Co <sub>9</sub> S <sub>8</sub>	381	36.3	184.9	70
CoCr <sub>2</sub> S <sub>4</sub>	338	75.3	382.7	82
NiS-mw	372	12.8	65.1	60
Ni-Cr-S	329	36.7	187.3	44
NiCr <sub>2</sub> S <sub>4</sub> -194	354	17.2	87.6	59
NiCr <sub>2</sub> S <sub>4</sub> -12	356	35.1	178.6	117
Cr/NiS	334	16.3	82.9	42
TiCr <sub>2</sub> S <sub>4</sub>	363	25.2	127.6	42

Firstly, the effect of chromium incorporation into the NiS (space group no:194) structure was investigated. The presence of chromium improved the OER activity of the NiS sample from 372 mV to 334 mV for 2 at.% Cr containing NiS sample and to 354 mV for 33 at.% Cr containing NiS sample at 10 mA cm<sup>-2</sup>.

ACr<sub>2</sub>S<sub>4</sub> (where A= Ni, Co, Ti) samples with a space group no:12 were studied secondly to investigate the effect of the A-site element in the ACr<sub>2</sub>S<sub>4</sub> compound. Single-phase NiCr<sub>2</sub>S<sub>4</sub>, CoCr<sub>2</sub>S<sub>4</sub> and TiCr<sub>2</sub>S<sub>4</sub> compounds were tested as OER

electrocatalysts and Li-ion battery anodes. NiCr<sub>2</sub>S<sub>4</sub>-12, CoCr<sub>2</sub>S<sub>4</sub> and TiCr<sub>2</sub>S<sub>4</sub> samples exhibited 356 mV, 338 mV and 363 mV OER overpotentials, respectively.

The effect of crystal structure on the OER performance was investigated in Co-S and Ni-Cr-S systems. In this regard, the NiCr<sub>2</sub>S<sub>4</sub> phase with two different crystal structures (space group no:194 and 12) having hexagonal and monoclinic ordering were compared in terms of OER activity. Stability and OER activities were almost the same, but there was a remarkable difference in the Tafel slopes. NiCr<sub>2</sub>S<sub>4</sub>-194 and NiCr<sub>2</sub>S<sub>4</sub>-12 samples exhibited 59 and 117 mV dec<sup>-1</sup> Tafel slopes, respectively. Kinetic features were also supported by EIS measurements and NiCr<sub>2</sub>S<sub>4</sub>-12 yielded larger charge transfer resistance than the NiCr<sub>2</sub>S<sub>4</sub>-194 sample. The effect of the crystal structure on the OER performance of the cobalt-based sulfides was also studied. In this manner, the CoS sample, which is identical to the NiAs prototype with a hexagonal ordering (space group P63/mmc, no: 194) was compared to the Co<sub>9</sub>S<sub>8</sub> sample, which is identical to the NaCl prototype with a cubic structure (space group of Fm-3m, no: 225). CoS and Co<sub>9</sub>S<sub>8</sub> samples exhibited 364 mV and 381 mV OER overpotentials, respectively. CoS sample yielded the better OER activity and Tafel slope (46 mV dec<sup>-1</sup>) due to larger ECSA, RF, mass activity and TOF values compared to the Co<sub>9</sub>S<sub>8</sub> sample.

The effect of the crystallinity on the OER performance of the Ni, Cr and S containing samples was demonstrated in the following part. In this manner, the NiCr<sub>2</sub>S<sub>4</sub>-194 sample, which is identical to the NiAs prototype with a hexagonal ordering (space group P63/mmc, no: 194) was compared to the amorphous Ni-Cr-S sample. NiCr<sub>2</sub>S<sub>4</sub>-194 and Ni-Cr-S samples exhibited 354 mV and 329 mV OER overpotentials, respectively, showing remarkable differences in OER performances. The Ni-Cr-S sample yielded better OER activity than the crystalline sample.

Transition metal sulfides were also tested as electrodes for Li-battery systems. The summary of all experimental parameters and testing conditions of the samples as Li-battery electrodes was given in Table 4.29.

Table 4.29 Summary of the Li-battery electrode performances.

Sample	Electrolyte	Electrode		Current Density	Discharge Capacity
		Composition	Crystallinity		
Ni-Cr-S	LiPF <sub>6</sub>	80:10:10	Amorphous	50 mA g <sup>-1</sup>	344 mAh g <sup>-1</sup>
NiCr <sub>2</sub> S <sub>4</sub> -194	LiPF <sub>6</sub>	80:10:10	P63/mmc	50 mA g <sup>-1</sup>	793 mAh g <sup>-1</sup>
NiCr <sub>2</sub> S <sub>4</sub> -194	LiPF <sub>6</sub>	80:10:10	P63/mmc	50 mA g <sup>-1</sup>	794 mAh g <sup>-1</sup>
NiCr <sub>2</sub> S <sub>4</sub> -194	LiPF <sub>6</sub>	60:20:20	P63/mmc	50 mA g <sup>-1</sup>	815 mAh g <sup>-1</sup>
NiCr <sub>2</sub> S <sub>4</sub> -12	LiPF <sub>6</sub>	60:20:20	C2/m	50 mA g <sup>-1</sup>	764 mAh g <sup>-1</sup>
CoCr <sub>2</sub> S <sub>4</sub>	LiPF <sub>6</sub>	60:20:20	C2/m	50 mA g <sup>-1</sup>	954 mAh g <sup>-1</sup>
TiCr <sub>2</sub> S <sub>4</sub>	LiPF <sub>6</sub>	60:20:20	C2/m	50 mA g <sup>-1</sup>	879 mAh g <sup>-1</sup>

First, the effect of crystallinity was investigated and it was observed that the amorphous sample exhibited very poor performance compared to the crystalline sample. After that, the electrode composition (weight ratio of active material: carbon: binder) was changed from 8:1:1 to 6:2:2 and specific discharge capacity increased from 794 mAh g<sup>-1</sup> to 815 mAh g<sup>-1</sup>. Then, the effect of crystal structure on the performance was investigated. In this manner, hexagonal NiCr<sub>2</sub>S<sub>4</sub>-194 and monoclinic NiCr<sub>2</sub>S<sub>4</sub>-12 samples were tested under the same experimental and testing conditions. The hexagonal NiCr<sub>2</sub>S<sub>4</sub>-194 sample demonstrated better performance than the monoclinic NiCr<sub>2</sub>S<sub>4</sub>-12 sample. However, both samples yielded promising performances to be Li-ion battery electrodes. Finally, the effect of chemistry on the performance was investigated in monoclinic ACr<sub>2</sub>S<sub>4</sub> (where A= Ni, Co, Ti) systems. CoCr<sub>2</sub>S<sub>4</sub> sample exhibited the best performance (954 mAh g<sup>-1</sup>) among all samples investigated in this study, while the TiCr<sub>2</sub>S<sub>4</sub> sample exhibited the best cyclic stability and rate capability.

#### **4.6 Future Recommendations**

- Lithiated forms of the Li-battery electrodes may decrease the capacity losses during conversion reactions.
- In-situ phase analysis can be carried out to identify the reaction intermediates properly during conversion reactions in Li-battery systems.
- Effect of pH on the OER activity and kinetics of the electrocatalysts can be performed.



## CHAPTER 5

### CONCLUSIONS

In the scope of this study, Co-based and Ni-based metal sulfides were produced via a microwave-assisted synthesis route. The aim was to investigate the OER activities and Li-battery performances of the novel electrodes. Changing the experimental parameters (mole ratio, synthesis method and heat treatment temperature), single-phase metal sulfides and phase mixtures were formed.

The incorporation of chromium into the NiS structure provided an increase in electrochemically active surface area and the roughness factor. This increase improved the OER activity of the electrocatalysts by making the adsorption of ions easier and facilitating electron transfer. Moreover, the amount of Ni<sup>2+</sup> ions in the structure has increased with chromium. An increase in the amount of Ni<sup>2+</sup> ions has a positive effect on OER activity and kinetics in a way that an increase in the amount of Ni<sup>2+</sup> ions increases the chemical reaction rate providing faster kinetics. The presence of Cr atoms in NiS structure may create extra active sites for electrocatalysis as well as causes the reconstruction of electronic structure, which may result in the change in the charge and mass transport mechanisms.

Catalyst performance test for NiCr<sub>2</sub>S<sub>4</sub>-12, CoCr<sub>2</sub>S<sub>4</sub> and TiCr<sub>2</sub>S<sub>4</sub> samples exhibited 356 mV, 338 mV and 363 mV OER overpotentials, respectively. All three samples exhibited better OER activity than the benchmark RuO<sub>2</sub> with an overpotential value of 387 mV at 10 mA cm<sup>-2</sup> current density. The highest TOF value was achieved by the CoCr<sub>2</sub>S<sub>4</sub> sample, which supports the OER activity of this sample, meaning that the number of active catalytic sites is the largest for CoCr<sub>2</sub>S<sub>4</sub> among the other samples. The possible reasons for a large number of active catalytic sites can be the synergetic effect of larger ECSA and RF values together with the electrical conductivity.

The effect of different crystal structures on the OER performance was investigated in Ni-Based and Co-based sulfides. There is no significant effect of the crystal structure on the OER performance of the NiCr<sub>2</sub>S<sub>2</sub>-194 and the NiCr<sub>2</sub>S<sub>4</sub>-12 samples. Only kinetic features were affected by the crystal structure of the electrocatalysts. However, there are remarkable differences in OER performances of the Co-based electrocatalysts. CoS sample yielded a better OER activity (364 mV) than the Co<sub>9</sub>S<sub>8</sub> (381 mV) sample because of its larger number of active sites, ECSA value and RF value. Comparison of the OER performances of crystalline and amorphous forms of Ni, Cr and S containing samples showed that larger values of the ECSA and RF may be the dominating reason for the better performance of the Ni-Cr-S as compared to the crystalline NiCr<sub>2</sub>S<sub>4</sub>-194 sample.

The effect of crystal structure on the performance as a Li-ion battery electrode showed that the specific discharge capacity of the hexagonal NiCr<sub>2</sub>S<sub>4</sub>-194 sample was 51 mAh g<sup>-1</sup> larger than that of the NiCr<sub>2</sub>S<sub>4</sub>-12 sample which can be due to the smaller particle size as well as the more open structure allowing easier diffusion of Li-ions in the hexagonal structure. The chemistry effect on the Li-ion battery performance study showed that the first specific discharge capacities yielded 764 mAh g<sup>-1</sup>, 954 mAh g<sup>-1</sup> and 879 mAh g<sup>-1</sup> for the NiCr<sub>2</sub>S<sub>4</sub>-12, CoCr<sub>2</sub>S<sub>4</sub>, TiCr<sub>2</sub>S<sub>4</sub> electrodes, respectively. All samples, except the Ni-Cr-S sample (344 mAh g<sup>-1</sup>), exhibited a specific discharge capacity larger than 750 mAh g<sup>-1</sup>. These values were very close to their counterparts in the literature [213–215]. Therefore, transition metal sulfides investigated in this study are promising Li-ion battery anodes.

## REFERENCES

- [1] E.C. Gay, D.R. Vissers, F.J. Martino, K.E. Anderson, Performance Characteristics of Solid Lithium-Aluminum Alloy Electrodes, *J. Electrochem. Soc.* 123 (1976) 1591.
- [2] N. Nitta, F. Wu, J.T. Lee, G. Yushin, Li-ion battery materials: present and future, *Mater. Today*. 18 (2015) 252–264. <https://doi.org/https://doi.org/10.1016/j.mattod.2014.10.040>.
- [3] J. Zhao, Y. Zhang, Y. Wang, H. Li, Y. Peng, The application of nanostructured transition metal sulfides as anodes for lithium ion batteries, *J. Energy Chem.* 27 (2018) 1536–1554. <https://doi.org/https://doi.org/10.1016/j.jechem.2018.01.009>.
- [4] F.F.C. Bazito, R.M. Torresi, Cathodes for lithium ion batteries: the benefits of using nanostructured materials, *J. Braz. Chem. Soc.* 17 (2006) 627–642.
- [5] F. Wu, G. Yushin, Conversion cathodes for rechargeable lithium and lithium-ion batteries, *Energy Environ. Sci.* 10 (2017) 435–459.
- [6] X. Li, N. Fu, J. Zou, X. Zeng, Y. Chen, L. Zhou, W. Lu, H. Huang, Ultrafine cobalt sulfide nanoparticles encapsulated hierarchical N-doped carbon nanotubes for high-performance lithium storage, *Electrochim. Acta.* 225 (2017) 137–142.
- [7] F. Wu, J.T. Lee, F. Fan, N. Nitta, H. Kim, T. Zhu, G. Yushin, A Hierarchical Particle–Shell Architecture for Long-Term Cycle Stability of Li<sub>2</sub>S Cathodes, *Adv. Mater.* 27 (2015) 5579–5586.
- [8] L. Wei, E.H. Ang, Y. Yang, Y. Qin, Y. Zhang, M. Ye, Q. Liu, C.C. Li, Recent advances of transition metal based bifunctional electrocatalysts for rechargeable zinc-air batteries, *J. Power Sources.* 477 (2020) 228696.
- [9] W. Zhu, Z. Yue, W. Zhang, N. Hu, Z. Luo, M. Ren, Z. Xu, Z. Wei, Y. Suo, J.

- Wang, Wet-chemistry topotactic synthesis of bimetallic iron–nickel sulfide nanoarrays: an advanced and versatile catalyst for energy efficient overall water and urea electrolysis, *J. Mater. Chem. A*. 6 (2018) 4346–4353.
- [10] C. Han, W. Li, C. Shu, H. Guo, H. Liu, S. Dou, J. Wang, Catalytic activity boosting of nickel sulfide toward oxygen evolution reaction via confined overdoping engineering, *ACS Appl. Energy Mater.* 2 (2019) 5363–5372.
- [11] Y. Li, Y. Duan, K. Zhang, W. Yu, Efficient Anodic Chemical Conversion to Boost Hydrogen Evolution with Low Energy Consumption over Cobalt-doped Nickel Sulfide Electrocatalyst, *Chem. Eng. J.* (2022) 134472.
- [12] W. He, F. Wang, D. Jia, Y. Li, L. Liang, J. Zhang, Q. Hao, C. Liu, H. Liu, J. Zhao, Al-doped nickel sulfide nanosheet arrays as highly efficient bifunctional electrocatalysts for overall water splitting, *Nanoscale*. 12 (2020) 24244–24250.
- [13] Q. Liu, L. Xie, Z. Liu, G. Du, A.M. Asiri, X. Sun, A Zn-doped Ni<sub>3</sub>S<sub>2</sub> nanosheet array as a high-performance electrochemical water oxidation catalyst in alkaline solution, *Chem. Commun.* 53 (2017) 12446–12449.
- [14] J. Ding, S. Ji, H. Wang, H. Gai, F. Liu, V. Linkov, R. Wang, Mesoporous nickel-sulfide/nickel/N-doped carbon as HER and OER bifunctional electrocatalyst for water electrolysis, *Int. J. Hydrogen Energy*. 44 (2019) 2832–2840.
- [15] Q. Hao, S. Li, H. Liu, J. Mao, Y. Li, C. Liu, J. Zhang, C. Tang, Dual tuning of nickel sulfide nanoflake array electrocatalyst through nitrogen doping and carbon coating for efficient and stable water splitting, *Catal. Sci. Technol.* 9 (2019) 3099–3108.
- [16] W. He, L. Han, Q. Hao, X. Zheng, Y. Li, J. Zhang, C. Liu, H. Liu, H.L. Xin, Fluorine-anion-modulated electron structure of nickel sulfide nanosheet arrays for alkaline hydrogen evolution, *ACS Energy Lett.* 4 (2019) 2905–2912.

- [17] Z. Zhang, T. Zhang, J.Y. Lee, Electrochemical Performance of Borate-Doped Nickel Sulfide: Enhancement of the Bifunctional Activity for Total Water Splitting, *ChemElectroChem*. 6 (2019) 1443–1449.
- [18] J.-J. Duan, Z. Han, R.-L. Zhang, J.-J. Feng, L. Zhang, Q.-L. Zhang, A.-J. Wang, Iron, manganese co-doped Ni<sub>3</sub>S<sub>2</sub> nanoflowers in situ assembled by ultrathin nanosheets as a robust electrocatalyst for oxygen evolution reaction, *J. Colloid Interface Sci.* 588 (2021) 248–256.
- [19] J.-F. Qin, M. Yang, S. Hou, B. Dong, T.-S. Chen, X. Ma, J.-Y. Xie, Y.-N. Zhou, J. Nan, Y.-M. Chai, Copper and cobalt co-doped Ni<sub>3</sub>S<sub>2</sub> grown on nickel foam for highly efficient oxygen evolution reaction, *Appl. Surf. Sci.* 502 (2020) 144172.
- [20] H. Mukaibo, A. Yoshizawa, T. Momma, T. Osaka, Particle size and performance of SnS<sub>2</sub> anodes for rechargeable lithium batteries, *J. Power Sources*. 119 (2003) 60–63.
- [21] C.-H. Lai, K.-W. Huang, J.-H. Cheng, C.-Y. Lee, W.-F. Lee, C.-T. Huang, B.-J. Hwang, L.-J. Chen, Oriented growth of large-scale nickel sulfide nanowire arrays via a general solution route for lithium-ion battery cathode applications, *J. Mater. Chem.* 19 (2009) 7277–7283.
- [22] S. Xiao, X. Li, W. Sun, B. Guan, Y. Wang, General and facile synthesis of metal sulfide nanostructures: In situ microwave synthesis and application as binder-free cathode for Li-ion batteries, *Chem. Eng. J.* 306 (2016) 251–259.
- [23] Y. Wang, J. Wu, Y. Tang, X. Lü, C. Yang, M. Qin, F. Huang, X. Li, X. Zhang, Phase-controlled synthesis of cobalt sulfides for lithium ion batteries, *ACS Appl. Mater. Interfaces*. 4 (2012) 4246–4250.
- [24] X. Zhu, Z. Wen, Z. Gu, S. Huang, Room-temperature mechanosynthesis of Ni<sub>3</sub>S<sub>2</sub> as cathode material for rechargeable lithium polymer batteries, *J. Electrochem. Soc.* 153 (2006) A504.

- [25] D.K. Nandi, S. Sahoo, S. Sinha, S. Yeo, H. Kim, R.N. Bulakhe, J. Heo, J.-J. Shim, S.-H. Kim, Highly uniform atomic layer-deposited MoS<sub>2</sub>@ 3D-Ni-foam: A novel approach to prepare an electrode for supercapacitors, *ACS Appl. Mater. Interfaces*. 9 (2017) 40252–40264.
- [26] R. Souleyman, Z. Wang, C. Qiao, M. Naveed, C. Cao, Microwave-assisted synthesis of graphene-like cobalt sulfide freestanding sheets as an efficient bifunctional electrocatalyst for overall water splitting, *J. Mater. Chem. A*. 6 (2018) 7592–7607.
- [27] J. Li, P.K. Shen, Z. Tian, One-step synthesis of Ni<sub>3</sub>S<sub>2</sub> nanowires at low temperature as efficient electrocatalyst for hydrogen evolution reaction, *Int. J. Hydrogen Energy*. 42 (2017) 7136–7142.
- [28] S. Leidich, D. Buechele, R. Lauenstein, M. Kluncker, C. Lind, “Non-hydrolytic” sol–gel synthesis of molybdenum sulfides, *J. Solid State Chem*. 242 (2016) 175–181.
- [29] H.R. Rajabi, F. Karimi, H. Kazemdehdashti, L. Kavoshi, Fast sonochemically-assisted synthesis of pure and doped zinc sulfide quantum dots and their applicability in organic dye removal from aqueous media, *J. Photochem. Photobiol. B Biol*. 181 (2018) 98–105.
- [30] X. Hu, S. Liu, Y. Chen, J. Jiang, Y. Sun, L. Wang, S. Han, H. Lin, One-step electrodeposition fabrication of iron cobalt sulfide nanosheet arrays on Ni foam for high-performance asymmetric supercapacitors, *Ionics (Kiel)*. (2020) 1–12.
- [31] C. Zhang, X. Cai, Y. Qian, H. Jiang, L. Zhou, B. Li, L. Lai, Z. Shen, W. Huang, Electrochemically synthesis of nickel cobalt sulfide for high-performance flexible asymmetric supercapacitors, *Adv. Sci*. 5 (2018) 1700375.
- [32] T. Edamura, J. Muto, Electrodeposition of zinc cadmium sulphide thin films from acidic aqueous electrolyte solution at room temperature, *J. Mater. Sci*.

Lett. 14 (1995) 889–891.

- [33] M. Lacroix, M. Vrinat, M. Breyse, Unsupported nickel tungsten sulfide catalysts: Part 1: Catalytic behaviour in hydrogenation and hydrodesulfurization reactions., *Appl. Catal.* 21 (1986) 73–83. [https://doi.org/https://doi.org/10.1016/S0166-9834\(00\)81329-9](https://doi.org/https://doi.org/10.1016/S0166-9834(00)81329-9).
- [34] A. Wustrow, B. Key, P.J. Phillips, N. Sa, A.S. Lipton, R.F. Klie, J.T. Vaughey, K.R. Poeppelmeier, Synthesis and Characterization of MgCr<sub>2</sub>S<sub>4</sub> Thiospinel as a Potential Magnesium Cathode, *Inorg. Chem.* 57 (2018) 8634–8638. <https://doi.org/10.1021/acs.inorgchem.8b01417>.
- [35] P. Bonnick, L. Blanc, S.H. Vajargah, C.-W. Lee, X. Sun, M. Balasubramanian, L.F. Nazar, Insights into Mg<sup>2+</sup> Intercalation in a Zero-Strain Material: Thiospinel Mg<sub>x</sub>Zr<sub>2</sub>S<sub>4</sub>, *Chem. Mater.* 30 (2018) 4683–4693. <https://doi.org/10.1021/acs.chemmater.8b01345>.
- [36] X. Sun, P. Bonnick, V. Duffort, M. Liu, Z. Rong, K.A. Persson, G. Ceder, L.F. Nazar, A high capacity thiospinel cathode for Mg batteries, *Energy Environ. Sci.* 9 (2016) 2273–2277. <https://doi.org/10.1039/C6EE00724D>.
- [37] L. Caggiu, S. Enzo, L. Stievano, R. Berthelot, C. Gerbaldi, M. Falco, S. Garroni, G. Mulas, Solvent-Free Mechanochemical Approach towards Thiospinel MgCr<sub>2</sub>S<sub>4</sub> as a Potential Electrode for Post-Lithium Ion Batteries, *Batteries.* 6 (2020) 43.
- [38] W. Chen, P. Yuan, S. Guo, S. Gao, J. Wang, M. Li, F. Liu, J. Wang, J.P. Cheng, Formation of mixed metal sulfides of Ni<sub>x</sub>Cu<sub>1-x</sub>Co<sub>2</sub>S<sub>4</sub> for high-performance supercapacitors, *J. Electroanal. Chem.* 836 (2019) 134–142.
- [39] T. Ma, J. Chen, M. Chen, S. Liu, J. Luo, H. Zou, W. Yang, S. Chen, Nickel-cobalt-molybdenum sulfides with adjustable morphology via coprecipitation and hydrothermal conversion as high-performance electrodes for asymmetric supercapacitors, *J. Alloys Compd.* 838 (2020) 155631. <https://doi.org/https://doi.org/10.1016/j.jallcom.2020.155631>.

- [40] C. Gervas, M.D. Khan, C. Zhang, C. Zhao, R.K. Gupta, E. Carleschi, B.P. Doyle, N. Revaprasadu, Effect of cationic disorder on the energy generation and energy storage applications of  $\text{Ni}_x\text{Co}_{3-x}\text{S}_4$  thiospinel, *RSC Adv.* 8 (2018) 24049–24058. <https://doi.org/10.1039/C8RA03522A>.
- [41] P. Ganesan, A. Sivanantham, S. Shanmugam, Inexpensive electrochemical synthesis of nickel iron sulphides on nickel foam: super active and ultra-durable electrocatalysts for alkaline electrolyte membrane water electrolysis, *J. Mater. Chem. A.* 4 (2016) 16394–16402.
- [42] G. Fu, J. Wang, Y. Chen, Y. Liu, Y. Tang, J.B. Goodenough, J.-M. Lee, Exploring Indium-Based Ternary Thiospinel as Conceivable High-Potential Air-Cathode for Rechargeable Zn–Air Batteries, *Adv. Energy Mater.* 8 (2018) 1802263. <https://doi.org/https://doi.org/10.1002/aenm.201802263>.
- [43] R. Krishnapriya, S. Praneetha, A.M. Rabel, A. Vadivel Murugan, Energy efficient, one-step microwave-solvothermal synthesis of a highly electrocatalytic thiospinel  $\text{NiCo}_2\text{S}_4$ /graphene nanohybrid as a novel sustainable counter electrode material for Pt-free dye-sensitized solar cells, *J. Mater. Chem. C.* 5 (2017) 3146–3155. <https://doi.org/10.1039/C6TC04619C>.
- [44] S.Y. Khoo, J. Miao, H. Bin Yang, Z. He, K.C. Leong, B. Liu, T.T.Y. Tan, One-Step Hydrothermal Tailoring of  $\text{NiCo}_2\text{S}_4$  Nanostructures on Conducting Oxide Substrates as an Efficient Counter Electrode in Dye-Sensitized Solar Cells, *Adv. Mater. Interfaces.* 2 (2015) 1500384.
- [45] S. Sahoo, R. Mondal, D.J. Late, C.S. Rout, Electrodeposited nickel cobalt manganese based mixed sulfide nanosheets for high performance supercapacitor application, *Microporous Mesoporous Mater.* 244 (2017) 101–108.
- [46] T. Wei, C. Chen, H. Chien, S. Lu, C. Hu, A cost-effective supercapacitor material of ultrahigh specific capacitances: spinel nickel cobaltite aerogels from an epoxide-driven sol–gel process, *Adv. Mater.* 22 (2010) 347–351.

- [47] J. Xiao, L. Wan, S. Yang, F. Xiao, S. Wang, Design Hierarchical Electrodes with Highly Conductive NiCo<sub>2</sub>S<sub>4</sub> Nanotube Arrays Grown on Carbon Fiber Paper for High-Performance Pseudocapacitors, *Nano Lett.* 14 (2014) 831–838. <https://doi.org/10.1021/nl404199v>.
- [48] A.B. Anderson, S.Y. Hong, J.L. Smialek, Comparison of bonding in first transition-metal series: diatomic and bulk sulfides and oxides, *J. Phys. Chem.* 91 (1987) 4250–4254.
- [49] A. Jain, S.P. Ong, G. Hautier, W. Chen, W.D. Richards, S. Dacek, S. Cholia, D. Gunter, D. Skinner, G. Ceder, Commentary: The Materials Project: A materials genome approach to accelerating materials innovation, *APL Mater.* 1 (2013) 11002.
- [50] M. Damm, T.N. Glasnov, C.O. Kappe, Translating high-temperature microwave chemistry to scalable continuous flow processes, *Org. Process Res. Dev.* 14 (2010) 215–224.
- [51] R. Zhang, C.X. Lu, Z.L. Shi, T. Liu, T.F. Zhai, W. Zhou, Hexagonal phase NiS octahedrons co-modified by 0D-, 1D-, and 2D carbon materials for high-performance supercapacitor, *Electrochim. Acta.* 311 (2019) 83–91. <https://doi.org/10.1016/j.electacta.2019.04.111>.
- [52] L.B. Ma, X.P. Shen, Z.Y. Ji, S. Wang, H. Zhou, G.X. Zhu, Carbon coated nickel sulfide/reduced graphene oxide nanocomposites: facile synthesis and excellent supercapacitor performance, *Electrochim. Acta.* 146 (2014) 525–532. <https://doi.org/10.1016/j.electacta.2014.09.087>.
- [53] X.J. Yang, L.J. Zhao, J.S. Lian, Arrays of hierarchical nickel sulfides/MoS<sub>2</sub> nanosheets supported on carbon nanotubes backbone as advanced anode materials for asymmetric supercapacitor, *J. Power Sources.* 343 (2017) 373–382. <https://doi.org/10.1016/j.jpowsour.2017.01.078>.
- [54] H. Geng, S.F. Kong, Y. Wang, NiS nanorod-assembled nanoflowers grown on graphene: morphology evolution and Li-ion storage applications, *J. Mater.*

Chem. A. 2 (2014) 15152–15158. <https://doi.org/10.1039/c4ta03440f>.

- [55] H.B. Ren, J.H. Wang, Y.X. Cao, W. Luo, Y.F. Sun, Nickel sulfide nanoparticle anchored reduced graphene oxide with improved lithium storage properties, *Mater. Res. Bull.* 133 (2021). <https://doi.org/10.1016/j.materresbull.2020.111047>.
- [56] Y.R. Zhang, F. Lu, L. Pan, Y. Xu, Y.J. Yang, Y. Bando, D. Golberg, J.N. Yao, X. Wang, Improved cycling stability of NiS<sub>2</sub> cathodes through designing a “kiwano” hollow structure, *J. Mater. Chem. A* 6 (2018) 11978–11984. <https://doi.org/10.1039/c8ta01551a>.
- [57] M.B. Ma, G. Yang, H.J. Wang, Y. Lu, B.W. Zhang, X. Cao, D.D. Peng, X.F. Du, Y.H. Liu, Y.Z. Huang, Ordered distributed nickel sulfide nanoparticles across graphite nanosheets for efficient oxygen evolution reaction electrocatalyst, *Int. J. Hydrogen Energy* 44 (2019) 1544–1554. <https://doi.org/10.1016/j.ijhydene.2018.11.176>.
- [58] S. Shit, S. Chhetri, W. Fang, N.C. Murmu, H. Koo, P. Samanta, T. Kuila, Cobalt Sulfide/Nickel Sulfide Heterostructure Directly Grown on Nickel Foam: An Efficient and Durable Electrocatalyst for Overall Water Splitting Application, *ACS Appl. Mater. Interfaces* 10 (2018) 27712–27722. <https://doi.org/10.1021/acsami.8b04223>.
- [59] M. Lee, H.-S. Oh, M.K. Cho, J.-P. Ahn, Y.J. Hwang, B.K. Min, Activation of a Ni electrocatalyst through spontaneous transformation of nickel sulfide to nickel hydroxide in an oxygen evolution reaction, *Appl. Catal. B Environ.* 233 (2018) 130–135. <https://doi.org/https://doi.org/10.1016/j.apcatb.2018.03.083>.
- [60] A.P. Tiwari, Y. Yoon, T.G. Novak, K.S. An, S. Jeon, Continuous Network of Phase-Tuned Nickel Sulfide Nanostructures for Electrocatalytic Water Splitting, *ACS Appl. NANO Mater.* 2 (2019) 5061–5070. <https://doi.org/10.1021/acsanm.9b00985>.
- [61] M. Muniyappa, S.N. Kalegowda, M. Shetty, J.B. Sriramoju, M. Shastri,

- S.V.N. Rao, D. De, M. V Shankar, D. Rangappa, Cocatalyst free nickel sulphide nanostructure for enhanced photocatalytic hydrogen evolution, *Int. J. Hydrogen Energy*. 47 (2022) 5307–5318. <https://doi.org/10.1016/j.ijhydene.2021.11.171>.
- [62] M. Khosravi, S. Saeednia, P. Iranmanesh, M.H. Ardakani, Cauliflower-like Nickel Sulfide Nanostructures: Preparation, Optical Properties, Catalytic and Photocatalytic Activities, *J. Clust. Sci.* (n.d.). <https://doi.org/10.1007/s10876-021-02210-5>.
- [63] A.W. Peters, Z.Y. Li, O.K. Farha, J.T. Hupp, Toward Inexpensive Photocatalytic Hydrogen Evolution: A Nickel Sulfide Catalyst Supported on a High-Stability Metal-Organic Framework, *ACS Appl. Mater. Interfaces*. 8 (2016) 20675–20681. <https://doi.org/10.1021/acsami.6b04729>.
- [64] H.S. Fan, H. Yu, X.L. Wu, Y. Zhang, Z.Z. Luo, H.W. Wang, Y.Y. Guo, S. Madhavi, Q.Y. Yan, Controllable Preparation of Square Nickel Chalcogenide (NiS and NiSe<sub>2</sub>) Nanoplates for Superior Li/Na Ion Storage Properties, *ACS Appl. Mater. Interfaces*. 8 (2016) 25261–25267. <https://doi.org/10.1021/acsami.6b07300>.
- [65] M.K. Sadan, M. Jeon, J. Yun, E. Song, K.K. Cho, J.H. Ahn, H.J. Ahn, Excellent Electrochemical Performance of a Mesoporous Nickel Sulfide Anode for Na/K-Ion Batteries, *ACS Appl. ENERGY Mater.* 4 (2021) 14537–14545. <https://doi.org/10.1021/acsaem.1c03192>.
- [66] Q.Q. Yao, J.S. Zhang, J.X. Li, W.J. Huang, K. Hou, Y. Zhao, L.H. Guan, Yolk-shell NiS<sub>x</sub>@C nanosheets as K-ion battery anodes with high rate capability and ultralong cycle life, *J. Mater. Chem. A*. 7 (2019) 18932–18939. <https://doi.org/10.1039/c9ta06292k>.
- [67] Y. Liu, S.J. Guo, W. Zhang, W. Kong, Z.D. Wang, W.J. Yan, H.L. Fan, X.G. Hao, G.Q. Guan, Three-dimensional interconnected cobalt sulfide foam: Controllable synthesis and application in supercapacitor, *Electrochim. Acta*.

317 (2019) 551–561. <https://doi.org/10.1016/j.electacta.2019.05.121>.

- [68] J.W. Cheng, L.Y. Lin, W.L. Hong, L.Y. Lin, H.Q. Chen, H.X. Lai, Rational design of nickel cobalt sulfide/cobalt sulfide sheet-on-sheet structure for asymmetric supercapacitors, *Electrochim. Acta.* 283 (2018) 1245–1252. <https://doi.org/10.1016/j.electacta.2018.07.059>.
- [69] Y.S. Zhou, J. Jin, X.R. Zhou, F. Liu, P. Zhou, Y.C. Zhu, B.S. Xu, Cobalt sulfide @ CNT-CNF for high-performance asymmetric supercapacitor, *Ionics (Kiel)*. 25 (2019) 4031–4035. <https://doi.org/10.1007/s11581-019-03085-3>.
- [70] Y.A. Kumar, S.S. Rao, D. Punnoose, C. V Tulasivarma, C. Gopi, K. Prabakar, H.J. Kim, Influence of solvents in the preparation of cobalt sulfide for supercapacitors, *R. Soc. OPEN Sci.* 4 (2017). <https://doi.org/10.1098/rsos.170427>.
- [71] H.C. Lu, Q.B. Guo, Q. Fan, L. Xue, X.Y. Lu, F. Zan, H. Xia, Cobalt sulfide quantum dot embedded in nitrogen/sulfur-doped carbon nanosheets as a polysulfide barrier in Li-S batteries, *J. Alloys Compd.* 870 (2021). <https://doi.org/10.1016/j.jallcom.2021.159341>.
- [72] H.L. Chen, P.S. Wu, J.J. Wu, Binder-Free Metal Sulfide Composite Nanosheet Array Electrodes for Li-Ion Batteries, *ACS Sustain. Chem. Eng.* 7 (2019) 17100–17106. <https://doi.org/10.1021/acssuschemeng.9b03329>.
- [73] M.M. Lao, G.Q. Zhao, X. Li, Y.P. Chen, S.X. Dou, W.P. Sun, Homogeneous Sulfur-Cobalt Sulfide Nanocomposites as Lithium-Sulfur Battery Cathodes with Enhanced Reaction Kinetics, *ACS Appl. ENERGY Mater.* 1 (2018) 167–172. <https://doi.org/10.1021/acsaem.7b00049>.
- [74] Y.S. Zhou, Y.C. Zhu, B.S. Xu, X.J. Zhang, K.A. Al-Ghanim, S. Mahboob, Cobalt Sulfide Confined in N-Doped Porous Branched Carbon Nanotubes for Lithium-Ion Batteries, *NANO-MICRO Lett.* 11 (2019). <https://doi.org/10.1007/s40820-019-0259-z>.

- [75] X.Y. Zhang, B. Li, M.Q. Lan, S.X. Yang, Q.R. Xie, J.W. Xiao, F. Xiao, S. Wang, Cation Modulation of Cobalt Sulfide Supported by Mesopore-Rich Hydrangea-Like Carbon Nanoflower for Oxygen Electrocatalysis, *ACS Appl. Mater. Interfaces.* 13 (2021) 18683–18692. <https://doi.org/10.1021/acsami.1c00579>.
- [76] C.Y. Xie, Q.J. Wang, C. Xiao, L.T. Yang, M.Q. Lan, S.X. Yang, J.W. Xiao, F. Xiao, S. Wang, Two-dimensional metal-organic framework-derived selenium-doped cobalt Sulfide@Graphene nanofoam for oxygen electrocatalysis, *Carbon N. Y.* 178 (2021) 640–648. <https://doi.org/10.1016/j.carbon.2021.03.054>.
- [77] T.T. Liu, Y.H. Liang, Q. Liu, X.P. Sun, Y.Q. He, A.M. Asiri, Electrodeposition of cobalt-sulfide nanosheets film as an efficient electrocatalyst for oxygen evolution reaction, *Electrochem. Commun.* 60 (2015) 92–96. <https://doi.org/10.1016/j.elecom.2015.08.011>.
- [78] F. Zhang, H.Q. Zhuang, J. Song, Y.L. Men, Y.X. Pan, S.H. Yu, Coupling cobalt sulfide nanosheets with cadmium sulfide nanoparticles for highly efficient visible-light-driven photocatalysis, *Appl. Catal. B-ENVIRONMENTAL.* 226 (2018) 103–110. <https://doi.org/10.1016/j.apcatb.2017.12.046>.
- [79] A.A. Khan, S. Kumari, A. Chowdhury, S. Hussain, Phase Tuned Originated Dual Properties of Cobalt Sulfide Nanostructures as Photocatalyst and Adsorbent for Removal of Dye Pollutants, *ACS Appl. NANO Mater.* 1 (2018) 3474–3485. <https://doi.org/10.1021/acsanm.8b00656>.
- [80] M. Zhou, L. Li, S. Zhang, J.J. Yi, Y.H. Song, H.M. Li, H. Xu, Surface Engineering of 2D Carbon Nitride with Cobalt Sulfide Cocatalyst for Enhanced Photocatalytic Hydrogen Evolution, *Phys. STATUS SOLIDI A-APPLICATIONS Mater. Sci.* 218 (2021). <https://doi.org/10.1002/pssa.202100012>.

- [81] Q.Y. Yu, J. Hu, C. Qian, Y.Z. Gao, W. Wang, G.P. Yin, CoS/N-doped carbon core/shell nanocrystals as an anode material for potassium-ion storage, *J. SOLID STATE Electrochem.* 23 (2019) 27–32. <https://doi.org/10.1007/s10008-018-4081-1>.
- [82] H.S. Wang, J.L. Liu, H.H. Wang, X.Y. Cai, X.L. Ye, L.L. Zhang, Z. Chen, Z.X. Shen, Cobalt sulfide nanoflakes grown on graphite foam for Na-ion batteries with ultrahigh initial coulombic efficiency, *J. Mater. Chem. A.* 8 (2020) 14900–14907. <https://doi.org/10.1039/d0ta04312e>.
- [83] J. Hu, B. Wang, Q.Y. Yu, Y.H. Zhang, D. Zhang, Y. Li, W. Wang, Amorphous cobalt sulfide/N-doped carbon core/shell nanoparticles as an anode material for potassium-ion storage, *J. Mater. Sci.* 55 (2020) 15213–15221. <https://doi.org/10.1007/s10853-020-04886-y>.
- [84] Y. Kim, K.S. Park, S.H. Song, J.T. Han, J.B. Goodenough, Access to  $M^{3+}/M^{2+}$  Redox Couples in Layered  $LiMS_2$  Sulfides ( $M=Ti, V, Cr$ ) as Anodes for Li-Ion Battery, *J. Electrochem. Soc.* 156 (2009) A703–A708. <https://doi.org/10.1149/1.3151856>.
- [85] M.X. Su, W.D. Zhou, Z.Z. Jiang, M.Y. Chen, X.F. Luo, J. He, C.L. Yuan, Elimination of Interlayer Potential Barriers of Chromium Sulfide by Self-Intercalation for Enhanced Hydrogen Evolution Reaction, *ACS Appl. Mater. Interfaces.* 13 (2021) 13055–13062. <https://doi.org/10.1021/acsami.0c20577>.
- [86] H. Pan, H.X. Xie, G. Chen, N.B. Xu, M.M. Wang, A. Fakhri,  $Cr_2S_3-Co_3O_4$  on polyethylene glycol-chitosan nanocomposites with enhanced ultraviolet light photocatalysis activity, antibacterial and antioxidant studies, *Int. J. Biol. Macromol.* 148 (2020) 608–614. <https://doi.org/10.1016/j.ijbiomac.2019.12.262>.
- [87] Z. Shadike, Y.N. Zhou, L.L. Chen, Q. Wu, J.L. Yue, N. Zhang, X.Q. Yang, L. Gu, X.S. Liu, S.Q. Shi, Z.W. Fu, Antisite occupation induced single anionic redox chemistry and structural stabilization of layered sodium chromium

- sulfide, *Nat. Commun.* 8 (2017). <https://doi.org/10.1038/s41467-017-00677-3>.
- [88] M.S. Javed, S.G. Dai, M.J. Wang, D.L. Guo, L. Chen, X. Wang, C.U. Hu, Y. Xi, High performance solid state flexible supercapacitor based on molybdenum sulfide hierarchical nanospheres, *J. Power Sources.* 285 (2015) 63–69. <https://doi.org/10.1016/j.jpowsour.2015.03.079>.
- [89] M.X. Shang, C.C. Du, H. Huang, J.X. Mao, P. Liu, W.B. Song, Direct electrochemical growth of amorphous molybdenum sulfide nanosheets on Ni foam for high-performance supercapacitors, *J. Colloid Interface Sci.* 532 (2018) 24–31. <https://doi.org/10.1016/j.jcis.2018.07.127>.
- [90] I.T. Bello, O. Oladipo, O. Adedokun, S.M. Dhlamini, Recent advances on the preparation and electrochemical analysis of MoS<sub>2</sub>-based materials for supercapacitor applications: A mini-review, *Mater. TODAY Commun.* 25 (2020). <https://doi.org/10.1016/j.mtcomm.2020.101664>.
- [91] Y. Zhou, Y. Liu, W.X. Zhao, F.Y. Xie, R.M. Xu, B.J. Li, X. Zhou, H. Shen, Growth of vertically aligned MoS<sub>2</sub> nanosheets on a Ti substrate through a self-supported bonding interface for high-performance lithium-ion batteries: a general approach, *J. Mater. Chem. A.* 4 (2016) 5932–5941. <https://doi.org/10.1039/c6ta01116k>.
- [92] S. Ji, S.K. Kim, W. Song, Y. Yoon, S. Myung, J. Lim, H.K. Jung, S. Choi, K.S. An, S.S. Lee, Extraordinary lithium storage capacity and lithiation mechanism of partially amorphous molybdenum sulfide on chemically exfoliated graphene, *Electrochim. Acta.* 354 (2020).
- [93] T. Ding, Increasing the electrochemical activity performance by employing molybdenum sulfide as barrier for soluble polysulfide in Li-S batteries, *Ionics (Kiel)*. 28 (2022) 1183–1187. <https://doi.org/10.1007/s11581-021-04395-1>.
- [94] Y.P. Sun, Synthesis and electrochemical performance of C@molybdenum sulfide composite for high-performance lithium-ion batteries, *Ionics (Kiel)*.

(n.d.). <https://doi.org/10.1007/s11581-022-04483-w>.

- [95] M.Y. Tang, Y.Y. Wang, H. Shen, G.B. Che, Solution-Based Preparation Techniques for Two-Dimensional Molybdenum Sulfide Nanosheet and Application of Its Composite Materials in Photocatalysis and Electrocatalysis, *Prog. Chem.* 30 (2018) 1646–1659. <https://doi.org/10.7536/PC180109>.
- [96] Y. Xu, C. Zheng, S.B. Wang, Y.D. Hou, 3D arrays of molybdenum sulphide nanosheets on Mo meshes: Efficient electrocatalysts for hydrogen evolution reaction, *Electrochim. Acta.* 174 (2015) 653–659. <https://doi.org/10.1016/j.electacta.2015.06.040>.
- [97] T. Daeneke, N. Dahr, P. Atkin, R.M. Clark, C.J. Harrison, R. Brkljaca, N. Pillai, B.Y. Zhang, A. Zavabeti, S.J. Ippolito, K.J. Borean, J.Z. Ou, M.S. Strano, K. Kalantar-zadeh, Surface Water Dependent Properties of Sulfur-Rich Molybdenum Sulfides: Electrolyteless Gas Phase Water Splitting, *ACS Nano.* 11 (2017) 6782–6794. <https://doi.org/10.1021/acsnano.7b01632>.
- [98] Z.B. Li, P. Liu, G.W. Yang, Efficient All-2D Amorphous Cobalt Sulfide Nanosheets/Multilayered Molybdenum Disulfide Hybrid Heterojunction Catalyst for Electrochemical Hydrogen Evolution, *Glob. CHALLENGES.* 4 (2020). <https://doi.org/10.1002/gch2.201900066>.
- [99] H.L. Zhou, Y.C. Liu, L. Zhang, H.D. Li, H. Liu, W.J. Li, Transition metal-doped amorphous molybdenum sulfide/graphene ternary cocatalysts for excellent photocatalytic hydrogen evolution: Synergistic effect of transition metal and graphene, *J. Colloid Interface Sci.* 533 (2019) 287–296. <https://doi.org/10.1016/j.jcis.2018.07.084>.
- [100] X.X. Jiang, M. Fuji, In-Situ Photodeposition of Highly Dispersed MoS<sub>x</sub> as a Co-catalyst on TiO<sub>2</sub> Nanoparticles for Efficient and Stable Photocatalytic H<sub>2</sub> Evolution, *Catal. Letters.* (n.d.). <https://doi.org/10.1007/s10562-021-03807-1>.
- [101] Y. Jiang, Y.C. Wang, J.F. Ni, L. Li, Molybdenum-based materials for sodium-

- ion batteries, *INFOMAT.* 3 (2021) 339–352.  
<https://doi.org/10.1002/inf2.12175>.
- [102] Y.X. Huang, Z.H. Wang, M.R. Guan, F. Wu, R.J. Chen, Toward Rapid-Charging Sodium-Ion Batteries using Hybrid-Phase Molybdenum Sulfide Selenide-Based Anodes, *Adv. Mater.* 32 (2020).  
<https://doi.org/10.1002/adma.202003534>.
- [103] S. Wang, J.G. Tu, Y. Yuan, R. Ma, S.Q. Jiao, Sodium modified molybdenum sulfide via molten salt electrolysis as an anode material for high performance sodium-ion batteries, *Phys. Chem. Chem. Phys.* 18 (2016) 3204–3213.  
<https://doi.org/10.1039/c5cp07007d>.
- [104] J. Zhu, S. Tang, J. Wu, X. Shi, B. Zhu, X. Meng, Wearable high-performance supercapacitors based on silver-sputtered textiles with FeCo<sub>2</sub>S<sub>4</sub>–NiCo<sub>2</sub>S<sub>4</sub> composite nanotube-built multitripod architectures as advanced flexible electrodes, *Adv. Energy Mater.* 7 (2017) 1601234.
- [105] J. Tang, W. Huang, X. Lv, Q. Shi, Improved chemical precipitation prepared rapidly NiCo<sub>2</sub>S<sub>4</sub> with high specific capacitance for supercapacitors, *Nanotechnology.* 32 (2020) 85604.
- [106] R.D. Shannon, Revised effective ionic radii and systematic studies of interatomic distances in halides and chalcogenides, *Acta Crystallogr. Sect. A Cryst. Physics, Diffraction, Theor. Gen. Crystallogr.* 32 (1976) 751–767.
- [107] C. Liu, X. Wu, B. Wang, Performance modulation of energy storage devices: a case of Ni-Co-S electrode materials, *Chem. Eng. J.* 392 (2020) 123651.
- [108] T.-F. Yi, J.-J. Pan, T.-T. Wei, Y. Li, G. Cao, NiCo<sub>2</sub>S<sub>4</sub>-based nanocomposites for energy storage in supercapacitors and batteries, *Nano Today.* 33 (2020) 100894.
- [109] H. Zhang, G. Liu, J. Li, H. Cui, Y. Liu, M. Wang, Trapping and catalytic conversion of polysulfides by kirkendall effect built hollow NiCo<sub>2</sub>S<sub>4</sub> nano-

- prisms for advanced sulfur cathodes in Li–S battery, *J. Mater. Sci.* 56 (2021) 4328–4340.
- [110] S. Li, P. Xu, M.K. Aslam, C. Chen, A. Rashid, G. Wang, L. Zhang, B. Mao, Propelling polysulfide conversion for high-loading lithium–sulfur batteries through highly sulfiphilic NiCo<sub>2</sub>S<sub>4</sub> nanotubes, *Energy Storage Mater.* 27 (2020) 51–60.
- [111] G. Janani, S. Yuvaraj, S. Surendran, Y. Chae, Y. Sim, S.-J. Song, W. Park, M.-J. Kim, U. Sim, Enhanced bifunctional electrocatalytic activity of Ni-Co bimetallic chalcogenides for efficient water-splitting application, *J. Alloys Compd.* 846 (2020) 156389.
- [112] J.-Z. He, W.-J. Niu, Y.-P. Wang, Q.-Q. Sun, M.-J. Liu, K. Wang, W.-W. Liu, M.-C. Liu, F.-C. Yu, Y.-L. Chueh, In-situ synthesis of hybrid nickel cobalt sulfide/carbon nitrogen nanosheet composites as highly efficient bifunctional oxygen electrocatalyst for rechargeable Zn-air batteries, *Electrochim. Acta.* 362 (2020) 136968.
- [113] X. Li, Z. Kou, S. Xi, W. Zang, T. Yang, L. Zhang, J. Wang, Porous NiCo<sub>2</sub>S<sub>4</sub>/FeOOH nanowire arrays with rich sulfide/hydroxide interfaces enable high OER activity, *Nano Energy.* 78 (2020) 105230.
- [114] Y. Xu, A. Sumboja, A. Groves, T. Ashton, Y. Zong, J.A. Darr, Enhancing bifunctional catalytic activity of cobalt–nickel sulfide spinel nanocatalysts through transition metal doping and its application in secondary zinc–air batteries, *RSC Adv.* 10 (2020) 41871–41882.
- [115] S. Zhao, J. Xu, M. Mao, L. Li, X. Li, NiCo<sub>2</sub>S<sub>4</sub>@ Zn<sub>0.5</sub>Cd<sub>0.5</sub>S with direct Z-scheme heterojunction constructed by band structure adjustment of Zn<sub>x</sub>Cd<sub>1-x</sub>S for efficient photocatalytic H<sub>2</sub> evolution, *Appl. Surf. Sci.* 528 (2020) 147016.
- [116] S. Sarawutanukul, C. Tomon, S. Duangdangchote, N. Phattharasupakun, M. Sawangphruk, Rechargeable Photoactive Zn-air batteries Using NiCo<sub>2</sub>S<sub>4</sub> as

an Efficient Bifunctional Photocatalyst towards OER/ORR at the Cathode, Batter. Supercaps. (n.d.).

- [117] Y. Miao, X. Zhao, X. Wang, C. Ma, L. Cheng, G. Chen, H. Yue, L. Wang, D. Zhang, Flower-like NiCo<sub>2</sub>S<sub>4</sub> nanosheets with high electrochemical performance for sodium-ion batteries, *Nano Res.* 13 (2020) 3041–3047.
- [118] W. Zhang, J. Chen, Y. Liu, S. Liu, X. Li, K. Yang, L. Li, Decoration of hollow nitrogen-doped carbon nanofibers with tapered rod-shaped NiCo<sub>2</sub>S<sub>4</sub> as a 3D structural high-rate and long-lifespan self-supported anode material for potassium-ion batteries, *J. Alloys Compd.* 823 (2020) 153631.
- [119] S. Hussain, M. Hassan, M.S. Javed, A. Shaheen, S.S.A. Shah, M.T. Nazir, T. Najam, A.J. Khan, X. Zhang, G. Liu, Distinctive flower-like CoNi<sub>2</sub>S<sub>4</sub> nanoneedle arrays (CNS–NAs) for superior supercapacitor electrode performances, *Ceram. Int.* 46 (2020) 25942–25948.
- [120] A.K. Yedluri, D.K. Kulurumotlakatla, S. Sangaraju, M.O. Ihab, H.-J. Kim, Facile synthesis of novel and highly efficient CoNi<sub>2</sub>S<sub>4</sub>-Ni(OH)<sub>2</sub> nanosheet arrays as pseudocapacitive-type electrode material for high-performance electrochemical supercapacitors, *J. Energy Storage.* 31 (2020) 101623.
- [121] X. Liu, Q. Li, X. Zhang, Y. Jiang, Hybrid structured CoNi<sub>2</sub>S<sub>4</sub>/Ni<sub>3</sub>S<sub>2</sub> nanowires with multifunctional performance for hybrid capacitor electrodes and overall water splitting, *RSC Adv.* 10 (2020) 33428–33435.
- [122] K. Zhang, Y. Wei, J. Huang, Y. Xiao, W. Yang, T. Hu, K. Yuan, Y. Chen, A generalized one-step in situ formation of metal sulfide/reduced graphene oxide nanosheets toward high-performance supercapacitors, *Sci. China Mater.* 63 (2020) 1898–1909.
- [123] R.K. Bhardwaj, S. Jayanthi, P.S. Adarakatti, A.K. Sood, A.J. Bhattacharyya, Probing the extent of polysulfide confinement using CoNi<sub>2</sub>S<sub>4</sub> additive inside sulfur cathode of Na/Li-sulfur rechargeable battery, *ACS Appl. Mater. Interfaces.* (2020).

- [124] Z. Jia, Z. Cui, Y. Tan, Z. Liu, X. Guo, Bimetal-organic frameworks derived ternary metal sulphide nanoparticles embedded in porous carbon spheres/carbon nanotubes as high-performance lithium storage materials, *Chem. Eng. J.* 370 (2019) 89–97.
- [125] S. Sun, Y. Nie, M. Sun, T. Liang, M. Sun, H. Yang, Facile synthesis of CoNi<sub>2</sub>S<sub>4</sub> one-dimensional nanorods as anode for high performance lithium ion batteries, *Mater. Lett.* 176 (2016) 87–90.
- [126] W. Yang, L. Chen, J. Yang, X. Zhang, C. Fang, Z. Chen, L. Huang, J. Liu, Y. Zhou, Z. Zou, One-step growth of 3D CoNi<sub>2</sub>S<sub>4</sub> nanorods and cross-linked NiCo<sub>2</sub>S<sub>4</sub> nanosheet arrays on carbon paper as anodes for high-performance lithium ion batteries, *Chem. Commun.* 52 (2016) 5258–5261.
- [127] W. Dai, K. Ren, Y. Zhu, Y. Pan, J. Yu, T. Lu, Flower-like CoNi<sub>2</sub>S<sub>4</sub>/Ni<sub>3</sub>S<sub>2</sub> nanosheet clusters on nickel foam as bifunctional electrocatalyst for overall water splitting, *J. Alloys Compd.* 844 (2020) 156252.
- [128] P. Wang, J. Qi, C. Li, W. Li, T. Wang, C. Liang, Hierarchical CoNi<sub>2</sub>S<sub>4</sub>@NiMn-layered double hydroxide heterostructure nanoarrays on superhydrophilic carbon cloth for enhanced overall water splitting, *Electrochim. Acta.* (2020) 136247.
- [129] K.S. Ranjith, C.H. Kwak, S.M. Ghoreishian, J.S. Im, Y.S. Huh, Y.-K. Han, Ultrathin rGO-wrapped free-standing bimetallic CoNi<sub>2</sub>S<sub>4</sub>-carbon nanofibers: an efficient and robust bifunctional electrocatalyst for water splitting, *Nanotechnology.* 31 (2020) 275402.
- [130] R. Huang, W. Chen, Y. Zhang, Z. Huang, H. Dai, Y. Zhou, Y. Wu, X. Lv, Well-designed cobalt-nickel sulfide microspheres with unique peapod-like structure for overall water splitting, *J. Colloid Interface Sci.* 556 (2019) 401–410.
- [131] B.J. Rani, K. Nivedha, G. Ravi, R. Yuvakkumar, Electrochemical Water Oxidation of NiCo<sub>2</sub>O<sub>4</sub> and CoNi<sub>2</sub>S<sub>4</sub> Nanospheres Supported on Ni Foam

Substrate, *ChemistrySelect*. 4 (2019) 10122–10132.

- [132] L. Li, J. Xu, M. Mao, X. Li, S. Zhao, Z. Liu, Y. Li, Effect of visible light irradiation on hydrogen production by CoNi<sub>2</sub>S<sub>4</sub>/CdWO<sub>4</sub> controllable flower spherical photocatalyst, *Appl. Surf. Sci.* 481 (2019) 692–701.
- [133] T. Xu, J. Zhao, L. Li, J. Mao, J. Xu, H. Zhao, Co/Ni-MOF-74-derived CoNi<sub>2</sub>S<sub>4</sub> nanoparticles embedded in porous carbon as a high performance anode material for sodium ion batteries, *New J. Chem.* 44 (2020) 13141–13147.
- [134] T. Xu, J. Zhao, J. Yang, J. Chen, Y. Wu, J. Xu, One-pot solvothermal synthesis of CoNi<sub>2</sub>S<sub>4</sub>/reduced graphene oxide (rGO) nanocomposites as anode for sodium-ion batteries, *Ionics (Kiel)*. 26 (2020) 213–221.
- [135] Z. Xu, H. Pan, Y. Lin, Z. Yang, J. Wang, Y. Gong, Constructing a hexagonal copper-coin-shaped NiCoSe<sub>2</sub>@NiO@CoNi<sub>2</sub>S<sub>4</sub>@CoS<sub>2</sub> hybrid nanoarray on nickel foam as a robust oxygen evolution reaction electrocatalyst, *J. Mater. Chem. A*. 6 (2018) 18641–18648.
- [136] F. Hartmann, M. Etter, G. Cibir, L. Liers, H. Terraschke, W. Bensch, Superior Sodium Storage Properties in the Anode Material NiCr<sub>2</sub>S<sub>4</sub> for Sodium-Ion Batteries: An X-ray Diffraction, Pair Distribution Function, and X-ray Absorption Study Reveals a Conversion Mechanism via Nickel Extrusion, *Adv. Mater.* 33 (2021). <https://doi.org/10.1002/adma.202101576>.
- [137] S.K. Hussain, B.N. V Krishna, J.S. Yu, Transition metal dichalcogenide nanostructured electrodes without calcination for aqueous asymmetric supercapacitors, *Int. J. ENERGY Res.* (n.d.). <https://doi.org/10.1002/er.7814>.
- [138] D.Z. Kong, Y. Wang, S.Z. Huang, Y. Von Lim, M.L. Wang, T.T. Xu, J.H. Zang, X.N. Li, H.Y. Yang, Defect-Engineered 3D hierarchical NiMo<sub>3</sub>S<sub>4</sub> nanoflowers as bifunctional electrocatalyst for overall water splitting, *J. Colloid Interface Sci.* 607 (2022) 1876–1887. <https://doi.org/10.1016/j.jcis.2021.10.020>.

- [139] M. Wu, S.F. Wang, J.H. Wang, Engineering NiMo<sub>3</sub>S<sub>4</sub> vertical bar Ni<sub>3</sub>S<sub>2</sub> interface for excellent hydrogen evolution reaction in alkaline medium, *Electrochim. Acta.* 258 (2017) 669–676. <https://doi.org/10.1016/j.electacta.2017.11.112>.
- [140] D.Z. Kong, Y. Wang, Y. Von Lim, S.Z. Huang, J. Zhang, B. Liu, T.P. Chen, H.Y. Yang, 3D hierarchical defect-rich NiMo<sub>3</sub>S<sub>4</sub> nanosheet arrays grown on carbon textiles for high-performance sodium-ion batteries and hydrogen evolution reaction, *NANO ENERGY.* 49 (2018) 460–470. <https://doi.org/10.1016/j.nanoen.2018.04.051>.
- [141] C.-H. Lai, M.-Y. Lu, L.-J. Chen, Metal sulfide nanostructures: synthesis, properties and applications in energy conversion and storage, *J. Mater. Chem.* 22 (2012) 19–30.
- [142] M.J. Patterson, Structure and reactivity studies of size-selected transition metal sulfide nanoclusters in the gas phase and supported on gold (111), State University of New York at Stony Brook, 2009.
- [143] S. Chandrasekaran, L. Yao, L. Deng, C. Bowen, Y. Zhang, S. Chen, Z. Lin, F. Peng, P. Zhang, Recent advances in metal sulfides: from controlled fabrication to electrocatalytic, photocatalytic and photoelectrochemical water splitting and beyond, *Chem. Soc. Rev.* 48 (2019) 4178–4280.
- [144] F. Bosi, C. Biagioni, M. Pasero, Nomenclature and classification of the spinel supergroup, *Eur. J. Mineral.* 31 (2019) 183–192.
- [145] C. Biagioni, M. Pasero, The systematics of the spinel-type minerals: An overview, *Am. Mineral.* 99 (2014) 1254–1264.
- [146] R. Hoogenboom, T.F.A. Wilms, T. Erdmenger, U.S. Schubert, Microwave-assisted chemistry: a closer look at heating efficiency, *Aust. J. Chem.* 62 (2009) 236–243.
- [147] J.M. Kremsner, A. Stadler, A chemist's guide to microwave synthesis: Basics,

equipment & application examples, Graz Ant. Paar GmbH. (2013).

- [148] H. Wang, J. Tang, Y. Li, H. Chu, Y. Ge, R. Baines, P. Dong, P.M. Ajayan, J. Shen, M. Ye, Template-free solvothermal preparation of ternary FeNi<sub>2</sub>S<sub>4</sub> hollow balloons as RuO<sub>2</sub>-like efficient electrocatalysts for the oxygen evolution reaction with superior stability, *J. Mater. Chem. A*. 6 (2018) 19417–19424.
- [149] L. An, Z. Zhang, J. Feng, F. Lv, Y. Li, R. Wang, M. Lu, R.B. Gupta, P. Xi, S. Zhang, Heterostructure-promoted oxygen electrocatalysis enables rechargeable zinc–air battery with neutral aqueous electrolyte, *J. Am. Chem. Soc.* 140 (2018) 17624–17631.
- [150] J. Jiang, Y.-J. Zhang, X.-J. Zhu, S. Lu, L.-L. Long, J.-J. Chen, Nanostructured metallic FeNi<sub>2</sub>S<sub>4</sub> with reconstruction to generate FeNi-based oxide as a highly-efficient oxygen evolution electrocatalyst, *Nano Energy*. 81 (n.d.) 105619.
- [151] D. Ma, M. Lv, Y. Shen, Y. Zhu, F. Wang, X. Zhang, Fabrication of Porous Mesh-Like FeCo<sub>2</sub>S<sub>4</sub> Nanosheet Arrays on Ni Foam for High Performance all Solid-State Supercapacitors and Water Splitting, *ChemistrySelect*. 4 (2019) 1879–1889.
- [152] J. Hu, Y. Ou, Y. Li, D. Gao, Y. Zhang, P. Xiao, FeCo<sub>2</sub>S<sub>4</sub> nanosheet arrays supported on Ni foam: an efficient and durable bifunctional electrocatalyst for overall water-splitting, *ACS Sustain. Chem. Eng.* 6 (2018) 11724–11733.
- [153] Y. Gong, H. Pan, Z. Xu, Z. Yang, Y. Lin, J. Wang, Crossed FeCo<sub>2</sub>S<sub>4</sub> nanosheet arrays grown on 3D nickel foam as high-efficient electrocatalyst for overall water splitting, *Int. J. Hydrogen Energy*. 43 (2018) 17259–17264.
- [154] X. Hu, R. Wang, P. Sun, Z. Xiang, X. Wang, Tip-Welded Ternary FeCo<sub>2</sub>S<sub>4</sub> Nanotube Arrays on Carbon Cloth as Binder-Free Electrocatalysts for Highly Efficient Oxygen Evolution, *ACS Sustain. Chem. Eng.* 7 (2019) 19426–19433.

- [155] X. Du, C. Huang, X. Zhang, Water splitting catalysis beginning with FeCo<sub>2</sub>S<sub>4</sub>@ Ni(OH)<sub>2</sub>: Investigation of the true catalyst with favorable stability, *Int. J. Hydrogen Energy*. 44 (2019) 31902–31915.
- [156] L. Li, L. Yang, S. Zhang, Y. Sun, F. Li, T. Qin, X. Liu, Y. Zhou, S. Alwarappan, A NiCo<sub>2</sub>S<sub>4</sub>@ N/S–CeO<sub>2</sub> composite as an electrocatalytic signal amplification label for aptasensing, *J. Mater. Chem. C*. 8 (2020) 14723–14731.
- [157] X. Wu, S. Li, J. Liu, M. Yu, Mesoporous Hollow Nested Nanospheres of Ni, Cu, Co-Based Mixed Sulfides for Electrocatalytic Oxygen Reduction and Evolution, *ACS Appl. Nano Mater.* 2 (2019) 4921–4932.
- [158] M. Mao, J. Xu, X. Yu, Y. Liu, A Z-type heterojunction of bimetal sulfide CuNi<sub>2</sub>S<sub>4</sub> and CoWO<sub>4</sub> for catalytic hydrogen evolution, *Dalt. Trans.* 49 (2020) 6457–6470.
- [159] P.S. Adarakatti, M. Mahanthappa, J.P. Hughes, S.J. Rowley-Neale, G.C. Smith, S. Ashoka, C.E. Banks, MoS<sub>2</sub>-graphene-CuNi<sub>2</sub>S<sub>4</sub> nanocomposite an efficient electrocatalyst for the hydrogen evolution reaction, *Int. J. Hydrogen Energy*. 44 (2019) 16069–16078.
- [160] A.T.A. Ahmed, A.S. Ansari, S.M. Pawar, B. Shong, H. Kim, H. Im, Anti-corrosive FeO decorated CuCo<sub>2</sub>S<sub>4</sub> as an efficient and durable electrocatalyst for hydrogen evolution reaction, *Appl. Surf. Sci.* 539 (2021) 148229.
- [161] Z. Hao, P. Wei, Y. Yang, J. Sun, Y. Song, D. Guo, L. Liu, Self-assembled CuCo<sub>2</sub>S<sub>4</sub> nanosheets with rich surface Co<sup>3+</sup> as efficient electrocatalysts for oxygen evolution reaction, *Appl. Surf. Sci.* 536 (2021) 147826.
- [162] L. Shao, Z.-X. Liang, H. Chen, Z.-X. Song, X.-H. Deng, G. Huo, X.-M. Kang, L. Wang, X.-Z. Fu, J.-L. Luo, CuCo<sub>2</sub>S<sub>4</sub> hollow nanoneedle arrays supported on Ni foam as efficient trifunctional electrocatalysts for overall water splitting and Al–Air batteries, *J. Alloys Compd.* (2020) 155392.

- [163] X. Xu, Z. Huang, C. Zhao, X. Ding, X. Liu, D. Wang, Z. Hui, R. Jia, Y. Liu, Interface engineering of copper-cobalt based heterostructure as bifunctional electrocatalysts for overall water splitting, *Ceram. Int.* (2020).
- [164] X. Du, Y. Ding, H. Su, X. Zhang, Effect of cation substitution on the water splitting performance of spinel cobaltite  $MCo_2S_4$  ( $M= Ni, Cu$  and  $Co$ ), *Int. J. Hydrogen Energy.* (2020).
- [165] B. Guo, S. Bandaru, C. Dai, H. Chen, Y. Zhang, Q. Xu, S. Bao, M. Chen, M. Xu, Self-Supported  $FeCo_2S_4$  Nanotube Arrays as Binder-Free Cathodes for Lithium–Sulfur Batteries, *ACS Appl. Mater. Interfaces.* 10 (2018) 43707–43715.
- [166] H. Wu, L. Wang, J. Bi, Y. Li, X. Pang, Z. Li, Q. Meng, H. Liu, L. Wang, Local Concentration Effect-Derived Heterogeneous  $Li_2S_2/Li_2S$  Deposition on Dual-Phase MWCNT/Cellulose Nanofiber/ $NiCo_2S_4$  Self-Standing Paper for High Performance of Lithium Polysulfide Batteries, *ACS Appl. Mater. Interfaces.* 12 (2020) 15228–15238.
- [167] L. Zhang, Y. Huang, Y.-E. Miao, W. Fan, T. Liu, Hierarchical composites of  $NiCo_2S_4$  nanorods grown on carbon nanofibers as anodes for high-performance lithium ion batteries, *Compos. Commun.* 21 (2020) 100395.
- [168] H. Zhang, A. Hao, Z. Sun, X. Ning, J. Guo, Y. Lv, D. Jia, Boosting the performance of half/full lithium-ion batteries by designing smart architecture anode of  $SnS_2$  nanosheet coating on  $NiCo_2S_4$  hollow spheres, *J. Alloys Compd.* 847 (2020) 156505.
- [169] K. Giagloglou, J.L. Payne, C. Crouch, R.K.B. Gover, P.A. Connor, J.T.S. Irvine, Synthesis and electrochemical study of  $CoNi_2S_4$  as a novel cathode material in a primary Li thermal battery, *J. Electrochem. Soc.* 164 (2017) A2159.
- [170] T. Lu, Y. Zhang, C. Cheng, Y. Wang, Y. Zhu, One-step synthesis of recoverable  $CuCo_2S_4$  anode material for high-performance Li-ion batteries,

Front. Chem. Sci. Eng. (2019) 1–10.

- [171] Q. Li, Q. Jiao, H. Li, W. Zhou, X. Feng, B. Qiu, Q. Shi, Y. Zheng, Y. Zhao, C. Feng, In-situ preparation of multi-layered sandwich-like CuCo<sub>2</sub>S<sub>4</sub>/rGO architectures as anode material for high-performance lithium and sodium ion batteries, *J. Alloys Compd.* 845 (2020) 156183.
- [172] A.T.A. Ahmed, B. Hou, S.M. Pawar, H. Kim, H. Im, Graphene-integrated CuCo<sub>2</sub>S<sub>4</sub> microspheres as a sustainable anode material for high-performance Li-ion batteries, *Int. J. Energy Res.* (2020).
- [173] M.-H. Wang, S.-P. Guo, Highly uniform hollow CuCo<sub>2</sub>S<sub>4</sub>@ C dodecahedra derived from ZIF-67 for high performance lithium-ion batteries, *J. Alloys Compd.* (2020) 154978.
- [174] Q. Li, Q. Jiao, X. Feng, Y. Zhao, H. Li, C. Feng, D. Shi, H. Liu, H. Wang, X. Bai, One-Pot Synthesis of CuCo<sub>2</sub>S<sub>4</sub> Sub-Microspheres for High-Performance Lithium-/Sodium-Ion Batteries, *ChemElectroChem.* 6 (2019) 1558–1566.
- [175] L. Cai, H. Wan, Q. Zhang, J.P. Mwisizerwa, X. Xu, X. Yao, In Situ Coating of Li<sub>7</sub>P<sub>3</sub>S<sub>11</sub> Electrolyte on CuCo<sub>2</sub>S<sub>4</sub>/Graphene Nanocomposite as a High-Performance Cathode for All-Solid-State Lithium Batteries, *ACS Appl. Mater. Interfaces.* 12 (2020) 33810–33816.
- [176] N.-T. Suen, S.-F. Hung, Q. Quan, N. Zhang, Y.-J. Xu, H.M. Chen, Electrocatalysis for the oxygen evolution reaction: recent development and future perspectives, *Chem. Soc. Rev.* 46 (2017) 337–365.
- [177] J. O'm Bockris, A.K.N. Reddy, A.K. Vijh, Modern electrochemistry, *J. Electrochem. Soc.* 119 (1972) 136C.
- [178] R. Guidelli, R.G. Compton, J.M. Feliu, E. Gileadi, J. Lipkowski, W. Schmickler, S. Trasatti, Defining the transfer coefficient in electrochemistry: An assessment (IUPAC Technical Report), *Pure Appl. Chem.* 86 (2014) 245–258.

- [179] X. Liu, C. Wang, In situ wet etching of MoS<sub>2</sub>@ dWO<sub>3</sub> heterostructure as ultra-stable highly active electrocatalyst for hydrogen evolution reaction, *Catalysts*. 10 (2020) 977.
- [180] A.K. Samantara, S. Ratha, *Metal Oxides/Chalcogenides and Composites: Emerging Materials for Electrochemical Water Splitting*, Springer, 2019.
- [181] L. Lutterotti, S. Matthies, H.-R. Wenk, MAUD (material analysis using diffraction): a user friendly Java program for Rietveld texture analysis and more, in: *Proceeding Twelfth Int. Conf. Textures Mater.*, NRC Research Press Ottawa, Canada, 1999: p. 1599.
- [182] H. Okamoto, M.E. Schlesinger, E.M. Mueller, eds., *Co (Cobalt) Binary Alloy Phase Diagrams*, *Alloy Phase Diagrams*. 3 (2016) 0. <https://doi.org/10.31399/asm.hb.v03.a0006156>.
- [183] L. Lutterotti, S. Matthies, H.R. Wenk, MAUD: a friendly Java program for material analysis using diffraction, *IUCr Newsl. CPD*. 21 (1999).
- [184] L. Kumar, B. Antil, A. Kumar, M.R. Das, S. Deka, A Superior and Stable Electrocatalytic Oxygen Evolution Reaction by One-Dimensional FeCoP Colloidal Nanostructures, *ACS Appl. Mater. Interfaces*. (2022).
- [185] R. Karthikeyan, D. Thangaraju, N. Prakash, Y. Hayakawa, Single-step synthesis and catalytic activity of structure-controlled nickel sulfide nanoparticles, *CrystEngComm*. 17 (2015) 5431–5439.
- [186] G.D. Park, J.S. Cho, Y.C. Kang, Sodium-ion storage properties of nickel sulfide hollow nanospheres/reduced graphene oxide composite powders prepared by a spray drying process and the nanoscale Kirkendall effect, *Nanoscale*. 7 (2015) 16781–16788.
- [187] H.N. Nong, L.J. Falling, A. Bergmann, M. Klingenhof, H.P. Tran, C. Spöri, R. Mom, J. Timoshenko, G. Zichittella, A. Knop-Gericke, Key role of chemistry versus bias in electrocatalytic oxygen evolution, *Nature*. 587 (2020)

408–413.

- [188] B. Liu, H. Nakatani, M. Terano, New aspects of the induction period of ethene polymerization using Phillips CrOx/SiO<sub>2</sub> catalyst probed by XPS, TPD and EPMA, *J. Mol. Catal. A Chem.* 184 (2002) 387–398. [https://doi.org/https://doi.org/10.1016/S1381-1169\(02\)00019-5](https://doi.org/https://doi.org/10.1016/S1381-1169(02)00019-5).
- [189] B. Yan, D. Krishnamurthy, C.H. Hendon, S. Deshpande, Y. Surendranath, V. Viswanathan, Surface restructuring of nickel sulfide generates optimally coordinated active sites for oxygen reduction catalysis, *Joule*. 1 (2017) 600–612.
- [190] J. Yan, G. Lui, R. Tjandra, X. Wang, L. Rasenthiram, A. Yu,  $\alpha$ -NiS grown on reduced graphene oxide and single-wall carbon nanotubes as electrode materials for high-power supercapacitors, *RSC Adv.* 5 (2015) 27940–27945.
- [191] M. Tahir, L. Pan, F. Idrees, X. Zhang, L. Wang, J.-J. Zou, Z.L. Wang, Electrocatalytic oxygen evolution reaction for energy conversion and storage: a comprehensive review, *Nano Energy*. 37 (2017) 136–157.
- [192] M. Gao, W. Sheng, Z. Zhuang, Q. Fang, S. Gu, J. Jiang, Y. Yan, Efficient water oxidation using nanostructured  $\alpha$ -nickel-hydroxide as an electrocatalyst, *J. Am. Chem. Soc.* 136 (2014) 7077–7084.
- [193] D. Zheng, L. Yu, W. Liu, X. Dai, X. Niu, W. Fu, W. Shi, F. Wu, X. Cao, Structural advantages and enhancement strategies of heterostructure water-splitting electrocatalysts, *Cell Reports Phys. Sci.* 2 (2021) 100443.
- [194] W. Zhou, X.-J. Wu, X. Cao, X. Huang, C. Tan, J. Tian, H. Liu, J. Wang, H. Zhang, Ni<sub>3</sub>S<sub>2</sub> nanorods/Ni foam composite electrode with low overpotential for electrocatalytic oxygen evolution, *Energy Environ. Sci.* 6 (2013) 2921–2924. <https://doi.org/10.1039/C3EE41572D>.
- [195] J.-B. Jorcin, M.E. Orazem, N. Pébère, B. Tribollet, CPE analysis by local electrochemical impedance spectroscopy, *Electrochim. Acta.* 51 (2006)

1473–1479.

- [196] T. Liu, P. Diao, Nickel foam supported Cr-doped NiCo<sub>2</sub>O<sub>4</sub>/FeOOH nanoneedle arrays as a high-performance bifunctional electrocatalyst for overall water splitting, *Nano Res.* 13 (2020) 3299–3309.
- [197] J. Balach, J. Linnemann, T. Jaumann, L. Giebeler, Metal-based nanostructured materials for advanced lithium–sulfur batteries, *J. Mater. Chem. A.* 6 (2018) 23127–23168.
- [198] X. Rui, H. Tan, Q. Yan, Nanostructured metal sulfides for energy storage, *Nanoscale.* 6 (2014) 9889–9924.
- [199] Z. Kou, X. Li, L. Zhang, W. Zang, X. Gao, J. Wang, Dynamic surface chemistry of catalysts in oxygen evolution reaction, *Small Sci.* 1 (2021) 2100011.
- [200] J. Jiang, F. Sun, S. Zhou, W. Hu, H. Zhang, J. Dong, Z. Jiang, J. Zhao, J. Li, W. Yan, Atomic-level insight into super-efficient electrocatalytic oxygen evolution on iron and vanadium co-doped nickel (oxy) hydroxide, *Nat. Commun.* 9 (2018) 1–12.
- [201] T. Yang, J. Zhou, X. Ma, K. Ding, K.C. Tan, G. Wang, H. Huang, M. Yang, Unravelling Distance-Dependent Inter-Site Interactions and Magnetic Transition Effects of Heteronuclear Single Atom Catalysts on Electrochemical Oxygen Reduction, *ArXiv Prepr. ArXiv2201.05801.* (2022).
- [202] Z. Jin, P. Li, Y. Meng, Z. Fang, D. Xiao, G. Yu, Understanding the inter-site distance effect in single-atom catalysts for oxygen electroreduction, *Nat. Catal.* 4 (2021) 615–622.
- [203] H.A. El-Sayed, A. Weiß, L.F. Olbrich, G.P. Putro, H.A. Gasteiger, OER catalyst stability investigation using RDE technique: a stability measure or an artifact?, *J. Electrochem. Soc.* 166 (2019) F458.
- [204] A.R. Zeradjanin, J. Masa, I. Spanos, R. Schlögl, Activity and Stability of

Oxides During Oxygen Evolution Reaction---From Mechanistic Controversies Toward Relevant Electrocatalytic Descriptors, *Front. Energy Res.* 8 (2021) 613092.

- [205] Q. Li, D. Wang, C. Han, X. Ma, Q. Lu, Z. Xing, X. Yang, Construction of amorphous interface in an interwoven NiS/NiS<sub>2</sub> structure for enhanced overall water splitting, *J. Mater. Chem. A.* 6 (2018) 8233–8237.
- [206] S. Fan, H. Liu, S. Bi, C. Gao, X. Meng, Y. Wang, Insight on the conversion reaction mechanism of NiCo<sub>2</sub>S<sub>4</sub>@ CNTs as anode materials for lithium ion batteries and sodium ion batteries, *Electrochim. Acta.* 388 (2021) 138618.
- [207] P. Guo, H. Song, Y. Liu, C. Wang, FeNi<sub>2</sub>S<sub>4</sub> QDs@ C composites as a high capacity and long life anode material for lithium ion battery and ex situ investigation of electrochemical mechanism, *Electrochim. Acta.* 258 (2017) 1173–1181.
- [208] J. Gao, M.A. Lowe, Y. Kiya, H.D. Abruna, Effects of liquid electrolytes on the charge–discharge performance of rechargeable lithium/sulfur batteries: electrochemical and in-situ X-ray absorption spectroscopic studies, *J. Phys. Chem. C.* 115 (2011) 25132–25137.
- [209] E. Yamauchi, T. Takeuchi, H. Sakaebe, Improvement of Cycling Capability of Li<sub>2</sub>S-FeS Composite Positive Electrode Materials by Surface Coating With Titanium Oxide, *Front. Energy Res.* 7 (2019) 38.
- [210] Z. Li, J.T. Zhang, Y.M. Chen, J. Li, X.W.D. Lou, Pie-like electrode design for high-energy density lithium–sulfur batteries, *Nat. Commun.* 6 (2015) 1–8.
- [211] J. Meng, Q. He, L. Xu, X. Zhang, F. Liu, X. Wang, Q. Li, X. Xu, G. Zhang, C. Niu, Identification of phase control of carbon-confined Nb<sub>2</sub>O<sub>5</sub> nanoparticles toward high-performance lithium storage, *Adv. Energy Mater.* 9 (2019) 1802695.
- [212] S. Fang, D. Jackson, M.L. Dreibelbis, T.F. Kuech, R.J. Hamers, Anode-

originated SEI migration contributes to formation of cathode-electrolyte interphase layer, *J. Power Sources*. 373 (2018) 184–192.

- [213] P. Fan, H. Liu, L. Liao, J. Fu, Z. Wang, G. Lv, L. Mei, H. Hao, J. Xing, J. Dong, Flexible and high capacity lithium-ion battery anode based on a carbon nanotube/electrodeposited nickel sulfide paper-like composite, *RSC Adv.* 7 (2017) 49739–49744.
- [214] S. Lu, Z. Wang, X. Zhang, Z. He, H. Tong, Y. Li, J. Zheng, In situ-formed hollow cobalt sulfide wrapped by reduced graphene oxide as an anode for high-performance lithium-ion batteries, *ACS Appl. Mater. Interfaces*. 12 (2020) 2671–2678.
- [215] H. Chang, Y.-R. Wu, X. Han, T.-F. Yi, Recent developments in advanced anode materials for lithium-ion batteries, *Energy Mater.* 1 (2021) 24.



## CURRICULUM VITAE

Surname, Name: Savaş Uygur, Cansu

### EDUCATION

Degree	Institution	Year of Graduation
MS	METU, Metallurgical and Materials Engineering	2017
BS	METU, Metallurgical and Materials Engineering	2014
High School	Çankaya Anittepe Anadolu High School, Ankara	2007

### FOREIGN LANGUAGES

Advanced English

### PUBLICATIONS

1. Uygur, C. S., & Aydınol, M. K. (2022). *Chromium-Nickel Sulfides Synthesized with Microwave-Assisted Method as Promising OER Electrocatalysts*, submitted.
2. Uygur, C. S., & Aydınol, M. K. (2021). *Effect of calcium or yttrium doping on cation ordering and electrochemical performance of Li (Ni<sub>0.80-x</sub>Co<sub>0.15</sub>Al<sub>0.05</sub>M<sub>x</sub>) O<sub>2</sub> (M= Ca, Y) as a Li-ion battery cathode*. *Materials Science and Engineering: B*, 264, 114925.
3. Pişkin, B., Uygur, C. S., & Aydınol, M. K. (2020). *Morphology effect on electrochemical properties of doped (W and Mo) 622NMC, 111NMC, and 226NMC cathode materials*. *International Journal of Hydrogen Energy*, 45(14), 7874-7880.
4. Uygur, C. S., Pişkin, B., & Aydınol, M. K. (2019). *Synthesis of Li<sub>x</sub> (Ni<sub>0.80</sub>Co<sub>0.15</sub>Al<sub>0.05</sub>) O<sub>2</sub> cathodes with deficient and excess lithium using an ultrasonic sound-assisted co-precipitation method for Li-ion batteries*. *Bulletin of Materials Science*, 42(205).
5. Pişkin, B., Savaş Uygur, C., & Aydınol, M. K. (2018). *Mo doping of layered Li (Ni<sub>x</sub>Mn<sub>y</sub>Co<sub>1-x-y-z</sub>M<sub>z</sub>) O<sub>2</sub> cathode materials for lithium-ion batteries*. *International Journal of Energy Research*, 42(12), 3888-3898.
6. Kunduraci, M., Uygur, C. S., & Aydınol, M. K. (2018). *Activation of Manganese Ions in Lithium-ion Battery Anode Materials via Nickel and Cobalt Doping*. *Journal of Electronic Materials*, 47(11), 6420-6427.